2012

Mesoporous silica nanoparticles for applications in drug delivery and catalysis

Xiaoxing Sun
Iowa State University

Mesoporous silica nanoparticles for applications in drug delivery and catalysis

by

Xiaoxing Sun

A dissertation submitted to the graduate faculty
in partial fulfillment of the requirements for the degree of
DOCTOR OF PHILOSOPHY

Major: Chemistry

Program of Study Committee
Brian G. Trewyn, Co-major Professor
Ning Fang, Co-major Professor
Marek Pruski
Emily Smith
Huaiqing Wu

Iowa State University
Ames, Iowa
2012

TABLE OF CONTENTS

ACKNOWLEDGEMENTS

I would like to convey my sincere thanks and deep appreciation to those who have supported and inspired me during these years.

First and foremost, I am deeply indebted to my major professor, Dr. Victor Shang-Yi Lin, whose enthusiasm, encouragement, creativity, patience and dedication to science exemplified to me what a scientist should be. It is my supreme honor to have been a graduate student in his research group. Although he is no longer with us, his words and deeds will continue to guide me in my future life.

My sincere gratitude also extends to my advisor Dr. Brian G. Trewyn, for his guidance for my research and his generous support with my degree completion.

My special thanks to my co-major professor Dr. Ning Fang, as well as my past and present Program of Study Committee Members, Dr. Marek Pruski, Dr. Emily Smith, Dr. Huaiqing Wu, Dr. Zhiqun Lin, and Dr. Nicola L. Pohl for their time and insightful advices.

To my past and present group members, thank their patience and kindness with my research.

To my dear parents and my family whose encouragement has provided me enormous support.

To all my friends, thank their care and friendship.

My best wishes to everyone whose entry into my life has supported and motivated me to pursue my dream.

ABSTRACT

Mesoporous silica materials, discovered in 1992 by the Mobile Oil Corporation, have received considerable attention due to their superior textual properties such as high surface area, large pore volume, tunable pore diameter, and narrow pore size distribution. A general overview of recent developments of organofunctionalized hybrid mesoporous silica nanoparticles (MSNs) materials is presented, focusing on the use of MSNs as biocompatible, stimuli-responsive drug delivery devices and a description of the sophisticated systems with novel capping agents and controlled release mechanisms.

The potential of employing MSNs for drug delivery was further studied on the biological behaviors of these nanoparticles in blood vessels. The research demonstrated the size and surface effects on the interaction of MSNs with human red blood cell membranes, and proposed that appropriate surface modification of nanoparticles can improve their biocompatibility and diminish their dangerous side effects on red blood cells.

MSN materials have also been extensively applied in the field of catalysis. We have tethered a Pt(II) bipyridine catalyst onto MSNs in order to enhance its thermal stability and product selectivity. A detailed investigation on the catalytic activity showed that the catalytic performance was similar between the homogeneous and heterogeneous systems. However, the homogeneous system exhibited appreciable degradation after 16 hr at 100 °C. Instead, using MSNs as scaffolds, this catalyst system retained its activity after 72 hr at 150 °C, demonstrating an increased thermal stability.

We also explored the feasibility of introducing a biocatalyst to function synergically with MSN supported inorganic catalyst. Supported Au-nanoparticle catalyst employed for direct alcohol oxidative esterification usually suffers from a slow alcohol oxidation rate. We designed a co-catalyst system by combining a biocatalyst, alcohol dehydrogenase enzyme and an inorganic catalyst, mesoporous silica nanoparticles supported Au nanoparticle to accelerate reaction tandemly. We identified several factors that affect the catalytic performance of the co-catalyst system. We then examined the catalytic capability of this co-catalyst system on the one-pot transformation of allyl alcohol into allyl acrylate ester. We expect that this system could lead to the development of a variety of catalyst pairs for a great scope of reactions.

We further explored the possibility of the intracellular co-delivery of a biocatalyst and its substrate using MSNs. We designed a gold nanoparticle-capped MSNs platform and demonstrated its ability to release luciferin from the interior pores of MSNs upon gold nanoparticle uncapping in response to disulfide-reducing antioxidants, and co-deliver bioactive luciferase from the PEGylated exterior surface of MSNs into Hela cells. The effectiveness of intracellular catalytical reactions was evaluated by measuring luminescence emission signals. We envision that our co-delivery systems could play a significant role in intracellular controlled catalysis and tumor imaging.

The research presented in this dissertation would provide MSNs with a great potential for various biomedical and catalytic applications.

CHAPTER 1. DISSERTATION ORGANIZATION

The dissertation is organized in seven chapters. Chapter 1 describes the organization of the dissertation. Chapters 2-6 consist of journal articles either published or submitted for publication. Chapter 7 concludes this dissertation with summary of the results and discusses an outlook for future work.

Chapter 2 is an overview of the mesoporous silica nanoparticle family, from the synthesis and surface functionalization, to its applications in drug delivery and controlled release to both animal cells and plant cells.

Chapter 3 discusses the effects of size and surface functional groups of mesoporous silica nanoparticles on their interactions with human red blood cell membranes, which is a preliminary topic when employing them as intracellular drug delivery devices.

Chapters 4 to 6 describe catalytical applications of mesoporous silica nanoparticles.

Chapter 5 describes a co-catalyst system comprising an enzyme and a MSN supported gold-nanoparticle catalyst. The catalytic activity of the co-catalyst system was evaluated on the one-pot allyl alcohol oxidative esterification reaction, wherein an alcohol dehydrogenation reaction took place first on the biocatalyst and the products subsequently served as reactant for an esterification reaction catalyzed by Au catalyst.

We further explored the use of mesoporous silica nanoparticles to perform catalysis reactions intracellularly. Chapter 6 presents the design of an enzyme-substrate co-delivery system and demonstrates its *in vitro* application in triggering artificial intracellular reactions, converting biological energy into usable forms and controlling cell functions.

Finally, Chapter 7 is a brief conclusion of this dissertation, summarizing general accomplishments and potential future applications.

CHAPTER 2. MESOPOROUS SILICA NANOPARTICLES FOR DRUG DELIVERY AND CONTROLLED RELEASE

A manuscript submitted to the book ***Nanotechnology and Drug Delivery***

Xiaoxing Sun and Brian G. Trewyn

ABSTRACT

The advancement of mesoporous silica nanoparticles with unique structural features as non-invasive and biocompatible carriers to deliver drug molecules into animal and plant cells has been well established in pharmaceutical research over the recent decade. Herein, we review synthetic approaches of mesoporous silica nanoparticles and current progress on the functionalization of mesoporous silica nanoparticles with organic components and inorganic nanoparticles plus a short survey of characterization methods frequently discussed. Utilizing these flexible functionalization methods, versatile mesoporous silica nanoparticle assemblies are fabricated and used as drug delivery devices via numerous mechanisms. We highlight the development of the design and synthesis of nanovalve and capping systems on mesoporous silica nanoparticles, where drugs are encapsulated in the pores and released in a controlled fashion by physical, chemical or biological external or internal stimuli. Moreover, when functionalized with specific cell and antigen targeting moieties, mesoporous silica nanoparticles can selectively deliver drugs to diseased cells, and hence enhance chemotherapy effectiveness and reduce side effects. Recent reports have also demonstrated paradigms of successful in vivo drug delivery systems using mesoporous silica nanoparticles as a scaffold. We further discuss investigations on the biocompatibility of mesoporous silica nanoparticles and on the internalization efficiency of mesoporous silica nanoparticles by animal and plant cells.

1. Introduction

During the past several decades, a steadily growing number of drugs have been discovered. However, about 40 percent of newly designed drugs, especially those which are based on biomolecules such as peptides, oligonucleotides, proteins and DNA, often exhibit low bioavailability and are rejected by the pharmaceutical industry.[1] Therefore, there is an increasing demand for the development of drug delivery systems to minimize

drug degradation, manipulate drug pharmacological profile, diversify drug administration routes, decrease detrimental drug side effects and target specific sites. To achieve these goals, numerous materials have been extensively investigated, such as amphiphilic block copolymers,[2-4] liposomes,[5] dendrimers,[6,7] hydrogels,[8,9] as well as inorganic nanoparticles.[10,11]

Among numerous drug delivery systems tested, mesoporous silica nanoparticles (MSNs) stand out to be a promising candidate, which have the potential to perform all the above-mentioned functions simultaneously. Typically, MSNs used as drug delivery systems are featured by their ordered arrays of 2D hexagonal micro- or mesopore structure, uniform particle sizes (80-500 nm), large surface areas (>1000 m^2 g^{-1}), high pore volumes (0.5-2.5 cm^3 g^{-1}), tunable pore diameters (1.3-30 nm), controllable particle morphology and both exterior and interior surfaces that could be independently modified with a variety of functional groups. In contrast to conventional polymer-based drug delivery systems, which usually suffer from problems such as low drug loading capacity and poor drug release control, MSNs-based drug delivery systems successfully avoid these issues. The high surface areas and pore volumes allow for a large payload of drug molecules. The pore environment and surface can be adjusted by functional groups favored by drug molecules in order to further enhance drug loading and releasing ability. The highly stable pore channels prevent encapsulated drug molecules from degradation in harsh environments during drug administration. The tunable particle morphology of MSN materials renders their superb biocompatibility at concentrations adequate for pharmacological applications.

Furthermore, the most remarkable advantage of MSN materials as drug delivery systems is their “zero premature controlled release” property. Namely, drugs are carried with precise control of location and time without leaching prior to reaching the targeted cells or tissues. This technique is realized by encapsulating drug molecules inside the pores of MSN materials followed by blocking the pore entrances with stimuli responsive agents, or so called “caps”. Hence, delivery of drug molecules takes place only when these caps leave the MSN assembly when triggered by external or internal stimuli that are manipulated manually at a desired location and time. In addition, it is also possible to deliver guest molecules repeatedly in small portions by reversibly switching the MSNs-based drug delivery system between “on” and “off” status.

In this chapter, we review recent endeavors on the development of MSNs-based controlled release drug delivery systems, as well as investigations on their *in vitro* and *in vivo* applications.

2. Synthesis of Mesoporous Silica Nanoparticles

The family of mesoporous silica materials was independently discovered by Kresge et al.[12] at the Mobil Oil Company and the Kuroda group[13] at Waseda University in the early 1990s. Since then, research in this field has tremendously expanded. Mesoporous silica materials with different mesophases have been synthesized by varying experimental conditions such as pH, temperature, templates and molar ratios.[14,15] The earliest and most well known representative is MCM-41, exhibiting a 2D hexagonal mesopore arrangement (Fig. 1). Another example is SBA-15, sharing a 2D hexagonal structure, but it bears wider, tunable pore size range and greater hydrothermal stability than MCM-41. Both types of MSN materials have found applications as drug delivery devices.[10,16-19]

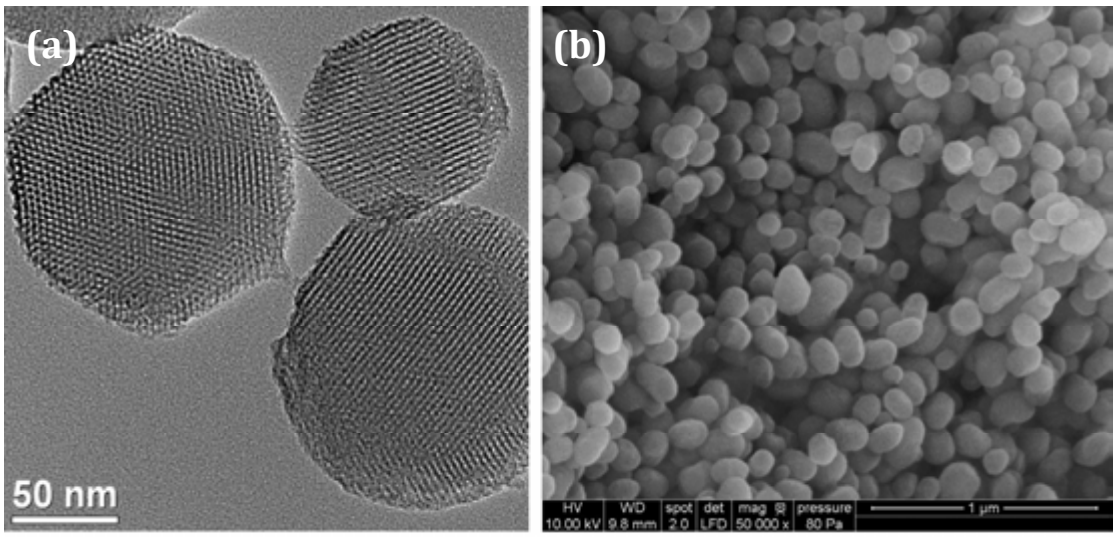

Figure 1. (a) Transmission electron micrograph and (b) Scanning electron micrograph of MCM-41 material.

The key principle for synthesizing MSN materials is the condensation of silica precursors directed by self-assembled liquid-crystal arrays of surfactants. In-depth investigations have led to two proposed mechanisms involved in the formation of supramolecular aggregates of surfactants and subsequent generation of MSN materials.[20] In the liquid crystal templating mechanism (LCT), surfactants form liquid crystal

structures at concentrations above the critical micelle concentration (CMC) of the surfactant and serve as templates, without requiring the addition of silica precursors. While an alternative mechanism was proposed that the final mesopore ordering is a process of cooperative interaction between surfactants and silica precursors. For example, MSN materials could be prepared even at surfactant concentrations far below the CMC, in which case an ordered liquid crystal structure could develop under the second mechanism.[21]

In a typical surfactant-silica precursor interaction, tetramethyl- (TMOS) or tetraethyl-orthosilicate (TEOS) is normally added as silica precursors, and cationic alkyltrimethylammonium salts are used as templates under a basic reaction condition. Further exploration was conducted by the Stucky research group, where they employed a series of block-copolymer surfactants as structure directing agents to synthesize MSNs in acidic environments.[22-25] A variety of strategies have been proposed to attain tunable pore sizes from less than 2 nm up to 30 nm, including the adjustment of the hydrocarbon chain length of small surfactant templates,[26,27] the use of pore swelling agents such as mesitylene,[26] or hydrothermal treatments.[28] The control over the surfactant-silica interaction enables a versatile synthesis condition for MSN materials, and thus allows for the functionalization of other species into the silica framework.

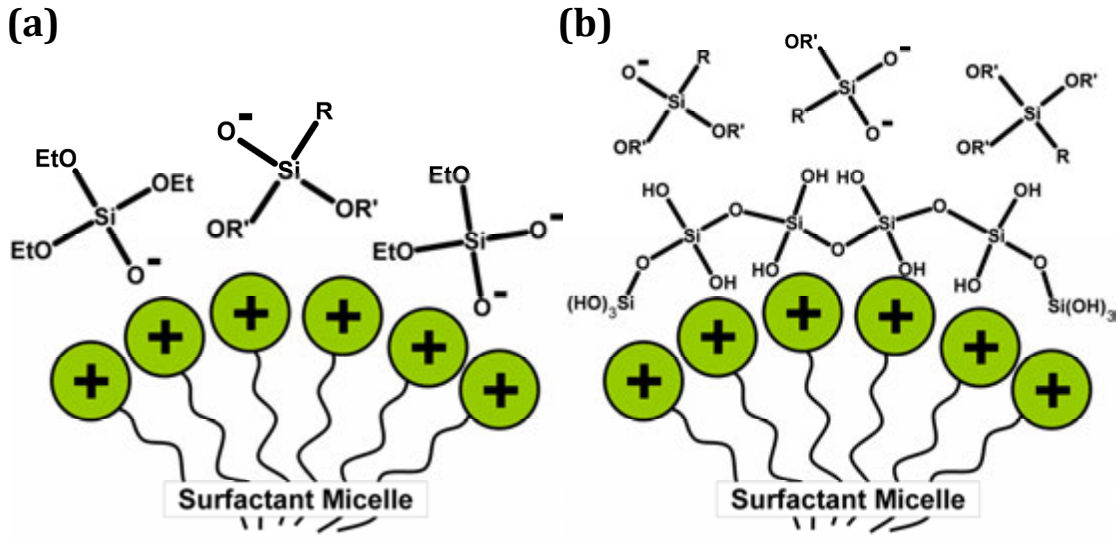

Figure 2. Surface functionalization of mesoporous silica nanoparticles by the (a) co-condensation method and (b) post-synthesis grafting method.

3. Surface Functionalization of Mesoporous Silica Nanoparticles

A notable advantage of using MSN materials as drug delivery systems is the relative ease to incorporate enormous variation of organic species with biocompatible MSN materials. The flexibility to modify MSN surfaces leads to the generation of a considerable number of MSN based hybrid materials that possess specific functions for drug delivery. Illustrations of these MSN derivatized materials and their functions will be discussed in later sections. The commonly used organic precursors are organotrialkoxysilanes [$(R'O)_3SiR$] or organotrichlorosilanes [Cl_3SiR]. Two popular pathways are available for surface functionalization (Fig. 2). One is to introduce organosilanes simultaneously with silica precursors during the synthesis of MSN materials ("co-condensation") (Fig. 2a). The other pathway is to prepare unfunctionalized MSN materials and subsequently modify their surfaces with organosilanes ("grafting") (Fig. 2b).

3.1 Surfaces Functionalization by Co-condensation Method

Co-condensation is a direct synthesis method where organosilanes are condensed along with the silica precursors in the presence of surfactant templates. As a result, the organic groups are homogeneously distributed within the mesoporous structure. Also, it is possible to control mesoporous silica nanoparticle morphology by the introduction of different organosilanes (Fig. 3). Lin and coworkers proposed that interactions between organosilanes and surfactant molecules, such as electrostatic interaction, hydrophobic interaction or hydrogen bonding could contribute to the variation in particle morphology.[29] They demonstrated that organosilanes with hydrophobic groups tend to intercalate their organic groups into the surfactant micelles and interact with the hydrophobic tails of surfactants, thus stabilizing the formation of long cylindrical micelles and giving rise to rod-shaped MSN materials. On the contrary, hydrophilic organosilanes would inhibit micelle growth and yield spherical particles with randomly oriented pore structures. As a result, by employing two organosilanes with opposite head group properties and varying their ratios, the surface functionality and particle morphology of MSN materials can be fine tuned with the co-condensation method.[30]

In order to preserve the pore structure and long-range pore ordering of MSNs, the amount of functional groups incorporated by the co-condensation method does not normally exceed 25 percent of surface coverage due to the difference in condensation

rates between organosilanes and silica precursors. The efficiency of loading depends on the nature of organic functional groups. A detailed study has been conducted by Lin and coworkers,[31] where they summarized that the amount of chemically accessible functional groups is proportional to the interfacial electrostatic matching between the functional groups and the surfactant head groups. Functional groups possessing a stronger ability to compete with the silicate anions in binding with surfactant molecules would be more likely to appear at MSN surfaces than those weakly binding functional groups which are usually embedded within the silica frameworks and are hence inaccessible. Based on their result, the degree of surface functionalization can be adjusted by choosing appropriate organic functional groups.

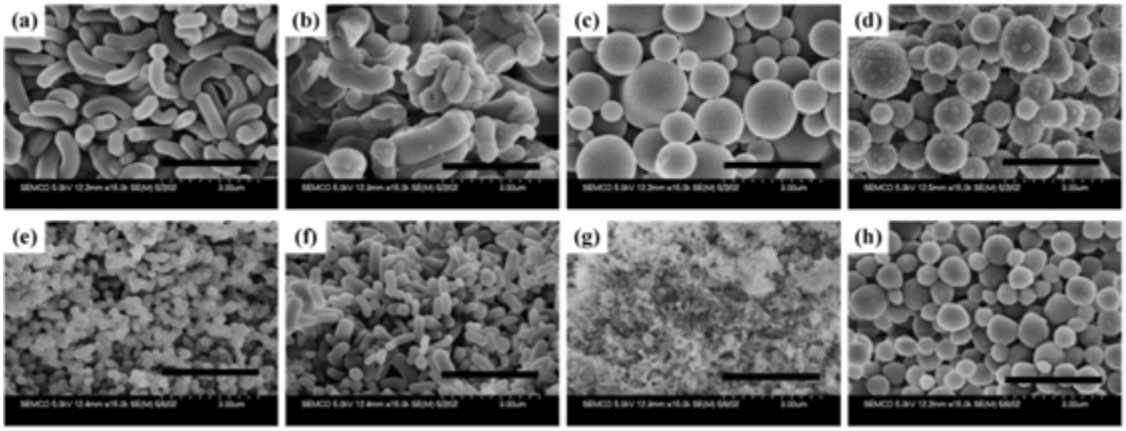

Figure 3. Field emission scanning electron microscopy (FE-SEM) images of (a) 3-aminopropyl-MSN, (b) N-(2-aminoethyl)-3-aminopropyl-MSN, (c) 3-[2-(2-aminoethyl-amino)ethylamino]propyl-MSN, (d) 3-ureidopropyl-MSN, (e) 3-isocyanatopropyl-MSN, (f) 3-cyanopropyl-MSN, (g) allyl-MSN, and (h) nonfunctionalized MSN. All images are presented using the same scale, with the scale bar = 3 μm. Reproduced with permission from ref. [29] Huh et al. 2003. Copyright 2003, American Chemical Society.

3.2 Surface Functionalization by Post-synthesis Grafting Method

In the grafting method, major functionalization reactions take place between organic precursors and free silanol groups at the exterior surface and at the opening of the pores of MSNs. Compared to the co-condensed material, organosilane grafted MSN materials have better retained pore structures and are more thermally stable. However, in most cases, the degree of functionalization by the grafting method is lower than that of co-condensation method, owing to the limited number of free surface silanol groups. As

opposed to the homogeneous functional groups coverage obtained by the co-condensation method, it has been reported that most functional groups are preferentially attached to the external surface or the pore openings, since the silanol groups are more easily accessible there than the interior pore surface which suffer from lower diffusion rates of organic precursors.[32] In certain situations such as when organic precursors are too big for the pores or they are unfavorable for the pore environment, their penetration to the inner sites of the pores is extremely impaired, leading to an unmodified internal surface. Taking advantage of this feature, it is feasible to selectively functionalize the external and internal surfaces of MSN materials with different functional groups.

3.3 Multi-functionalization

To satisfy the need for constructing more complex MSN based drug delivery systems, it is desirable to be able to incorporate more than one type of functional group with the MSN. Co-condensing two different organosilanes with silica precursors could be a simple solution, but as mentioned previously, different hydrolysis rates of silanes would undermine the ordering of MSNs material and restrict the loading quantity. Furthermore, locations of the functional groups cannot be regulated accurately. Therefore, a co-condensation and post-synthesis grafting combined approach for selectively incorporating functional groups onto external and internal surface of MSN materials was developed by Lin and coworkers.[33] A mercaptopropyl functionalized MSN material was first prepared by co-condensation method, yielding 90 percent of total thiol groups inside the pore channels, followed by 5,6-epoxyhexyltriethoxysilane (EHTES) grafted onto the outer surface of thiol-functionalized MSN materials with 43 percent surface coverage. The mercaptopropyl groups were converted to *o*-phthalic hemithioacetal (OPTA) groups and the 5,6-dihydroxyhexyl groups were used for a poly(lactic acid) coating. This assembly was reported as a detector for amino-containing neurotransmitters. In their study, both outer and inner surfaces of the MSN were modified without interacting with each other. Another strategy of sequential grafting was designed by the Ruiz-Hitzky group where external grafting with alkyl groups was carried out before removing surfactant templates so that the surfactant molecules would prevent the penetration of organic precursors into the pores.[34] Templates were extracted afterward by refluxing the particles in an ammonium chloride containing *n*-heptane/ethanol mixture. This template-free material then received a second grafting with aryl groups. Since most of the

external silanol groups were consumed in the first grafting, a majority of aryl groups reacted mainly with silanol groups inside the pore channels, generating MSN materials functionalized with organic groups topologically located as desired.

In a recent paper reported by Lo and coworkers,[35] a trifunctionalized MSN material was synthesized containing three distinct domains: the silica framework, the hexagonal pores and the outermost surfaces which were independently functionalized with contrast agents for imaging, drug payloads for cancer therapy and biomolecular ligands for cancer cell targeting, respectively. A near-infrared fluorescent contrast agent was co-condensed with TEOS for the optical tracking of MSN materials. The surfactant templates were then removed, followed by the grafting of nanochannels with a palladium-porphyrin based photosensitizer, which was exploited in photodynamic therapy. The third functionalization reaction occurred on the external surfaces with cRGDyK peptides that specifically bind to overexpressed integrins of cancer cells.

4. Biological Performance of Mesoporous Silica Nanoparticles

4.1 Intracellular Uptake of Mesoporous Silica Nanoparticles

To deliver encapsulated drug molecules into mammalian cells and perform therapeutic functions, MSN based drug delivery systems have to overcome the cell membrane boundary and be internalized by cells. Many research groups have demonstrated that MSN materials can be efficiently internalized by a variety of mammalian cells, including cancer cells (HeLa, CHO, lung, PANC-1, MCF-7, RIN-5F) and noncancer cells (liver, endothelial, skin fibroblast).[36-40] However, thorough understanding of cellular internalization mechanisms has not been fully unveiled. At the size domain of MSN materials, particles have been found to enter cells through endocytosis pathways in the majority of cases.[41] Various factors have been outlined to influence the kinetics and efficiency of intracellular endocytosis of MSN materials.

One of the factors dictating particle endocytosis is the surface functional group, as reported by Slowing et al[38]. The results showed that the surface functionalities not only regulate the uptake of MSN by HeLa cells, but also affect their ability to escape endosomal entrapment. Positively charged MSN materials exhibited better endocytosis efficiency than the negatively charged MSN, owing to a higher electrostatic affinity to the negatively charged cell membranes. On the other hand, the negatively charged particles possess superior endosomal escape ability, presumably due to a “proton sponge effect”. In

addition, folate groups on MSN materials could facilitate the HeLa cell uptake efficiency through a folate-receptor mediated endocytosis pathway. Therefore, as will be discussed, folic acid is widely used as a targeting ligand to regulate drug delivery accuracy.

The particle size and morphology also plays a role on the endocytosis of MSNs. The Lin research group observed a faster and higher intracellular uptake of smaller MSNs compared with larger ones[42]. This effect was further explored by Mou and coworkers[43], indicating an optimal particle size of 50 nm to reach the maximum uptake of MSNs by HeLa cells. Also, distinct endocytosis efficiencies were found with spherical- and tubular-shaped MSNs. Their investigations may allow researchers to control the rate of drug delivery more accurately.

4.2 Biocompatibility of Mesoporous Silica Nanoparticles

To evaluate the potential of MSNs as drug delivery devices, issues regarding the biocompatibility, biodistribution, retention and clearance of MSNs on cellular systems were examined by many research groups[10,38,44-50]. No significant cytotoxicity was observed of MSNs towards HeLa and CHO cells at dosage below 100 μg ml^{-1}, even after 6 d of incubation. A size- and concentration-dependent effect of MSNs on human dendritic cell viability was reported by Vallhov and coworker[45]. They found that smaller particles and lower concentrations affected human dendritic cells to a minor degree compared to the larger particles and higher concentrations, in terms of viability, uptake and immune regulatory markers, which is consistent with the *in vitro* results.

Likewise, a size- and morphology-dependent cytotoxicity of MSN materials on human red blood cells (RBCs) was confirmed by Haynes and Trewyn[51,52]. It was determined that in contrast to severe hemolytic activity of amorphous silica, MSNs showed high biocompatibility towards red blood cells at concentrations up to 100 μg ml^{-1}, which is possibly attributed to restricted RBC access to silanol groups on the surface of the MSN structures. Furthermore, MSNs with particle size of 600 nm caused an echinocytic shape transformation of RBCs and a subsequent hemolytic effect. These findings suggest that careful control over the particle size and surface functionalities can minimize toxicity of MSNs.

Recent investigations on the *in vivo* biodistribution and circulation determined that silica nanoparticles accumulated mainly in the liver, kidney and urinary bladder after intravenous injection, and then partially excreted through the renal route[48-50,53,54]. It is

worth noting that Hyeon and coworkers observed an accumulation of nanoparticles less than 200 nm in tumor masses 24 hr after administration, which is probably due to an enhanced permeability and retention effect at tumor sites[53]. Interestingly, the blood circulation time can be regulated by different surface functional groups. It was also reported that no short-term toxicity effect of MSNs was observed on mice at a dosage below 200 mg kg^{-1}, which is already significantly higher than the necessary dosage for drug delivery applications[46,53]. In a long-term study, accumulation of MSNs was observed in the liver for up to 3 months without apparent toxicity[54]. Therefore, although detailed information on the biocompatibility of MSNs still needs further investigations, there is little doubt that MSNs material will be a promising drug delivery device in clinical trials.

5. Mesoporous Silica Nanoparticles for Drug Controlled Release

As mentioned in the first section, the large drug loading capability, the flexible surface modification, the rigid porous structures and the excellent biocompatibility of MSNs are ideal for drug delivery applications. Initial research of employing mesoporous silica materials for drug adsorption/desorption was conducted by Vallet-Regí at the beginning of this century[16]. They successfully demonstrated that 80% of previously loaded ibuprofen was released in three days. In order to achieve an accurate control of drug releasing rate, a "stimuli-triggered release" concept was brought forward simultaneously by Tanaka and coworkers and Lin and coworkers two years later[10,55]. In Tanaka's approach, coumarin ligands were immobilized at the pore entrance and on the external surfaces by a grafting method. The uptake and release of guest molecules from pore voids were photo-regulated. The coumarin molecules underwent a dimerization reaction to completely seal the pore entrances when this sample was exposed to UV light ($\lambda > 310$ nm). Release of guest molecules was triggered by the cleavage of the coumarin dimers with UV light ($\lambda = 250$ nm) irradiation.

However, mesoporous silica samples prepared in Tanaka's study have no defined morphology or monodispersed sizes so that the biocompatibility of these materials is unsatisfactory for drug delivery applications. The first example of using biocompatible MSNs as carriers and inorganic nanoparticles as caps to effectively deliver drug molecules into animal cells with zero premature release was developed in the Lin research group[10]. They prepared spherical mesoporous silica nanoparticles with a uniform particle diameter of 200 nm and pore size of 2.3 nm, and then functionalized them with

2-(propyldisulfanyl)ethylamine groups. This MSNs sample was soaked in a concentrated solution of vancomycin or ATP to allow the diffusion of cargo molecules into the pores. Water-soluble cadmium sulfide (CdS) nanocrystals with mercaptoacetic acid groups were then added to react with the terminal amino groups on the surface of the MSNs. Thus, the CdS nanocrystals were covalently bonded to the MSNs and blocked the pore entrances. The resulting vancomycin- or ATP-loaded, CdS-capped MSNs were washed to remove physisorbed molecules. A quantitative analysis of the amounts of each compound was monitored by HPLC and the loading efficiency of vancomycin and ATP was calculated to be 25 and 47 μmol g^{-1}, respectively. The controlled release performance of this drug delivery system was evaluated. The material exhibited less than 1 percent drug release in buffer solution over a 12 hour period, suggesting a good pore blockage and minimal premature release. With the addition of disulfide reducing reagents such as dithiothreitol (DTT) or mercaptoethanol (ME) to cleave the CdS-MSN linkage, a rapid release was triggered and 85 percent of entrapped molecules were released within 24 hours. To further demonstrate its *in vitro* control release behavior, ATP-loaded, CdS-capped MSNs were cultured with astrocytes loaded with a calcium-chelating fluorescent dye. Perfusion application of ME led to a pronounced increase of intracellular calcium concentration, which was stimulated by ATP molecules carried by this drug delivery system.

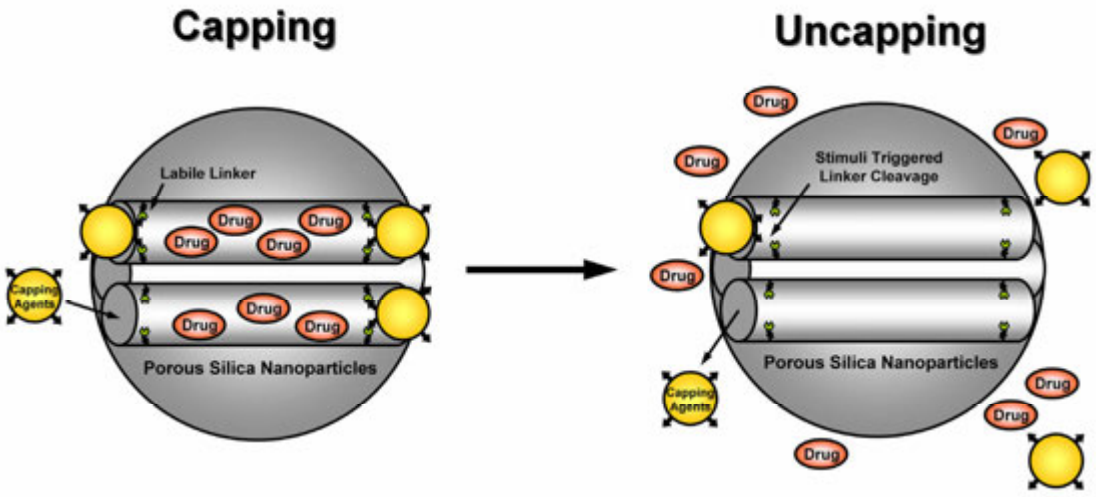

Figure 4. Design principle of mesoporous silica nanoparticles for controlled drug release. The capping agents block pore entrances and trap drug molecules by labile linkers which later respond to specific stimuli, triggering a drug release.

Over the past decade, many research groups have made great endeavors in the development of MSNs based drug delivery systems with stimuli-responsive triggered release property (Fig. 4). A number of regulating mechanisms have been proposed and confirmed their feasibility for intracellular drug delivery with precise control of location and timing. The triggers or stimuli can be internal, meaning that they are already present in the living organism, or external, which requires a simple and convenient pathway for application. Internal stimuli are often unique to the targeted pathology, which enables drug delivery systems to respond specifically to the desired location and release drugs in a self-regulated fashion. External controls are mostly noninvasive and easy to manipulate, so that they could assist to localize the drug release and optimize the degree of the drug delivery process. Examples of these triggers include pH, light, redox potential, temperature, enzymes, etc.

5.1 pH-triggered Release

A series of pH-responsive linkers have been exploited for controlled release applications by taking advantage of the acidic environment at tumor or inflammatory sites (pH ~ 6.8), endosomal or lysosomal compartments of cells (pH ~ 5-6) as well as the stomach (pH ~ 1.5-3.5). These pH-responsive linkers feature an inert respond to physiological pH and a robust release at low pH environment.

An early example of a pH-responsive release system was reported by Casacus et al., where they created a pH and anion controlled drug delivery system[56]. The MSN materials were prepared by the co-condensation of mercaptopropyltriethoxysilane with TEOS. A second grafting reaction was carried out with N-(3-triethoxysilylpropyl-2-aminoethyl)-eth ylenediamine to get a preferential anchoring of amino groups on the external surfaces. At high pH values, the amines were deprotonated and were tightly packed through hydrogen bonding interactions so that the delivery system was at its “open gate” state. However, when the amines were protonated at low pH conditions, they repelled each other and covered the pore openings due to the coulombic repulsion effect between positively charged amine groups and the delivery system was monitored to its “close gate” state. In addition, a significant synergic effect was observed in the presence of anions, which could intercalate into the open-chain polyamines and seal the pore openings. This effect is clearly associated with the anion size and the strength of the polyamine-anion

electrostatic interaction. Employing this pH-responsive drug delivery system, they have successfully demonstrated pH-controlled release of squaraine and vitamin B2.[57]

A pH-responsive drug delivery system for protein drugs was designed by Kawi and coworkers.[58] In order to encapsulate bulky proteins without denaturation, MSN materials with pore diameters above 10.5 nm and pore volumes around 1 cm^3 g^{-1} were synthesized in this study. These MSN materials were further modified with amine groups by co-condensation and were loaded with a model protein, bovine serum albumin (BSA). The positively charged BSA loaded MSNs were then mixed with a solution of polyacrylic acid (PAA) at pH 5.35. The electrostatic assembly of PAA blocked the pore entrances and trapped the BSA proteins, the final loading amount of BSA was calculated to be 16.3 percent. In pH 1.2 acidic medium, no release of BSA from the PAA-encapsulated sample was measured within 5 hours and released only 10 percent after 36 hours. However, in a phosphate buffer solution at pH 7.4, carboxyl groups on the PAA chains started to dissociate and repel each other, causing PAA to swell and dissolve into the buffer solution. As a result, 40 percent of the entrapped BSA was released from the sample, suggesting a good pH responsive capability of their material. Additionally, PAA was found to be able to protect proteins from enzymatic degradation. By comparing the UV-CD spectra of native and released BSA, they concluded that the BSA conformation has not been severely altered by the adsorption process, inferring a well-preserved protein activity. They envisioned that this material has the potential for the oral delivery of protein drugs to the target sites with higher pH, such as small intestine or colon.

Covalently-immobilized PAA on MSN materials was studied as a pH-sensitive drug delivery system by the Hong research group using a reversible addition-fragmentation chain transfer (RAFT) polymerization of acrylic acid (Fig. 5).[59] In this example, 5,6-Epoxyhexyltriethoxysilane was grafted on the MSNs, followed by the template removal. A RAFT agent, S-1-dodecyl-S-(α,α'-dimethyl-α''-acetic acid)trithiocarbonate, was attached to the MSNs exterior surface through an esterification reaction with the hydroxyl groups. Finally, acrylic acid was allowed to polymerize under vacuum to form a covalently-bonded PAA nanoshell coating on the MSNs. The structure of PAA nanoshell was highly dependent on the pH value of the medium. At pH 8.0, the PAA nanoshell is deprotonated and soluble in aqueous solutions, thus forming an open state with accessible pore entrances. However, when the pH drops below 4.0, the PAA nanoshell becomes insoluble and collapses onto the surface of MSNs, rendering a compact layer. Fluorescein

was used to evaluate the pH-regulated drug release performance of the PAA coated MSNs. They observed both fluorescein uptake and release by PAA coated MSNs at pH 8.0, but neither was detected with the same material at pH 4.0. Their results verified that the PAA coated MSNs can reversibly regulate the loading and releasing of guest molecules by adjusting pH values.

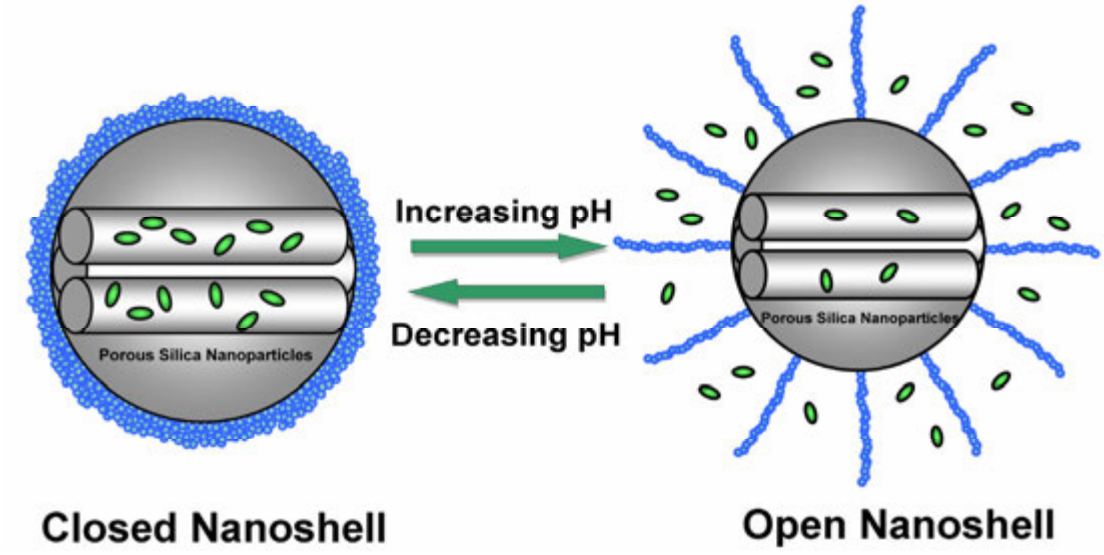

Figure 5. Schematic graph of opening and closing of the core-shell structured nanoparticle triggered by pH.

The unique structural and physiochemical properties of pseudorotaxanes have been exploited for the fabrication of a series of pH-responsive drug delivery devices. In a system reported by Kim and coworkers, low molecular weight polyethyleneimine (PEI, M_n = 1100) and cyclodextrin (CD) were assembled onto the surface of MSNs as the rod and the ring components.[60] PEI was grafted by a 1,1'-carbonyldiimidazol catalyzed reaction with carboxylic group functionalized MSNs. Calcein was then loaded as a guest molecule to the PEI-MSN hybrid material. Self-assembly of CDs (ring) with PEI (rod) was carried out under basic conditions, at which the CD was able to form hydrogen bonding with the deprotonated nitrogen atoms of PEI. Both α-CD and γ-CD showed effective blockage of the pores, whereas β-CD did not form a stable pseudorotaxane with PEI. The pH values of the suspensions of the calcein-loaded samples were adjusted from 11 to 5.5 to examine the "dethreading" of CD and the consequent releasing of calcein. Only weak fluorescence intensity was observed at high pH value. But an immediate increase in the fluorescence intensity was measured upon acidification of the solution to

pH 5.5. The system provided an example of pseudorotaxane based MSNs for pH-regulated drug delivery. However, the harsh working condition remains a concern for practical applications.

Similar constitution of pseudorotaxane has been created by Stoddart and Zink and coworkers.[61] The threading axis was a bisammonium stalk and cucurbit[6]uril (CB[6]) was used as the ring unit. Aminopropyl-functionalized MSNs were suspended in a methanol solution of propargyl bromide to obtain alkyne-terminated silica nanoparticles. After a loading with rhodamine B (RhB), the material was capped with CB[6]-disubstituted 1,2,3-triazole pseudorotaxanes by means of a CB[6]-catalyzed 1,3-dipolar cycloaddition of alkyne groups on MSNs and 2-azidoethylamine. At neutral and acidic environments, the CB[6] encircle the bisammonium stalk tightly through ion-dipolar interactions. Raising the pH value results in deprotonation of the stalk and dethreading of CB[6], and subsequent unblocking of the pores. They also discovered that the use of a shorter stalk would bring the CB[6] ring closer to the surface of MSNs and strengthen its ability of preventing leakage. They proposed that their system can be tuned to operate under gentler pH by switching to other bisammonium ion centers with favorable pK_a values.

The same research group later constructed a CB[6]-trisammonium pseudorotaxane based MSNs that could release guest molecules at either elevated or reduced pH values.[62] The trisammonium stalk consists of a tetra-methylenediammonium group and an anilinium group. The anilinium nitrogen atom is 10^6-fold less basic than the alkyl nitrogen atoms. Therefore, it stays unprotonated at neutral conditions, leaving the CB[6] ring residing on the tetra-methyleneammonium unit to block the pore channels. When the pH increased, all of the nitrogen atoms become deprotonated, resulting in the dethreading of the CB[6] ring. Otherwise, at lower pH with all nitrogen atoms protonated, the CB[6] moiety shuttles to the distal hexamethylenediammonium unit because its ion-dipole complexation is an order of magnitude greater of the six-carbon spacer than that of the four-carbon spacer. In both cases, the motion of CB[6] gives rise to the pore opening and controlled release of drugs. Furthermore, they demonstrated that the release profiles were different for aniline and *p*-anisidine functionalities due to their distinct pK_a values. It is conceivable that the material sensitivity to specific pH values for their material can be rationally tuned by selecting appropriately substituted anilines.

5.2 Light-triggered Release

Light irradiation is a convenient remote control approach for site-specific drug delivery. The uptake and release of guest molecules can be rapidly induced upon exposure to light with certain wavelengths. After Tanaka and coworkers first demonstration of a coumarin functionalized MSN material to manipulate drug release as previously discussed, photochemical responsive linkers such as azobenzene, *o*-nitrobenzyl ester and thymine bases are incorporated onto the surface of MSNs to render them photochemically susceptible for light controlled release.

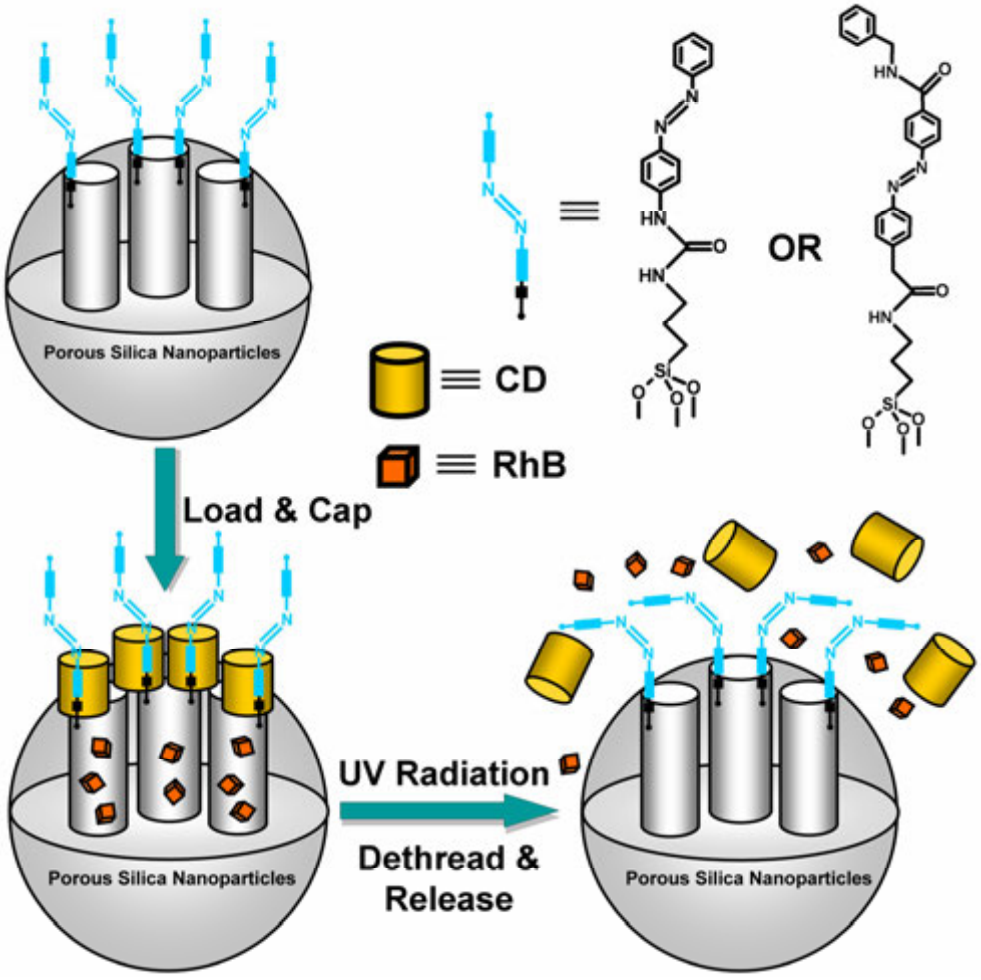

Figure 6. Schematic representation illustrating the capping of MSNs by Py-β-CD based pseudorotaxane, and the dethreading of pseudorotaxane upon UV radiation.

By varying the stalk and ring components, the pseudorotaxanes approach was also applied to control drug release with light (Fig. 6). Zink, Stoddart and coworkers constituted a photosensitive pseudorotaxane of azobenzene derivative (AB) and β-cyclodextrin (β-CD).[63] Unfunctionalized MSNs were grafted with 4-(3-triethoxylsilyl-

propylureido)azobenzene (TSUA) groups or more water-soluble (E)-4-((4-(benzyl-carbamoyl)phenyl)diazenyl)benzoic acid groups, as the pseudorotaxane stalks. Upon irradiation to 351 nm light, both azobenzene derivatives isomerized from the more stable *trans* form to a less stable *cis* configuration. β-CD or fluorescently labeled pyrene-β-cyclodextrin (Py-β-CD) were then introduced. The high binding affinity between *trans*-AB and β-CD locked the β-CD rings at the orifice. On the other hand, owing to the weak binding between *cis*-AB and β-CD, the isomerization of *trans*- to *cis*-AB stalks led to the dissociation of pseudorotaxanes, thus permitting the release of cargo molecules. Experimental data confirmed that the AB stalks and Py-β-CD assembly was stable without 351 nm UV radiation, whereas a complete Py-β-CD dissociation was determined when the sample was exposed to a 351 nm excitation beam for 400 minutes. Likewise, results from RhB loaded samples revealed that more than 90 percent of RhB was released from the laser light exposed sample, while less than 30 percent was released from the unexposed one, over a period of 7 hours. They concluded that their material was applicable to light-operated intracellular drug delivery systems.

Cyclodextrin was also employed by the Kim group to cover the porous reservoirs.[64] In their work, MSN materials were functionalized with aminopropyl groups, which were then treated with succinic anhydride in the presence of triethylamine to generate a carboxylic acid terminated MSNs sample. The sample was further functionalized by alkyne end groups through a coupling reaction with 2-nitro-5-(2-propyn-1-yloxy)-benzenemethanol, producing a photosensitive *o*-nitrobenzyl ester moiety that would decompose upon UV light exposure at 350 nm. Following a calcein dye loading, the pores were capped with the mono-6-azido-β-CD, by the Huigsen 1,3-dipolar cycloaddition reaction. In order to test the feasibility of their approach, the fluorescence intensity of the CD-capped calcein-loaded MSNs sample suspension was monitored over time. Only a very weak signal was detected in the dark, indicating that the calcein molecules were retained inside the pores. When the sample was irradiated with UV light, a remarkable increase in the fluorescence intensity was observed due to the photolysis of *o*-nitrobenzyl ester linkage and the diffusion of CD and calcein molecules. Furthermore, they noted a periodic release behavior of their sample in response to successive UV irradiation over short periods of time.

Gold nanoparticles, for the demonstrated excellent biocompatibility, were used as pore-blocking caps in a research conducted by Lin and coworkers (Fig. 7).[40] A

photoresponsive linker, thioundecyl-tetraethyleneglycolester-*o*-nitrobenzylethyldimethyl ammonium bromide, was immobilized onto the surface of Au nanoparticles (PR-AuNPs). These positively charged species then attached on the negatively charged MSN materials through the electrostatic interaction to produce a PR-AuNP capped MSNs system, the structure of which was later confirmed by transmission electron microscopy (TEM). A good capping efficiency was verified by the fact that no release of cargo was found even after 80 hours in the dark. Photoirradiation at 365 nm resulted in the cleavage of the *o*-nitrobenzyl ester containing linker, forming the negatively charged, thioundecyltetraethyleneglycolcarboxylate functionalized Au nanoparticles. Hence, the charge repulsion between Au nanoparticles and MSNs uncovered the pores and allowed the diffusion of guest molecules. In addition, intracellular studies were executed using an anticancer drug as cargo for the controlled release in human liver and fibroblast cells. Both cell lines were incubated with either drug-loaded sample or drug-free sample and were either exposed to light or kept in the dark. Only cells exposed to UV light with internalized drug-loaded MSNs caused significant cell death greater than 50 percent, suggesting that this system could indeed transport and release drug molecules inside live human cells under the control of photoirradiation.

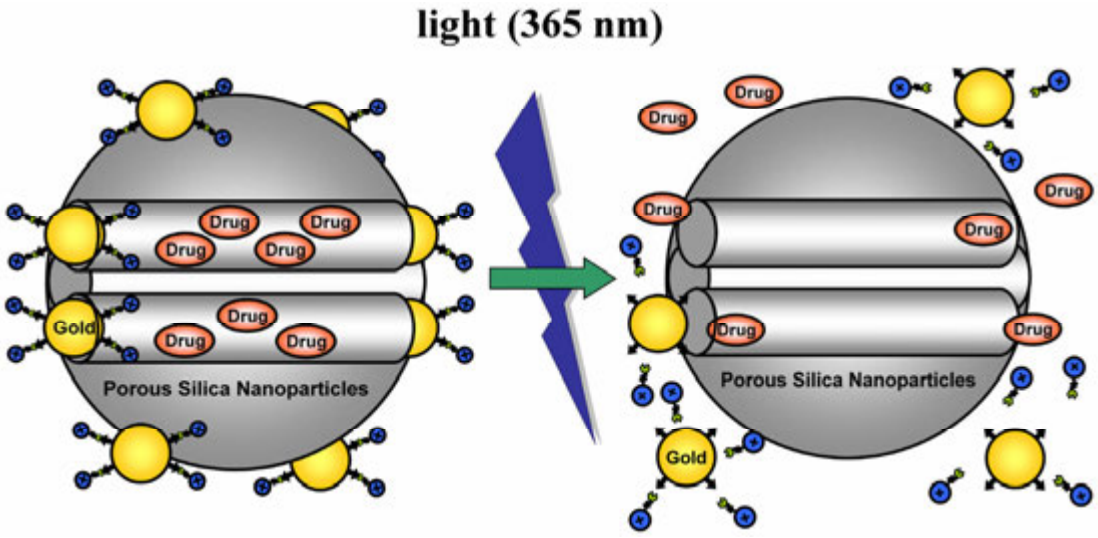

Figure 7. Schematic illustration of photo-induced controlled drug release of PR-AuNPs capped MSNs.

Thymine bases are a group of molecules that undergo photodimerization and revert back to monomeric thymines upon light irradiation above and below 270 nm, respectively. He et al. functionalized MSNs with thymine and loaded the cavities with a $Ru(bipy)_3^{2+}$

dye.[65] Irradiation with 365 nm UV light led to the formation of a cyclobutane ring and thus covered the pore outlets. A reversed photoreaction was triggered by exposure to 240 nm light, along with a release of 80 percent of loaded $Ru(bipy)_3^{2+}$. Their study provided another illustration for light-triggered drug delivery.

5.3 Redox Potential-triggered Release

The designs of redox responsive linkers are mainly based on the disulfide bond. It draws much interest in these systems because of its relative stability in plasma and is reversible. Intracellular antioxidant species levels are 100 to 1000 fold higher than that in the extracellular space, resulting in a high redox potential difference between the oxidizing extracellular space and the reducing intracellular space.[66] This difference is more significant in cancer cells than that in healthy cells, which renders the disulfide linkage more vulnerable in cancer cells leading to potentially higher drug concentrations at tumor sites. Thus, the demand for both outstanding delivery efficiency and minimized cytotoxicity can be realized by MSN based drug delivery systems.

The feasibility of the redox-responsive linkage has been well established and reported in a number of recent publications. In addition to the original CdS-capped MSN materials, Lin and coworkers refined the system by replacing the CdS caps to more biocompatible superparamagnetic iron oxide (Fe_3O_4) nanoparticles.[37] MSNs were functionalized with 3-(propyldisulfanyl)propionic acid and incubated in a fluorescein solution. 3-amino-propylsiloxyl coated Fe_3O_4 nanoparticles were then allowed to react with the carboxyl groups of MSNs to form a covalent amide bond. Less than 1 percent of fluorescein leaching was observed after 130 hr in a PBS suspension. A drastic release of 40 percent of loaded fluorescein was observed within 2 days upon the addition of DTT or dihydrolipoic acid, an antioxidant naturally present in the cells. A series of cell biological studies further confirmed successful endocytosis and intracellular fluorescein cargo release. Additionally, when a magnet was placed on the side of a cuvette, HeLa cells with internalized magnetic Fe_3O_4-capped MSNs were shown migrating across the cuvette. Confocal fluorescence microscopy images of the HeLa cells cultured with Fe_3O_4-capped MSNs for 10 hr revealed green fluorescent cell bodies, proving that the disulfide bond cleavage and uncapping process took place after the MSN materials were internalization by the cells.

Not limiting to inorganic nanoparticles, polymers such as polyelectrolytes multilayers (PEM) have also been employed to inhibit premature release. Yang, Wang and coworkers synthesized MSNs with disulfide bond cross-linked multilayers of poly-(vinlypyrrolidone) and thiolated poly-(methacrylic acid) by through a layer-by-layer method.[67] No detectable release of loaded FITC can be observed after a 24-hour incubation. Treatment with DTT caused the deconstruction of polyelectrolytes and the subsequent release of the encapsulated FITC. The PEM-MSNs were further conjugated with a cancer-specific DNA aptamer for cell targeting. A cell viability study results showed that doxorubicin (DOX) loaded PEM-MSN-aptamer samples led to more pronounced cancer cell death and non-cancer cell viability than the aptamer-free sample, demonstrating a redox-responsive controlled drug release system with targeted delivery ability.

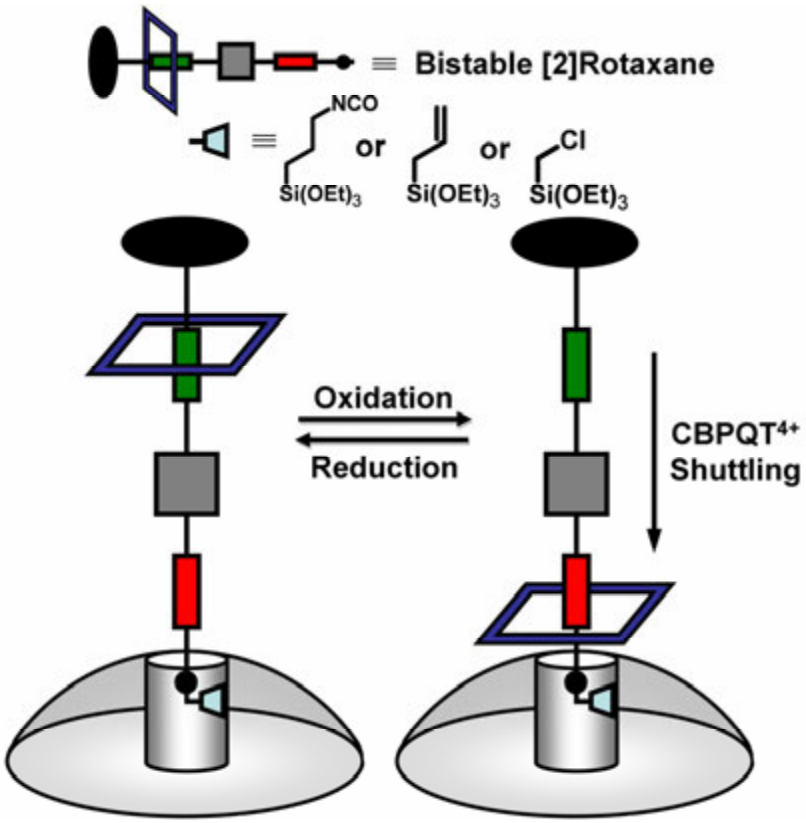

Figure 8. Graphical representaions of the assembly of the bistable [2]rotaxanes to form nanovalves and the possible positions (IN and OUT) regulated by the oxidation state. The cycle can be repeated several times.

A series of pseudorotaxanes have been developed in the Zink research group (Fig. 8).[68] In their first attempt, 1,5-dioxynaphthalene containing derivatives (DNPD) were

tethered to the surface of the MSNs, acting as the pseudorotaxane rod, followed by the assembly of cyclobis(paraquat-*p*-phenylene) ($CBPQT^{4+}$), which noncovalently complexed with DNPD. The bulky $CBPQT^{4+}$ tetracations thus obstruct the pore openings. The sample was loaded with a fluorescent dye, tris(2,2'-phenylpyridyl)iridium(III), to investigate the release behavior of this complex system. Upon addition of reducing agent, the pseudorotaxanes on the MSNs surface immediately dethreaded and opened up the pores. A fast increase in luminescence intensity was observed, indicating a rapid release of entrapped molecules.

The system was improved by including a second recognition site derived from tetrathiafulvalene (TTF).[69] A much stronger binding affinity between $CBPQT^{4+}$ and TTF exists than between $CBPQT^{4+}$ and DNPD, which ensured that over 95 percent of the $CBPQT^{4+}$ rings encircled the TTF station. However, oxidization of the TTF component to TTF^{2+} would destabilize such interaction and repel the $CBPQT^{4+}$ rings to shuttle along the axis to the DNPD recognition sites. This process is reversible upon the addition of a reducing agent such as ascorbic acid so that the $CBPQT^{4+}$ ring returns to the thermally favored TTF sites. They later established a general trend for the optimal design of their system: small guest molecules require short linkers and large guest molecules require long linkers.

5.4 Temperature-triggered Release

The local temperature difference between tumor sites and nontumor sites has been shown to be useful as an internal trigger for the control release of drugs. It is desirable to design a temperature-responsive drug carrier that only releases drugs at temperatures above 37 °C, but keeps drugs encapsulated while in circulation. Poly(*N*-isopropyl-acrylamide) (PNiPAm), a popular thermal-sensitive polymer, has been functionalized onto MSNs to modulate the transport of guest molecules.[70-74] It holds a low critical solution temperature (LCST) close to 37 °C,[75] below which the PNiPAm is hydrated and swollen so that it covers the cavities of MSNs. While at temperatures above LCST, the PNiPAm undergoes a conformation change to a hydrophobic, shrunken state in aqueous solution, and thus opening up the pore entrance.[76,77]

Initial studies were conducted by Lopez and coworkers, where they demonstrated three different approaches to prepare hybrid PNiPAm-functionalized MSNs.[70-72] In their first method, PNiPAm was mixed with silica precursors at the condensation stage, giving

rise to a sample with random porosity.[70] The product was found not feasible as a drug carrier due to its limited mass transport property. Their second mechanism was to form a copolymer of *N*-isopropylacrylamide (NiPAm) and 3-methacryloxypropyl-trimethoxysilane through free radical polymerization.[72] Then, the PNiPAm-silane copolymer was allowed to co-condense with TEOS to obtain PNiPAm-functionalized MSNs. But the particles were too large to be applied for intracellular application. So a third approach was proposed by growing PNiPAm on the external surface of pre-synthesized MSNs.[71] This method is widely used because the size of MSNs can be very well controlled.[73,74] Typically, a polymerization initiator, 1-(trichlorosilyl)-2-(*m/p*-(chloromethyl)phenyl)ethane was grafted onto MSNs, followed by an *in situ* atom-transfer radical polymerization of monomers at a slow and uniform rate to prevent clogging of the pores with free polymers. Additionally, the degree of polymerization could be tuned. It was further demonstrated that the PNiPAm-coated MSNs material was capable to uptake fluorescein molecules at low temperatures and release them at temperatures above LCST. Investigations in the cell biological properties of PNiPAm-coated MSNs showed no acute cytotoxicity and good endocytosis efficiency on human breast carcinoma cells. Successful intracellular release of a fluorescent dye at elevated temperature was observed by confocal fluorescence microscopy.

Another thermal-responsive uncapping mechanism was developed based on DNA oligomers. The Bein group. attached biotin-labeled DNA double strands onto the external surface of MSNs by click chemistry.[78] Avidin proteins were then coordinated with biotin and capped the pores of the nanoparticles. Upon temperature increase, the DNA double strands would dehybridize and release the biotin-avidin moiety into suspension, reaching an "open state". By picking different lengths of DNA oligomers, they were able to control the temperature threshold for gate-opening. This DNA dehybridization induced uncapping mechanism enables a precise adjustment for desired applications.

5.5 Enzyme-triggered Release

The development of smart, controlled-release delivery systems triggered by biomolecules such as enzymes is a very promising research direction, owing to their excellent biocompatibilities and their rapid and specific biological activities.

An enzyme-responsive cyclodextrin containing rotaxane was reported by Patel et al (Fig. 9).[79] MSNs were functionalized with monoazide-terminated triethyleneglycol by a

two-step grafting process. After soaking the MSN materials in a solution of RhB, α-CD was threaded onto the triethyleneglycol chain and effectively blocked the pores. A bulky adamantyl ester-linked stopper group was tethered to the terminal azide groups by Huisgen cycloaddition, and hence interlocked α-CD to the rotaxane stalk. An enzyme triggered release was verified by the addition of porcine liver esterase which broke the ester bonds on the stopper groups and enabled α-CD rings to escape from the triethyleneglycol thread, therefore permitting the diffusion of cargo molecules. It is interesting to note that when the ester bond of the stopper group was replaced by amide bond, it was no longer activated by esterase cleavage, demonstrating a high selectivity of the enzyme.

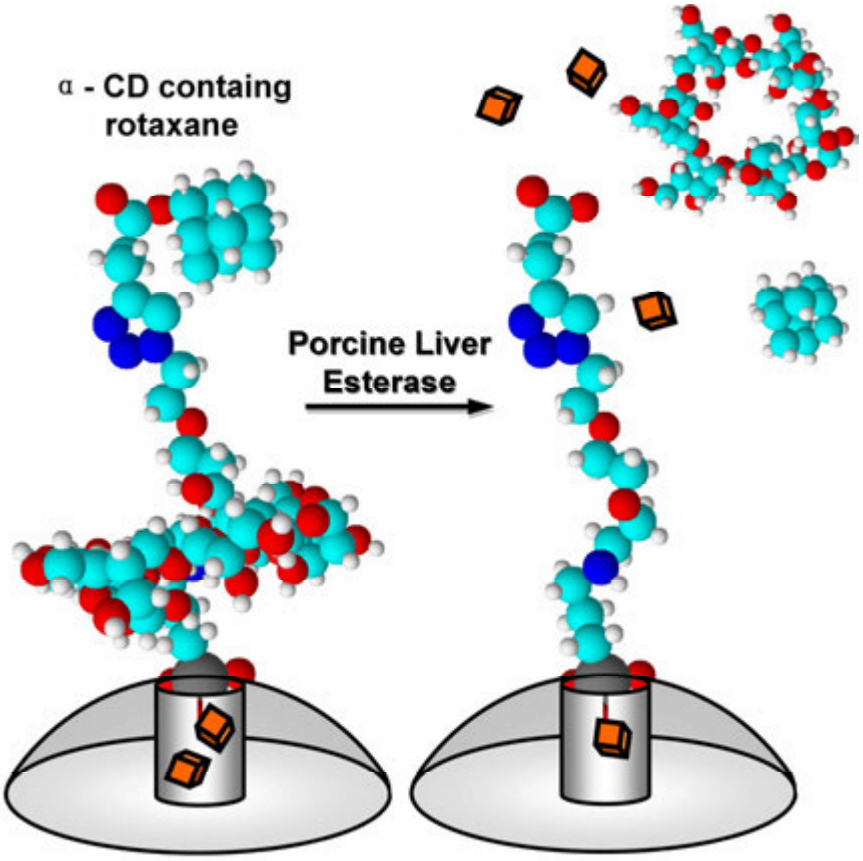

Figure 9. Esterase activated pore opening of α-CD containing rotaxane capped MSNs.

An extensively applied linker system is the biotin-avidin linker first prepared by Bein and coworkers, synthesizing biotinylated MSNs by a reaction of thiol-functionalized MSNs and biotin-maleimide.[80] The avidin caps were then strongly complexed to the biotin terminals on the MSNs, forming a tight closure of the pores. The avidin-biotin linked MSNs exhibited zero release until the addition of protease trypsin, which digested

avidin by the tryptic hydrolysis process and led to the release of guest molecules. Release reached completion after 140 minutes following the treatment of trypsin. The biotin-avidin linker was also useful for the targeted drug delivery.

Another approach to develop enzyme-sensitive linkers was reported by Bernardos et al.[81] MSNs as a starting material was loaded with $[Ru(bipy)_3]Cl_2$ for monitoring the enzyme-controlled release process. This sample was then capped with β-D-galactose and β-D-glucose disaccharides linked triethoxysilane. The capped sample was resuspended in a pH 7.5 buffer solution. Only a negligible release of cargo was observed after 5 hours. In contrast, the addition of β-D-galactosidase hydrolyzed the glycosidic bond, resulted in a decrease in the size of the capping agent, and induced $[Ru(bipy)_3]Cl_2$ cargo release. They also demonstrated that when the capped sample was treated with either digestive pepsin or denatured β-D-galactosidase, no release was observed, demonstrating that β-D-galactosidase was responsible for the dye release in their experiments.

5.6 Other Stimuli

A novel biocompatible surfactant-assisted controlled release system was proposed by Tsai and Trewyn et al.[82] The high cytotoxicity has always been a defect of the traditional cetyltrimethylammonium pore template, therefore the surfactant molecules have to be adequately removed before administration. To avoid this problem, a non-cytotoxic anionic surfactant, undec-1-en-11-yltetra(ethylene glycol) phosphate monoester (PMES), was developed to function as a structure directing agent. The presence of hydrophobic tails on the surfactants makes this material especially effective for the uptake of hydrophobic molecules. The MSNs with PMES (PMES-MSNs) sample possess a four fold greater loading ability for hydrophobic molecules in comparison to the calcined sample. Release of guest molecules occurred in conjunction with the diffusion of PMES surfactants when the drug-loaded PMES-MSNs were suspended in a PBS solution. The authors confirmed good biocompatibility and high cellular uptake efficiency for the PMES-MSN materials. In addition, an intracellular release of a hydrophobic drug (doxorubicin) was exemplified with Chinese Hamster Ovarian cells.

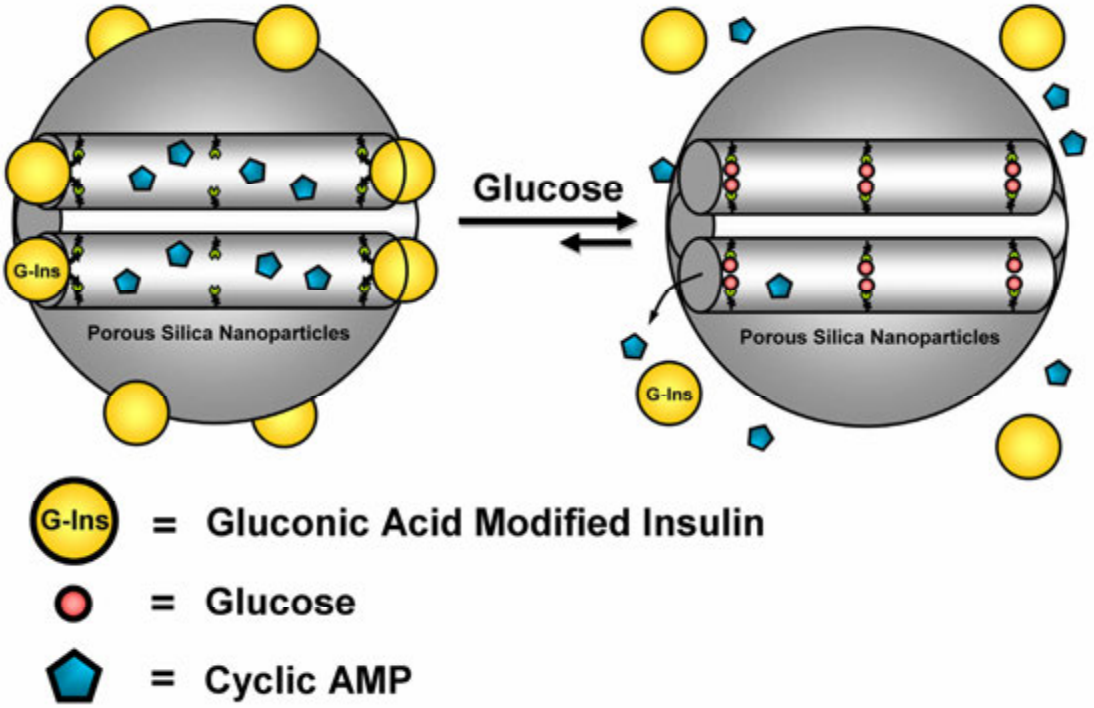

Figure 10. Schematic illustration of the glucose-responsive MSN based delivery system for controlled release of bioactive G-Ins and cAMP.

A glucose-responsive delivery system was fabricated by Lin and coworkers consisting of phenylboronic acid modified MSNs (BA-MSNs) and gluconic acid modified insulin (G-Ins) (Fig. 10).[83] The G-Ins serving as caps were attached to BA-MSNs through reversible covalent bonding between the vicinal diols of G-Ins and the phenylboronic acid groups on BA-MSNs. Release of guest molecules can be triggered by introducing saccharides such as glucose, which forms much more stable cyclic esters with phenylboronic acid than the acyclic diols and hence substitutes G-Ins moieties. This system is especially promising for the treatment of diabetes because it responds only at diabetic glucose levels while remains intact at normal conditions. Moreover, cyclic adenosine monophosphate (cAMP), known as an insulin secretion stimulating agent, can be encapsulated inside the pores and released subsequent to G-Ins diffusion to achieve a synergic effect for the regulation of blood glucose levels.

The antigen-antibody pair is another strong and specific binding linker for controlled release. Climent et al. first anchored the outer surface of MSNs with a derivative of the hapten 4-(4-aminobenzenesulfonylamino)benzoic acid and the orifices were blocked when a polyclonal antibody of sulfathiazole bound to the surface functional group.[84] The

delivery protocol of entrapped molecules occurred through a displacement reaction of the sulfathiazole-antibody pairs. Experimental results showed that release efficiency was closely associated with the concentration of sulfathiazole in the buffer solution. The delivery behavior was also determined to be antigen-specific, which makes their approach appealing for customizing controlled delivery devices.

A biomolecule-sensitive controlled release system was also reported by Yang and coworkers.[85] This modulating scheme took advantage of specific aptamer-target interactions. Adenosine-functionalized MSNs were synthesized through amide coupling of amine-modified MSNs and adenosine-5'-carboxylic acid. ATP aptamer-immobilized gold nanoparticles were employed as capping agents since the aptamers recognized and attached to the adenosine moieties on the MSNs. The gold nanoparticle caps sufficiently inhibited cargo release in the absence of ATP molecules. In contrast, in the presence of aptamer target molecules, a competitive displacement reaction destroyed the aptamer-adenosine interaction and, thus, cleaved the gold caps from the exterior surface of the MSNs. Significant release of cargo was observed. A high specificity of ATP-aptamer affinity was evaluated by comparing the release profiles triggered by ATP, CTP, GTP and UTP. It is noteworthy that other than ATP molecules, the complementary oligonucleotides (cDNA) are also able to selectively and efficiently bind to aptamers and trigger the cargo delivery.

Ultrasound can serve as a noninvasive external stimulus to achieve localized drug delivery. In the work by Honma and coworkers, MSNs were coated with poly(dimethylsiloxane), which restricted the diffusion of drug molecules.[86] On the other hand, ultrasound irradiation could enhance the permeability of water and drug molecules through the polymer layer, which is explained by the cavitation effect. Diffusion coefficient was four times higher for the ultrasound treated sample than that of the sample under nonultrasound conditions. Moreover, their material also revealed a regular pulsatile release pattern with repeated ultrasound irradiation.

The Martínez-Máñez and Stroeve research groups constructed a series of alkyl chain anchored MSNs to control delivery modulation.[87] Pore outlets were decorated with alkylsilanes of variant chain length, as diffusion controllers. They demonstrated that longer alkyl chains led to a slower releasing rate. Therefore, mass transport can be regulated artificially.

Releasing rates can also be tuned by controlling pore sizes. In a recent study by Gao et al., MSNs with pore sizes of 3.2 nm, 6.1 nm and 12.6 nm were prepared and all three materials were loaded with DOX, a typical chemotherapeutic agent.[88] Through a series of investigations on *in vitro* cytotoxicity, cellular uptake efficiency, intracellular drug release behavior, permeability glycoprotein expression and ATP levels of a drug-resistant cell line (MCF-7/ADR), they claimed that MSNs with a larger pore size could suppress cancer cells more effectively due to a faster release of DOX and a better endocytosis efficiency than MSNs with smaller pores.

5.7 Multiple Stimuli Triggered Release

Along with the extensive research conducted on single stimulus triggered drug delivery, multi-responsive controlled release systems have been developed to achieve complex release behaviors in either an independent or a synergistic fashion.

A dual pH and light controlled release system based on the combination of pH-sensitive pseudorotaxane and photo-sensitive nanoimpeller azobenzene was designed by Angelos et al.[89] A silylated azobenzene derivative was co-condensed with TEOS to produce pore surface functionalized MSNs and CB[6]/bisalkylammonium containing pseudorotaxane was anchored on the exterior surface of MSNs. They illustrated that this material could function as AND logic gates, such that cargo delivery occurred only when it was triggered by both stimuli. They envisioned that it is possible to manually regulate delivery dosage with this system.

Another pH and photo-switch release approach was demonstrated by Aznar et al.[90] They employed a boronate ester linker formed between saccharide functionalized MSNs and boronic acid anchored gold nanoparticle caps. Two opening protocols were proposed to break the boronate ester linkage. One is to lower the pH value to 3; the other is to irradiate the material with a laser beam at 1064 nm, which induces plasmon resonance excitation in Au nanoparticles to produce a photothermal effect. Both triggers were shown to be able to generate a pulsatile release of guest molecules by administrating stimulus repeatedly.

In another pseudorotaxane based MSNs reported by Kim and coworkers, three independent stimuli were confirmed to be capable to sufficiently unblock the pore voids.[91] The pseudorotaxane unit consisted of an *o*-nitrobenzene ester containing stalk and a β-CD ring. The stalk can either be ruptured by UV light irradiation or be

decomposed by lipase and the β-CD ring can be digested by α-amylase. Therefore, the release of guest molecules can be diversely triggered by enzymes or light individually, or by both to achieve a synergistic acceleration effect.

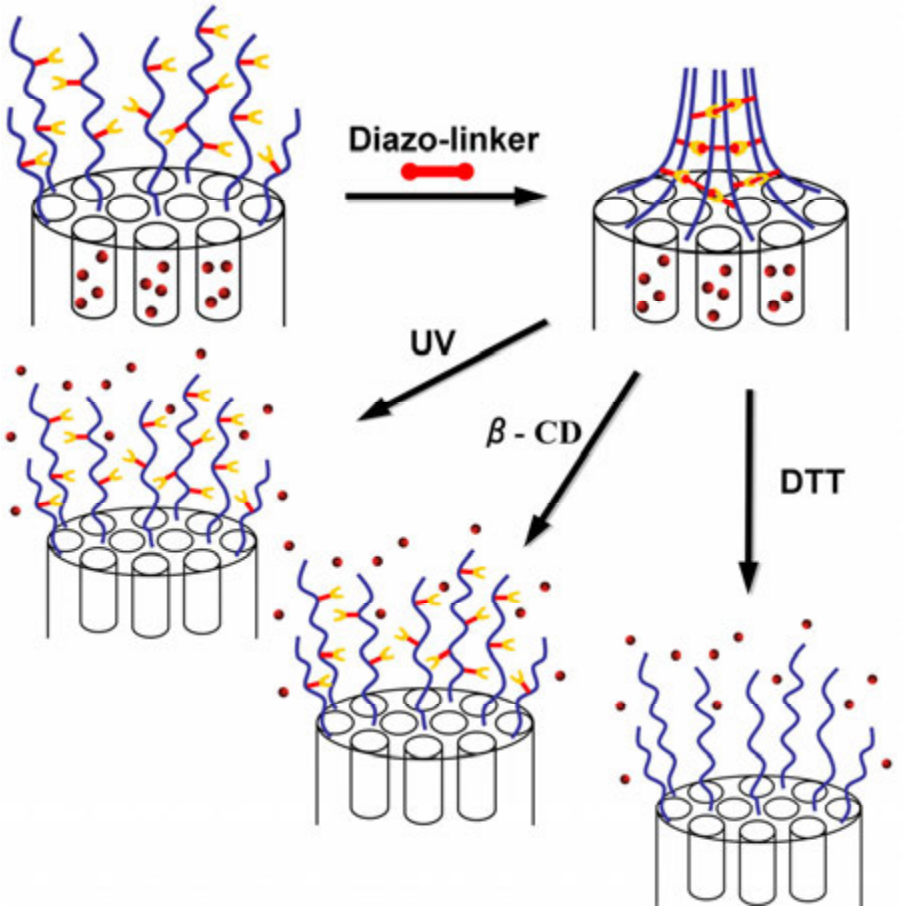

Figure 11. Schematic illustration of a multiresponsive nanogated ensemble based on supramolecular polymeric network-capped mesoporous silica nanoparticle.

A tri-stimuli responsive delivery system was developed by Feng and coworkers involving the construction of a pyridyldithio-containing polymer functionalized MSNs that were disulfide bond linked to thiol-modified β-CD (Fig. 11).[92] The β-CD moieties were further cross-linked by diazo-linkers to inhibit the release of entrapped molecules. Their assembly was expected to respond to UV light irradiation, as well as the addition of DTT or α-CD. Under a 365 nm UV light, the *trans*- configured diazo-linkers would transform into a *cis*-azobenzene and thus lose their high affinity to β-CD molecules. Addition of DTT would cleave the disulfide linkage between β-CD and MSNs. The introduction of excess α-CD would result in the formation of a more stable α-CD-diazo

cross-linkage and displace β-CD. In all three scenarios, the pore-blocking polymeric network was opened, leading to tri-stimuli triggered release.

The fact that magnetic nanocrystals are able to generate heat energy under high-frequency alternating magnetic field was applied in the design of temperature-responsive delivery systems by the Vallet-Regí group.[93] Magnetic iron oxide nanocrystals were embedded inside the silica matrix of MSNs and the surface of MSNs was decorated with a thermosensitive copolymer of poly(ethyleneimine)-*b*-poly-(*N*-isopropyl-acrylamide) (PEI/NIPAM). They demonstrated that this device could deliver proteins with preserved activity, triggered by a temperature increase, as well as an alternating magnetic field that heat up the local environment through encapsulated iron oxide nanocrystals.

6. Targeted Drug Delivery of Mesoporous Silica Nanoparticles

Cell-specific targeting is highly attractive as an approach to spontaneously distinguish the site of disease diagnosis, and as a result, this technique reduces drug administration dosage and diminishes toxic side-effects of drugs during circulation. Both passive strategies and active surface decoration methods have been applied to the fabrication of novel MSNs based drug delivery systems for targeted release.

6.1 Passive Routes

Passive accumulation of MSNs in tumor tissue can be realized by the enhanced permeability and retention (EPR) effect, a theory first postulated by Matsumura and Maeda in 1986.[94] They hypothesized that the differential localization of macromolecules as well as particles of certain sizes is attributed to the tumor microenvironment, the relative slow elimination rate and poor lymphatic drainage. Effectiveness of the EPR effect can be mediated by the particle size, surface charge or hydrophobicity. Tamanoi and coworkers demonstrated a preferential accumulation of fluorescently labeled MSNs (100-130 nm in diameter) in tumors of mice, within 4 hours of an intravenous injection. The fluorescent signal then gradually decreased to the same level as the whole body after 48 hr.[95] Similar phenomenon was also reported by the Hyeon group that MSNs less than 200 nm accumulated in tumor 24 hours after administration.[53]

6.2 Surface Decoration with Targeting Ligands

Efforts have been made to functionalize the surfaces of MSNs with cancer-specific targeting ligands for an enhanced MSNs uptake by cancer cells compared to noncancerous cells. One such ligand is folic acid,[96-98] as folate receptors are known to be overexpressed in several types of human cancer, including ovarian, endometrial, colorectal, breast and lung.[99] Using folic acid-conjugated MSNs (FA-MSNs), Sahlgren, Linden and coworkers observed that the total number of particles internalized by the HeLa cancer cells was about one order of magnitude higher than that of FA-MSNs internalized by noncancerous cells, although noncancerous cells normally do express folate receptors.[96] Besides folic acid, other small cell nutrient molecules such as mannose,[100] was also shown to selectively improve the uptake of MSNs by breast cancer cells.

Another group of targeting ligands is the RGD peptide, abbreviation for arginine-glycine-aspartic acid, which interacts with the highly overexpressed $\alpha_v\beta_3$ integrin receptor in metastatic cancers. Lo and coworkers verified an integrin-dependent endocytosis process of cyclic RGD (cRGD)-anchored MSNs by U87-MG cells.[35] Futhermore, Tamanoi, Zink and coworkers synthesized cRGD-modified MSNs, targeting metastatic cancer cells, as well as transferrin-modified MSNs, targeting transferrin receptor overexpressed primary cancer cells.[101] They observed a positive interaction between targeting ligands and upregulated receptors, they also envisaged that by altering the surface groups, the MSN based drug delivery systems can be manipulated to target different stages of cancers.

Further research on the RGD peptide facilitated cancer cell delivery was conducted by the Trewyn group,[102] where they determined that RGD modified MSNs remained in the endosomes for a longer period of time compared to MSNs without RGD ligand attached. Moreover, their results indicated that the conformation of the RGD peptide affects the uptake efficiency of RGD modified MSNs, where cyclic RGD peptides possess greater affinity to the cell membrane integrins and facilitate the endocytosis process better, comparing to linear RGD peptides. Other proteins or peptides such as monoclonal herceptin antibody or TAT peptide have also been immobilized onto MSNs and shown to increase the uptake efficiency by cancerous cells.[103,104]

Aptamers are recognized as molecule-specific targeting agents, so it is feasible to furnish MSNs with cell-specific aptamers for targeted delivery. In a work by Zhu et al., a

cancer-cell targeted DNA aptamer, sgc8, was selected as a recognition molecule.[67] Significant enhancement of Hela cell uptake of aptamer-conjugated MSNs comparing to aptamer-free MSNs was monitored by flow cytometry.

7. *In vivo* and *in planta* delivery with Mesoporous Silica Nanoparticles

7.1 *In vivo* Delivery

Despite the numerous studies that have demonstrated the *in vitro* therapy efficacy of MSNs based smart drug delivery systems, the feasibility of using MSNs for *in vivo* drug delivery has to be further evaluated. Recently, several groups have explored extended *in vivo* investigations. In Tamanoi's experiments on mice, camptothecin (CPT)-loaded MSNs showed to be effective in suppressing tumor growth.[95] For nude mice injected with CPT-loaded MSNs, the tumor significantly decreased in size or was completely eliminated by the end of treatment (52 days). Another important finding was that a targeting moiety functionalization dramatically increased tumor-suppressing effects of CPT-loaded MSNs.[105] Folic acid-modified MSNs induced an enhanced tumor inhibition and faster tumor regression than unmodified MSNs, suggesting a good targeting efficacy of folic acid.

In vivo therapeutic efficacy of MSNs based drug delivery system was also assessed by Chen and coworkers.[106] Mice with tumors of approximately 200 mm^3 were treated with docetaxel-loaded MSNs (Dtxl-MSNs), taxotere or physiological saline for 17 days. They observed that Dtxl-MSNs treatment decreased tumor weight to only 28 percent compared to the control group, which was also significantly lower than the tumor weight of the taxotere group. The enhanced tumor suppression of Dtxl-MSNs may be attributed to the sustained drug release as well as intratumor drug accumulation due to the EPR effect.

7.2 *In planta* Delivery

MSN systems have also been reported to overcome the rigid plant cell wall barrier and undergo plant cell internalization in a study by Lin, Wang and coworkers (Fig. 12).[107] First, they proved that MSNs functionalized with triethylene glycol (TEG-MSNs) was successfully internalized by tobacco mesophyll protoplasts. Using confocal fluorescence microscopy, they demonstrated TEG-MSNs can function as DNA delivery agents to efficiently carry green fluorescent protein (GFP) plasmid into protoplast cells and lead to

transgene expression. In depth applications for gene and guest molecules co-delivery with this system was inspected. A chemical trigger, β-estradiol, was loaded into inducible GFP-coated MSNs system and capped with gold nanoparticles by a redox-responsive disulfide linkage. Non-transgenic plants bombarded with this material exhibited gene transcription only after DTT triggered the release of β-estradiol. This methodology was also recently demonstrated and elaborated by the Wang and Trewyn research groups,[108] where they employed MSNs with large pore size (10 nm) to load and subsequently release active, non-denatured proteins, as well as plasmid DNA, to the same cell upon bombardment. Their findings indicated that MSNs based delivery system can be applied to plant science research to aid further investigations of plant genomics and gene function.

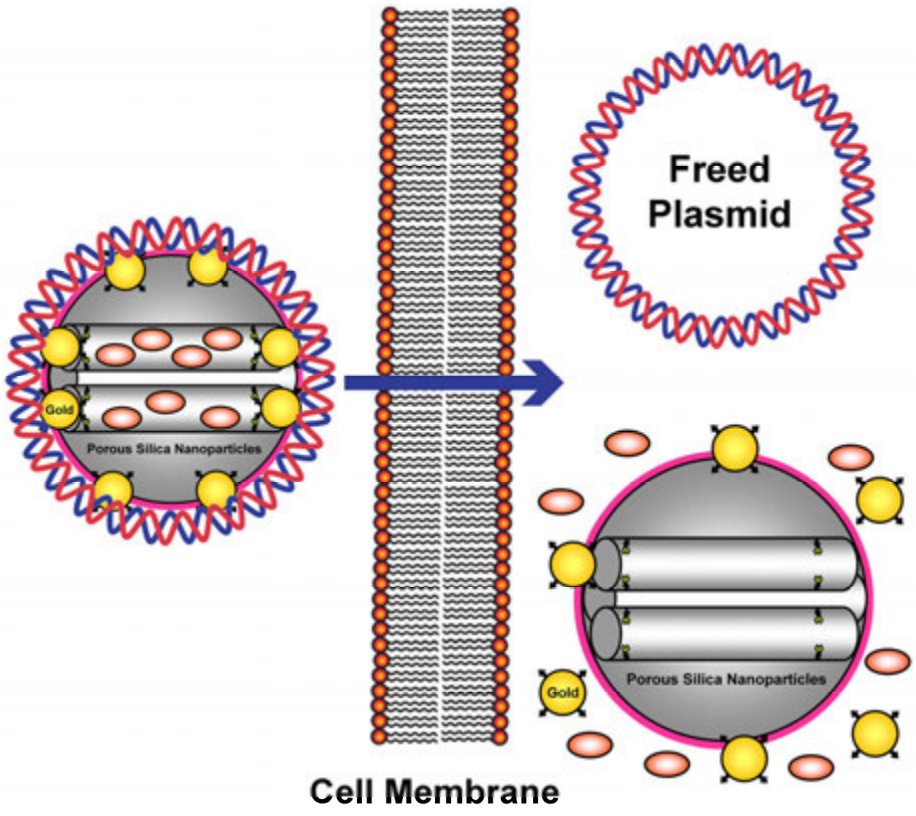

Figure 12. DNA plasmid-coated gold nanoparticle-capped mesoporous silica nanoparticle for the simultaneous delivery of a gene and its promoter into plant cells.

8. Conclusion

The emergence of MSN materials has been appreciated by the biomedical and plant science field for the design of smart drug delivery devices. The unique characteristics of MSNs have created a fast growing number of stimuli-responsive release systems. A high degree of specificity and control in drug delivery is achieved by versatile uncapping mechanisms and new approaches for MSN synthesis. However, despite the encouraging progress, these systems are mostly investigated outside the biological system, and have not yet been proven for *in vivo* biomedical applications. Although ingenious work is required to conquer remaining challenges, it is reasonable to believe that these multifunctional MSNs drug delivery systems will promote the development in clinical and other biotechnological fields.

REFERENCES

1. Svenson, S. 2004. *ACS Symposium Series.* 879:2-23.
2. Gref, R. and Y. Minamitake, M.T. Peracchia, V. Trubetskoy, V. Torchilin, and R. Langer. 1994. *Science.* 263(5153): 1600-1603.
3. Jeong, B. and Y.H. Bae, D.S. Lee, and S.W. Kim. 1997. *Nature.* 388:860-862.
4. Discher, B.M. and Y.-Y. Won, D.S. Ege, J. C.-M. Lee, F.S. Bates, D.E. Discher, and D.A. Hammer. 1999. *Science.* 284(5417): 1143-1146.
5. Torchilin, V.P. 2005. *Nat. Rev. Drug Discov.* 4(2):145-160.
6. Gao, C. and D. Yan. 2004. *Prog. Polym. Sci.* 29(3):183-275.
7. Lee, C.C. and J.A. Mackay, J.M.J. Frechet, and F.C. Szoka. 2005. *Nat. Biotechnol.* 23(12):1517-1526.
8. Peppas, N. A. and P. Bures, W. Leobandung, and H. Ichikawa. 2000. *Eur. J. Pharm. Biopharm.* 50(1):27-46.
9. Peppas, N. A. and J.Z. Hilt, A. Khademohosseini, and R. Langer. 2006. *Adv. Mater.* 18(11):1345-1360.
10. Lai, C.Y. and B.G. Trewyn, D.M. Jeftinija, K. Jeftinija, S. Xu, S. Jeftinija, and V.S.-Y. Lin. 2003. *J. Am. Soc. Chem.* 125(15):4451-4459.
11. Vivero-Escoto, J.L. and I.I. Slowing, B.G. Trewyn and V.S.-Y. Lin. 2010. *Small.* 6(18):1952-1967.
12. Kresge, C.T. and M.E. Leonowicz, W.J. Roth, J.C. Vartuli, and J.S. Beck. 1992. *Nature*. 359(6397):710-712.
13. Inagaki, S. and Y. Fukushima, and K. Kuroda. 1993. *J. Chem. Soc. Chem. Comm.* 8:680-682.
14. Hoffmann, F. and M. Cornelius, J. Morell, and M. Froeba. 2006. *Angew. Chem. Int. Ed.* 45(20):3216-3251.
15. Wan, Y. and D. Zhao. 2007. *Chem. Rev.* 107(7):2821-2860.
16. Vallet-Regí, M. and A. Ramila, R.P. del Real, and J. Perez-Pariente. 2001. *Chem. Mater.* 13(2):308-311.
17. Vallet-Regí, M. and F. Balas, and D. Arcos. 2007. *Angew. Chem. Int. Ed.* 46(40):7548-7558.
18. Trewyn, B.G. and S. Giri, I.I. Slowing, and V.S.-Y. Lin. 2007. *Chem. Comm.* 31:3236-3245.
19. Song, S.W. and K. Hidajat, and S. Kawi. 2005. *Langmuir*. 21(21):9568-9575.

20. Vartuli, J.C. and K.D. Schmitt, C.T. Kresge, W.J. Roth, M.E. Leonowicz, S.B. McCullen, S.D. Hellring, J.S. Beck, J.L. Schlenker, D.H. Olson, and E.W. Sheppard. 1994. *Chem. Mater.* 6(12):2117-2326.
21. Cai, Q. and W.-Y. Lin, F.-S. Xiao, W.-Q. Pang, X.-H. Chen, and B.-S. Zou. 1999. *Micropor. Mesopor. Mater.* 32(1-2):1-15.
22. Huo, Q. and R. Leon, P.M. Petroff, and G.D. Stucky. 1995. *Science*. 268(5215):1324-1327.
23. Huo, Q. and D.I. Margolese, and G.D. Stucky. 1996. *Chem. Mater.* 8(5):1147-1160.
24. Zhao, D. and J. Feng, Q. Huo, N. Melosh, G.H. Frederickson, B.F. Chmelka, and G.D. Stucky. 1998. *Science*. 279(5350):548-552.
25. Zhao, D. and Q. Huo, J. Feng, B.F. Chmelka, and G.D. Stucky. 1998. J. *Am. Chem. Soc.* 120(24):6024-6036.
26. Beck, J.S. and J.C. Vartuli, W.J. Roth, M.E. Leonowicz, C.T. Kresge, K.D. Schmitt, C.T.-W. Chu, D.H. Olson, E.W. Sheppard, S.B. McCullen, J.B. Higgins, and J.L. Schlenker. 1992. *J. Am. Chem. Soc.* 114(27):10834-10843.
27. Widenmeyer, M. and R. Anwander. 2002. *Chem. Mater.* 14(4):1827-1831.
28. Sayari, A. and P. Liu, M. Kruk, and M. Jaroniec. 1997. *Chem. Mater.* 9(11):2499-2506.
29. Huh, S. and J.W. Wiench, J.-C. Yoo, M. Pruski, and V.S.-Y. Lin. 2003. *Chem. Mater.* 15(22):4247-4256.
30. Huh, S. and J.W. Wiench, B.G. Trewyn, S. Song, M. Pruski, and V.S.-Y. Lin. 2003. *Chem. Comm.* 18:2364-2365.
31. Radu, D.R. and C.-Y. Lai, J. Huang, X. Shu, and V.S.-Y. Lin, 2005. *Chem. Comm.* 10:1264-1266.
32. Lim, M.H. and A. Stein. 1999. *Chem. Mater.* 11(11):3285-3295.
33. Radu, D.R. and C.-Y. Lai, J.W. Wiench, M. Pruski, and V.S.-Y. Lin. 2004. *J. Am. Chem. Soc.* 126(6):1640-1641.
34. De Juan, F. and E. Ruiz-Hitzky. 2000. *Adv. Mater.* 12(6):430-432.
35. Cheng, S.-H. and C.-H. Lee, M.-C. Chen, J.S. Souris, F.-G. Tseng, C.-S. Yang, C.-Y. Mou, C.-T. Chen, and L.-W. Lo. 2010. *J. Mater. Chem.* 20(29):6149-6157.
36. Radu. D.R. and C.-Y. Lai, K. Jeftinija, E.W. Rowe, S. Jeftinija, and V.S.-Y. Lin. 2004. *J. Am. Chem. Soc.* 126(41):13216-13217.

37. Giri, S. and B.G. Trewyn, M.P. Stellmaker, and V.S.-Y. Lin. 2005. *Angew. Chem. Int. Ed.* 44(32):5038-5044.
38. Slowing, I.I. and B.G. Trewyn, and V.S.-Y. Lin. 2006. *J. Am. Chem. Soc.* 128(46):14792-14793.
39. Slowing I.I. and B.G. Trewyn, and V.S.-Y. Lin. 2007. *J. Am. Chem. Soc.* 129(28):8845-8849.
40. Vivero-Escoto, J.L. and I.I. Slowing, C.-W. Wu, and V.S.-Y. Lin. 2009. *J. Am. Chem. Soc.* 131(10):3462-3463.
41. Prokop, A. and J.M. Davidson. 2008. *J. Pharm. Sci.* 97(9):3518-3590.
42. Trewyn, B.G. and J.A. Nieweg, Y. Zhao, and V.S.-Y. Lin. 2008. *Chem. Eng. J.* 137(1):23-29.
43. Lu, F. and S.-H. Wu, Y. Hung, and C.-Y. Mou. 2009. *Small*. 5(12):1408-1413.
44. Chung, T.-H. and S.-H. Wu, M. Yao, C.-W. Lu, Y.-S. Lin, Y. Hung, C.-Y. Mou, Y.-C. Chen, and D.-M. Huang. 2007. *Biomaterials*. 28(19):2959-2966.
45. Vallhov, H. and S. Gabrielsson, M. Stromme, A. Scheynius, and A.E. Garcia-Bennett. 2007. *Nano Lett.* 7(12):3576-3582.
46. Hudson, S.P. and R.F. Padera, R. Langer, and D.S. Kohane. 2008. *Biomaterials*. 29(30):4045-4055.
47. Jiang, W. and B.Y.S. Kim, J.T. Rutka, and W.C.W. Chan. 2008. *Nature. Nanotechnol.* 3(3):145-150.
48. He, X. and H. Nie, K. Wang, W. Tan, X. Wu, and P. Zhang. 2008. *Anal. Chem.* 80(24):9597-9603.
49. He, Q. and Z. Zhang, F. Gao, Y. Li, and J. Shi. 2011. *Small*. 7(2):271-280.
50. Huang, X. and L. Li, T. Liu, N. Hao, H. Liu, D. Chen, and F. Tang. 2011. *ACS Nano.* 5(7):5390-5399.
51. Lin, Y.-S. and C.L. Haynes. 2010. *J. Am. Chem. Soc.* 132(13):4834-4842.
52. Zhao, Y. and X. Sun, G. Zhang, B.G. Trewyn, I.I. Slowing, and V.-S.Y. Lin. 2011. *ACS Nano.* 5(2):1366-1375.
53. Kim, J. and H.S. Kim, N. Lee, T. Kim, H. Kim, T. Yu, I.C. Song, W.K. Moon, and T. Hyeon. 2008. *Angew. Chem. Int. Ed.* 47(44):8438-8441.
54. Wu, S.-H., Y.-S. Lin, Y. Hung, Y.-H. Chou, Y.-H. Hsu, C. Chang, and C.-Y. Mou. 2008. *Chembiochem.* 9(1):53-57.
55. Mal, N.K. and M. Fujiwara, and Y. Tanaka. 2003. *Nature*. 421(6921):350-353.

56. Casasus, R. and M.D. Marcos, R. Martínez-Máñez, J.V. Ros-Lis, J. Soto, L.A. Villaescusa, P. Amorós, D. Beltran, C. Guillem, and J. Latorre. 2004. *J. Am. Chem. Soc.* 126(28):8612-8613.
57. Bernardos, A. and E. Aznar, C. Coll, R. Martínez-Máñez, J. Barat, M.D. Marcos, F. Sancenon, A. Benito, and J. Soto. 2008. *J. Controlled Release.* 131(3):181-189.
58. Song, S.-W. and K. Hidajat, and S. Kawi. 2007. *Chem. Comm.* 42:4396-4398.
59. Hong, C.-Y. and X. Li, and C.-Y. Pan. 2009. J. Mater. Chem. 19(29):5155-5160.
60. Park, C. and K. Oh, S.C. Lee, and C. Kim. 2007. *Angew. Chem. Int. Ed.* 46(9):1455-1457.
61. Angelos, S. and Y.-W. Yang, K. Patel, J.F. Stoddart, and J.I. Zink. 2008. *Angew. Chem. Int. Ed.* 47(12):2222-2226.
62. Angelos, S. and N.M. Khashab, Y.-W. Yang, A. Trabolsi, H.A. Khatib, J.F. Stoddart, and J.I. Zink. 2009. *J. Am. Chem. Soc.* 131(36):12912-12914.
63. Ferris, D.P. and Y.-L. Zhao, N.M. Khashab, A. Hussam, J.F. Stoddart, and J.I. Zink. 2009. *J. Am. Chem. Soc.* 131(5):1686-1688.
64. Park, C. and K. Lee, and C. Kim. 2009. *Angew. Chem. Int. Ed.* 48(7):1275-1278.
65. He, D. and X. He, K. Wang, J. Cao, and Y. Zhao. 2012. *Langmuir*. 28(8):4003-4008.
66. Saito, G. and J.A. Joel, and K.-D. Lee. 2003. *Adv. Drug Deliv. Rev.* 55(2):199-215.
67. Zhu, C.-L. and X.-Y. Song, W.-H. Zhou, H.-H. Yang, Y.-H. Wen, and X.-R. Wang. 2009. *J. Mater. Chem.* 19(41):7765-7770.
68. Nguyen, T.D. and Y. Liu, S. Saha, K.C.-F. Leung, J.F. Stoddart, and J.I. Zink. 2007. *J. Am. Chem. Soc.* 129(3):626-634.
69. Nguyen, T.D. and H.-R. Tseng, P.C. Celestre, A.H. Flood, Y. Liu, J.F. Stoddart, and J.I. Zink. 2005. *Proc. Nat. Acad. Sci. USA*. 102(29):10029-10034.
70. Rao, G.V.R. and M.E. Krug, S. Balamurugan, H. Xu, Q. Xu, and G.P. Lopez. 2002. *Chem. Mater.* 14(12):5075-5080.
71. Fu, Q. and G.V.R. rao, L.K. Ista, Y. Wu, B.P. Andrzejewski, L.A. Sklar, T.L. Ward, and G.P. Lopez. 2003. *Adv. Mater.* 15(15):1262-1266.
72. Fu, Q. and G.V.R. Rao, T.L. Ward, Y. Lu, and G.P. Lopez. 2007. *Langmuir*. 23(1):170-174.
73. You, Y.-Z. and K.K. Kalebaila, S.L. Brock, and D. Oupicky. 2008. *Chem. Mater.* 20(10):3354-3359.

74. Yang, Y. and X. Yan, Y. Cui, Q. He, D. Li, A. Wang, J. Fei, and J. Li. 2008. *J. Mater. Chem.* 18(47):5731-5737.
75. Heskins, M. and J.E. Guillet. 1968. *J. Macro. Sci.* 2(8):1441-1455.
76. Pelton, R. 2000. *Adv. Colloid Interfac.* 85(1):1-33.
77. Li, D. and Y. Cui, K. Wang, Q. He, X. Yan, and J. Li. 2007. *Adv. Func. Mater.* 17(16):3134-3140.
78. Schlossbauer, A. and S. Warncke, P.M.E. Gramlich, J. Kecht, A. Manetto, T. Carell, and T. Bein. 2010. *Angew. Chem. Int. Ed.* 49(28):4734-4737.
79. Patel K. and S. Angelos, W.R. Dichtel, A. Coskun, Y.-W. Yanng, J.I. Zink, and J.F. Stoddart. 2008. *J. Am. Chem. Soc.* 130(8):2382-2383.
80. Schlossbauer, A. and J. Kecht, and T. Bein. 2009. *Angew. Chem. Int. Ed.* 48(17):3092-3095.
81. Bernardos, A. and E. Aznar, M.D. Marcos, R. Martínez-Máñez, F. Sancenon, J. Soto, J.M. Barat, M. Jose, and P. Amorós. 2009. *Angew. Chem. Int. Ed.* 48(32):5884-5887.
82. Tsai, C.-H. And J.L. Vivero-Escoto, I.I. Slowing, I.-J. Fang, B.G. Trewn, and V.S.-Y. Lin. 2011. *Biomaterials*. 32(26):6234-6244.
83. Zhao, Y. and B.G. Trewyn, I.I. Slowing, and V.S.-Y. Lin. 2009. *J. Am. Chem. Soc.* 131(24):8398-8400.
84. Climent, E. and A. Bernardos, R. Martínez-Máñez, A. Maquieira, M.D. Marcos, N. Pastor-Navarro, R. Puchades, F. Sancenon, J. Soto, and P. Amorós 2009. *J. Am. Chem. Soc.* 131(39):14075-14080.
85. Zhu, C.-L. and C.-H. Lu, X.-Y. Song, H.-H. Yang, and X.-R. Wang. 2011. *J. Am. Chem. Soc.* 133(5):1278-1281.
86. Kim, H.-J. and H. Matsuda, H. Zhou, and I. Honma. 2006. *Adv. Mater.* 18(23):3083-3088.
87. Aznar, E. and F. Sancenon, M.D. Marcos, R. Martínez-Máñez, P. Stroeve, J. Cano, and P. Amorós. 2012. *Langmuir*. 28(5):2986-2996.
88. Gao, Y. and Y. Chen, X. Ji, X. He, Q. Yin, Z. Zhang, J. Shi, and Y. Li. 2011. *ACS Nano* 5(12):9788-9798.
89. Angelos, S. and Y.-W. Yang, N.M. Khashab, J.F. Stoddart, and J.I. Zink. 2009. *J. Am. Chem. Soc.* 131(32):11344-11346.
90. Aznar, E. and M.D. Marcos, R. Martínez-Máñez, F. Sancenon, J. Soto, P. Amorós, and C. Guillem. 2009. *J. Am. Chem. Soc.* 131(19):6833-6843.

91. Park, C. and H. Kim, S. Kim and C. Kim, 2009. *J. Am. Chem. Soc.* 131(46):16614-16615.
92. Liu, R. and Y. Zhang, and P. Feng. 2009. *J. Am. Chem. Soc.* 131(42):15128-15129.
93. Baeza, A. and E. Guisasola, E. Ruiz-Hernandez, and M. Vallet-Regí. 2012. *Chem. Mater.* 24(3):517-524.
94. Matsumura, Y. and H. Maeda. 1986. *Cancer Res.* 46(12):6387-6392.
95. Lu, J. and M. Liong, Z. Li, J.I. Zink, and F. Tamanoi. 2010. *Small*. 6(16):1794-1805.
96. Rosenholm, J.M. and A. Meinander, E. Peuhu, R. Niemi, J.E. Eriksson, C. Sahlgren, and M. Linden. 2009. *ACS Nano* 3(1):197-206.
97. Wang, L.-S. and L.-C. Wu, S.-Y. Lu, L.-L. Chang, I.-T. Teng, C.-M Yang, and J.-A.A. Ho. 2010. *ACS Nano* 4(8):4371-4379.
98. Guo, R. and L.-L. Li, W.-H. Zhao, Y.-X. Chen, X.-Z. Wang, C.J. Fang, W. Feng, T.-L. Zhang, X. Ma, M. Lu, S.-Q. Peng, and C.-H. Yan. 2012. *Nanoscale* 4(11):3577-3583.
99. Sudimack, J. and R.J. Lee. 2000. *Adv. Drug Deliv. Rev.* 41(2):147-162.
100. Brevet, D. and M. Gary-Bobo, L. Raehm, S. Richeter, O. Hocine, K. Amro, B. Loock, P. Couleaud, C. Frochot, A. Morere, P. Maillard, M. Garcia, and J.-O. Durand. 2009. *Chem. Comm.* 12:1475-1477.
101. Ferris, D.P. and J. Lu, C. Gothard, R. Yanes, C.R. Thomas, J.-C. Olsen, J.F. Stoddart, F. Tamanoi, and J.I. Zink. 2011. *Small*. 7(13):1816-1826.
102. Fang, I.-J. and I.I. Slowing, K.C.-W. Wu, V.S.-Y. Lin, and B.G. Trewyn. 2012. *Chem-Eur. J.* 18(25):7787-7792.
103. Tsai, C.-P. and C.-Y. Chen, Y. Hung, F.-H. Chang, C.-Y. Mou. 2009. *J. Mater. Chem.* 19(32):5737-5743.
104. Pan, L. and Q. He, J. Liu, Y. Chen, M. Ma, L. Zhang, and J. Shi. 2012. *J. Am. Chem. Soc.* 134(13):5722-5725.
105. Lu, J. and Z. Li, J.I. Zink, and F. Tamanoi. 2012. *Nanomedicine* 8(2):212-220.
106. Li, L. and F.-Q. Tang, H.-Y. Liu, T.-L. Liu, N.-J. Hao, D. Chen, X. Teng, and J.-Q. He. 2010. *ACS Nano* 4(11):6874-6882.
107. Torney, F. and B.G. Trewyn, V.S.-Y. Lin, and K. Wang. 2007. *Nature Nanotechnol.* 2(5):295-300.
108. Martin-Ortigosa, S. and J.S. Valenstein, V.S.-Y. Lin, B.G. Trewyn and K. Wang. 2012. *Adv. Func. Mater.* (in press).

CHAPTER 3. INTERACTION OF MESOPOROUS SILICA NANOPARTICLES WITH HUMAN RED BLOOD CELL MEMBRANES: SIZE AND SURFACE EFFECTS

A paper published in ***ACS Nano***, **2011**, *5*, 1366-1375

Yannan Zhao, **Xiaoxing Sun**, Guannan Zhang, Brian G. Trewyn, Igor I. Slowing, and Victor S.-Y. Lin

ABSTRACT

The interactions of mesoporous silica nanoparticles (MSNs) of different particle sizes and surface properties with human red blood cell (RBC) membranes were investigated by membrane filtration, flow cytometry and various microscopic techniques. Small MCM-41-type MSNs (~100 nm) were found to adsorb to the surface of RBCs without disturbing the membrane or morphology. In contrast, adsorption of large SBA-15-type MSNs (~600 nm) to RBCs induced a strong local membrane deformation leading to spiculation of RBCs, internalization of the particles, and eventual hemolysis. In addition, the relationship between the degree of MSN surface functionalization and the degree of its interaction with RBC, as well as the effect of RBC-MSN interaction on cellular deformability were investigated. The results presented here provide a better understanding of the mechanisms of RBC-MSN interaction and the hemolytic activity of MSNs, and will assist in the rational design of hemocompatible MSNs for intravenous drug delivery and *in vitro* imaging.

1. Introduction

Recent advancements in particle size and morphology control of mesoporous materials have led to the creation of nano- and submicron-sized mesoporous silica nanoparticles (MSNs).[1-5] The MSN materials with well-ordered cylindrical pore structures such as MCM-41 and SBA-15, have attracted special interest in the biomedical field.[1] The large surface areas and pore volumes of these materials allow the efficient adsorption of a wide range of molecules, including small drugs,[6-10] therapeutic proteins,[11-13] antibiotics,[14, 15] and antibodies.[16] Therefore, these materials have been proposed for use as potential vehicles for biomedical imaging, real-time diagnosis, and controlled delivery of multiple therapeutic agents.[6-8, 10, 17-25]

Despite the considerable interest in the biomedical applications of MSNs, relatively few studies have been published on the biocompatibility of the two most common types of MSNs (MCM-41 and SBA-15).[26-29] Asefa and co-workers reported that the cellular bioenergetics (cellular respiration and ATP levels) were inhibited remarkably by large SBA-15 nanoparticles, but the inhibition was greatly reduced by smaller MCM-41 type nanoparticles.[26] These differences in the disruption of cellular bioenergetics are believed to be caused by the different surface areas, number of surface silanol groups, and/or particle sizes of both types of material. A recent study by Kohane and collaborators on the systemic effects of MCM-41 (particle size ~ 150 nm) and SBA-15 (particle size ~ 800 nm) MSNs in live animals revealed interesting findings regarding their biocompatibility.[27] While large doses of mesoporous silicas administered subcutaneously to mice appear to be relatively harmless, the same doses given intravenously or intraperitoneally were lethal.[27] A possible reason for the severe systemic toxicity of MSNs when injected intravenously could be the interactions of the nanoparticles with blood cells.

Our initial studies on the biocompatibility of MCM-41 type MSNs with red blood cells (RBCs), the dominant (99%) cell type in blood, suggested that this material was innocuous in comparison to the highly hemolytic amorphous silica.[30] These results were later confirmed by Lin and Haynes, who demonstrated that the hemocompatibility of MSNs also depended on the size of the nanoparticles.[31] These findings were mainly based on hemolysis assays performed by UV-Vis spectroscopy. The lack of hemolysis, however, does not necessarily warrant the absence of interactions between the particles and the RBCs, which could lead to more subtle side effects. Such side effects could eventually be the ones responsible for the enhanced systemic toxicity observed upon intravenous injection of these materials.[27] Therefore, an in depth study of other possible biological side effects of these materials must be performed if they are intended to be applied as vehicles for drug delivery.

In general, our knowledge of the biocompatibility, bioretention, and biodistribution of MSNs does not match with the rapid pace of research on their syntheses in numerous forms and structures. To date, efforts have focused predominantly on exploiting multifunctional nanoparticles as intravascular drug carriers with different particle sizes ranging from a few tens of nanometers[4,24,32] up to hundreds of nanometers,[3,5] various pore diameters ranging from 2 to 10 nm[5,11,33] and assorted surface functionalities from small

organic groups (*e.g.*, amino,[34,35] carboxyl,[35] thiol,[35] phosphate,[19] *etc*) to large molecules (*e.g.*, dendrimers,[36] polyethyleneimine (PEI),[25,37] poly(ethylene glycol) (PEG),[38] phospholipids,39 *etc*). Unfortunately, these endeavors are limited by a poor understanding of particle interactions with cells in circulation.

Herein, we report our investigations on the interactions of the two most common types of MSNs (MCM-41 and SBA-15) with RBC membranes using fluorescence and electron microscopies and cell biology techniques. In addition to studying the effects of particle size and surface area on the hemolytic behavior of MSNs, we explored the effects that the chemical nature and degree of surface functionalization of the particles has on their interactions with RBCs. Understanding these effects will not only offer a guide for the rational design of biocompatible particles, but will also provide an insight into how to control the circulation properties of MSNs in the bloodstream. In fact, a prolonged circulation of polymeric nanoparticles has been recently demonstrated by means of their non-covalent attachment to the RBC membrane.[40] Attachment to the RBC membrane, however, may affect one of its most important properties, namely its deformability (*i.e.* the ability of an erythrocyte to deform so it can flow through microcirculation). To the best of our knowledge, this problem has not yet been addressed for any drug delivery system. In this work, we examined the effect of RBC-MSN interactions on membrane deformability by the Nucleopore filtration technique,[41] and established how size and surface properties can alter this important property. Overall, we propose three fundamental criteria to assess the hemocompatibility of nanoparticles: (1) hemolytic potential, (2) propensity to induce RBC membrane deformation or morphological alteration, and (3) tendency to impair RBC deformability. The evaluation of these conditions will enable a more adequate estimation of the hemocompatibility of many types of nanomaterials. This study suggests a minimal set of criteria that must be met before performing *in vitro* studies involving the intravascular administration of nanoparticles.

2. Results and Discussion

2.1. Size- and surface-dependent MSN interaction with RBC membranes

While particle size effect of MCM-41 type MSNs has already been established with larger particles producing lower hemolysis on RBC,[31] the question remains whether the typically larger SBA-15 type MSNs as hemocompatible. A more critical issue is that the

mechanism of how MSNs of different sizes and surface areas correlate and contribute to their hemocompatibility is unclear, although several biological rationales have been suggested.[30,31] To address these questions, we prepared two types of MSNs: MCM-41 and SBA-15, as described in the Methods section. Scanning electron microscopy (SEM) and transmission electron microscopy (TEM) images showed particle sizes of 100 to 200 nm for the MCM-41-type MSNs (referred to as *s*-MSN, Figure 1a,d) and ~600 nm by ~300 nm for the SBA-15-type MSNs (referred as *l*-MSN, Figure 1b,e). The hydrodynamic particle size distributions of the materials suspended in phosphate-buffered saline (PBS) (100 μg mL^{-1}) were determined by dynamic light scattering (DLS), giving average sizes of 122 nm for *s*-MSN and 531 nm for *l*-MSN (Figure 1c). XRD patterns showed that both *s*-MSNs and *l*-MSNs exhibit 2D hexagonal pore arrangements (Figure 1f).

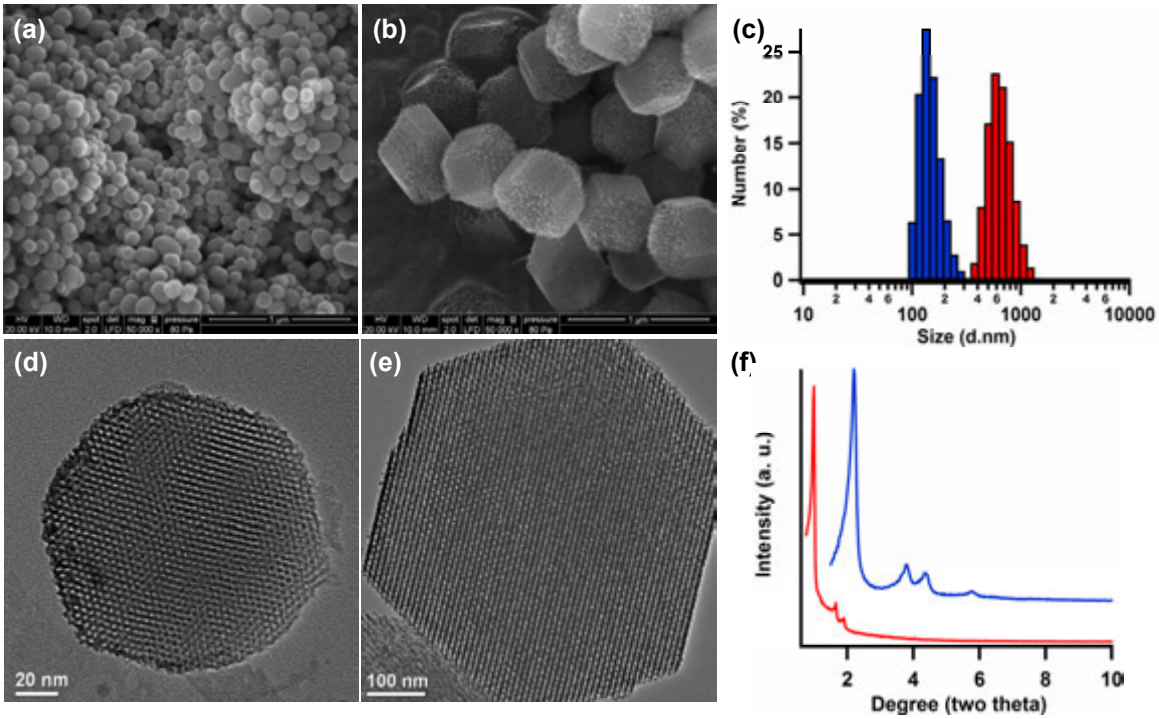

Figure 1. Scanning electron (top) and transmission electron (bottom) images of (a, d) *s*-MSN and (b, e) *l*-MSN. (c) Hydrodynamic size distributions of *s*-MSN (blue) and *l*-MSN (red) suspended in PBS (100 μg mL^{-1}) measured by dynamic light scattering. (f) X-ray diffraction patterns of *s*-MSN (blue) and *l*-MSN (red).

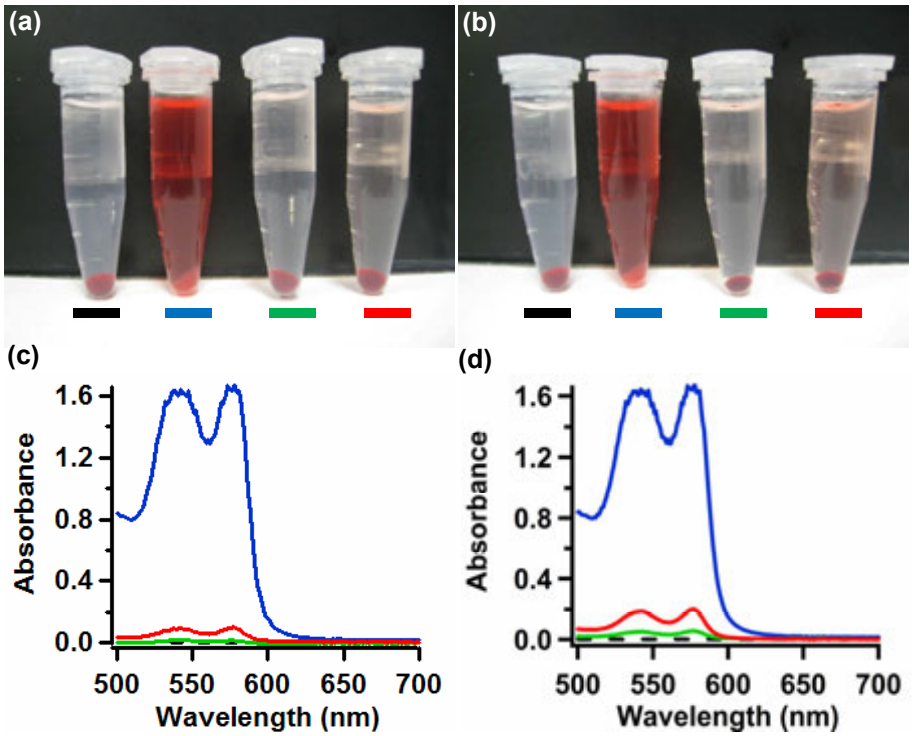

Figure 2. Hemolysis assay for *s*-MSN (green lines) and *l*-MSN (red lines), using water as a positive control (blue lines) and PBS as a negative control (dashed black lines). The materials were suspended at 50 (a, c) and 100 μg mL^{-1} (b, d). The mixtures were centrifuged to detect the presence of hemoglobin in the supernatant visually (a, b) and by absorption at 541 nm (c, d).

The hemolysis assay was used to evaluate the hemolytic behaviors of *s*-MSN and *l*-MSN on human RBCs. Human RBCs were first isolated by centrifugation and purified by five successive washes with sterile isotonic PBS, then diluted to 5% hematocrit with PBS before incubating with MSN suspensions of various concentrations. Controls were prepared in the same manner as the above RBC samples except adding water (positive control) and PBS (negative control) instead of the MSN suspensions. After a two-hour incubation at room temperature, the samples were spun down for the detection of hemoglobin released from hemolyzed RBCs. Surprisingly, contrary to the recently reported trend regarding size,[31] MSNs with larger particle size exhibited a higher hemolytic activity than the small particles (Figure 2). The hemolytic activity of *l*-MSNs was first observed at 50 μg mL^{-1} with 5% hemolysis detected, while a good hemocompatibility (< 2% hemolysis) of *s*-MSN was confirmed at concentrations as high as 100 μg mL^{-1}. While a larger particle size may be preferable for hemocompatible MSNs

below 225 nm,[31] increasing particle size of MSNs beyond this range will not necessarily improve the hemocompatibility as one might intuitively expect. In addition to particle size, other factors such as the surface area are also expected to affect the hemolytic potential of MSNs.

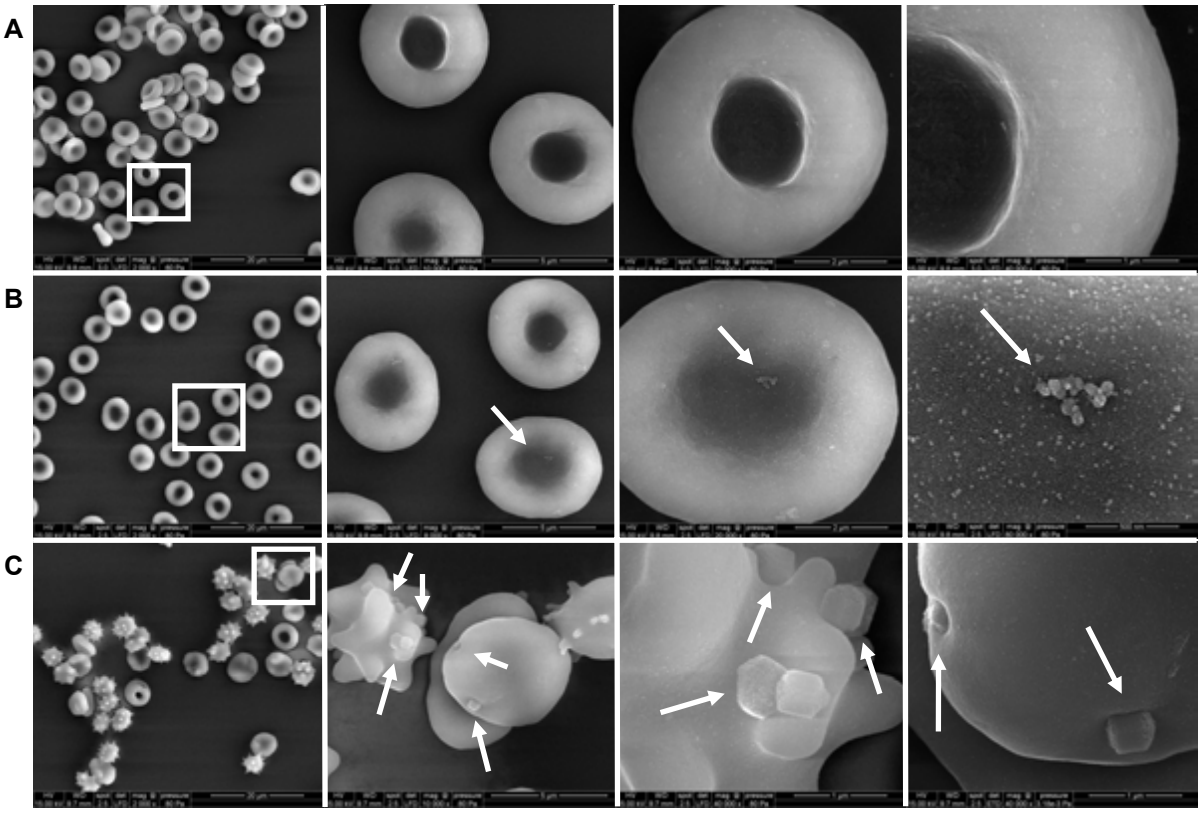

Figure 3. Scanning electron images of RBCs (5% hematocrit) incubated for 2 h at room temperature with (A) PBS as control, (B) 100 μg mL^{-1} of *s*-MSN and (C) 100 μg mL^{-1} of *l*-MSN. Images increase in magnification from left to right with features highlighted with white squares or arrows. The nanoparticles attached on cell surface are distinguished by the particle shape and surface textural difference between the particles and RBCs. (Additional high magnification images are shown in Figure S2.)

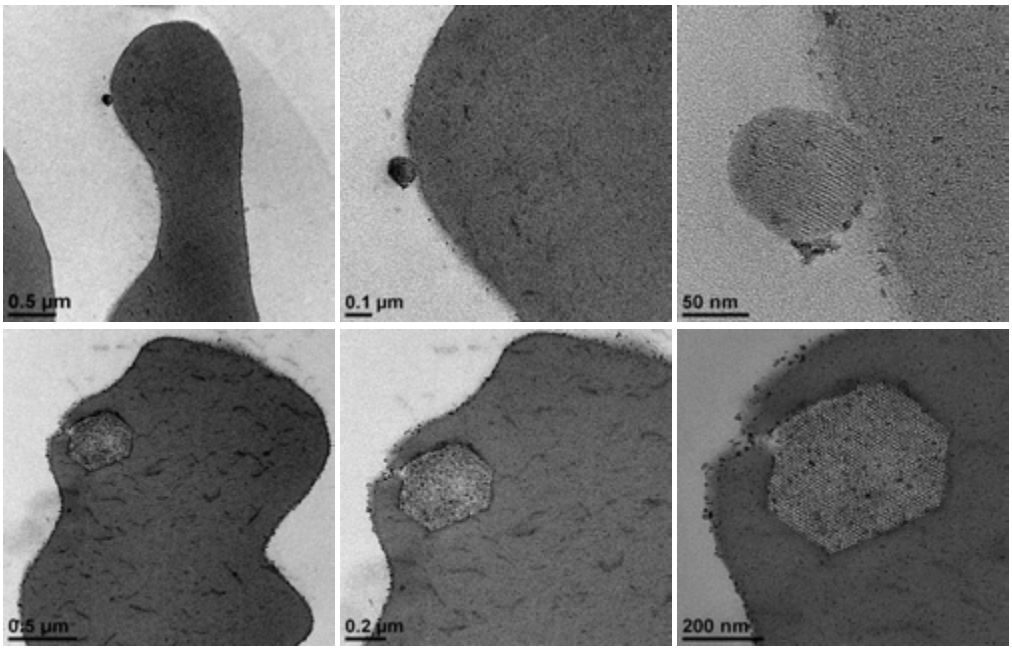

Figure 4. Transmission electron images of RBCs (5% hematocrit) incubated for 2 h at room temperature with 100 μg mL^{-1} *s*-MSN (top) and *l*-MSN (bottom). Images increase in magnification from left to right. The presence of MSNs is confirmed by the visible pores in the higher magnification micrographs.

To elucidate the mechanism of the observed difference in hemolysis and investigate the underlying particle size and surface effects, the interaction of MSNs with RBCs were visualized by SEM (Figure 3) and TEM (Figure 4). A small proportion of *s*-MSNs were found to adsorb to the surface of RBC. The cell membrane did not show any alteration upon particle binding and RBCs maintained normal biconcave shape compared to control RBCs (Figure 3B and Figure 4 top). In contrast, a large proportion of *l*-MSNs attached to RBC membranes and induced a strong local membrane deformation, which frequently resulted in particle encapsulation by RBCs (Figure 3C and Figure 4 bottom). The membrane wrapping around *l*-MSNs led to an echinocytic (spiculated) shape transformation of RBCs and a reduction in the ratio of surface area to volume.[42] This inability to maintain their normal surface area and control their cell volume can ultimately lead to the destruction of these cells,[42] which explains the observed high hemolytic activity of *l*-MSNs.

Two main processes are involved in the interaction of MSN with the membrane of RBC: (1) binding of the silanol-rich surface of MSNs with the phosphatidyl choline-rich RBC membrane,[30] and (2) bending of the RBC membrane to adapt to the rigid surface of

MSNs (Scheme 1).[43-47] The occurrence of the interaction depends on whether the amount of energy released from the binding of the MSNs with the RBC membrane (E_i) is able to overcome the amount of free energy required to bend the membrane and adapt to the surface of MSNs (E_b). The former energy is associated with the external surface area (*i.e.*, accessible silanols) of MSN,[30] while the latter is proportional to the curvature or inversely proportional to the square of the radius (r) of the particle.[43,44,47] The external surface areas of *s*-MSNs and *l*-MSNs, calculated from the t-plots of their N_2 adsorption isotherms,[48] were 81.6 and 155.4 m^2 g^{-1}, respectively. The relatively large external surface area of *l*-MSN (40% of total surface area) in comparison to that of *s*-MSN (8% of total surface area) implies that *l*-MSN can have a larger binding energy (E_i) available for pulling the membrane to the particle surface. In addition, since surface curvature decreases with particle size, the bending energy required to wrap the large particles (E_b) is lower than the one needed to wrap the smaller particles.[43] This combination makes membrane wrapping and engulfment of *l*-MSN thermodynamically favorable. On the contrary, in order for the RBC membranes to wrap around smaller *s*-MSNs, they would have to attain a larger curvature (steeper angles over smaller areas) than they need for wrapping around the larger particles.[43] This would require investing a much higher E_b compared to the small amount of E_i, which thermodynamically prevents the membrane deformation or engulfment of *s*-MSN by RBC, and explains the lower hemolytic activity of *s*-MSNs. Similar explanations on the effect of particle size on membrane wrapping have been reported elsewhere.[43,44] Hence, the interaction of MSNs with RBC membranes and the hemolytic activity depends on not only particle size but on their external surface area as well.

2.2. Size- and surface-dependent engulfment of MSNs by RBCs

Though the *in vitro* endocytosis of MSN has been systematically investigated with various mammalian cell lines,[4,11,17,34,36,49-52] little is known about the uptake of nanoparticles by RBCs. This is partly because the interactions between RBC and MSN are still poorly understood. Before investigating the internalization of MSNs by RBC, it is necessary to establish the concentration at which the plasma membrane maintains its integrity and RBCs retain normal biconcave shape. To do so, the RBCs were incubated with *l*-MSNs at different concentrations; and the hemolytic effects as well as the resulting

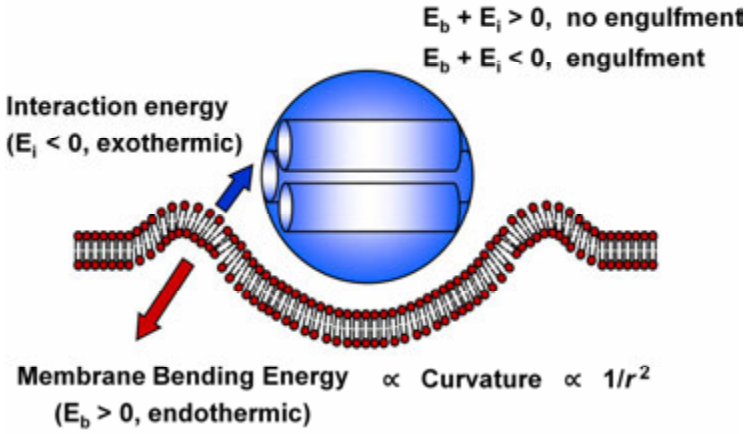

Scheme 1. A schematic illustration of the size- and surface-dependent interaction of MSN and RBC membrane. MSN with radius *r* can be wrapped around or engulfed by RBC if the energy (E_i) released from RBC-MSN interaction is greater than the energy (E_b) required for membrane bending.

cell morphologies were examined by UV-Vis spectroscopy (Figure S3 in Supporting Information) and SEM (Figure S4). The hemolysis percentage of RBCs increased from 1% to 11% as the concentration of *l*-MSN raised from 20 to 100 μg mL^{-1}, and growing proportions of spiculated RBCs were observed with increasing concentrations of *l*-MSN. As shown in Figure S4, almost 90% of RBCs exhibited spiculated shape with 100 μg mL^{-1} of *l*-MSN. The proportion of spiculated RBCs decreased to 50% when 50 μg mL^{-1} of *l*-MSN was used. Interestingly, only minor shape modifications (less than 10% spiculated cells) in RBCs were observed after incubation with 20 μg mL^{-1} of *l*-MSN, even if many particles were adsorbed to the membranes or underwent internalization (Figure S4 left). Therefore, the cellular uptake process was examined at a concentration of 20 μg mL^{-1} of *l*-MSN (Figure 5). It should be noted that the images in Figure 5 correspond to different cells at different stages of nanoparticle encapsulation. A plausible interpretation of our observations is as follows. The particle interacts with an initially flat cell membrane. Driven by a local reduction in free energy (Scheme 1), the phospholipids in the immediate neighborhood of the site of contact are drawn to the surface of the particle, leading to membrane wrapping and eventual encapsulation. Such internalization is different from phagocytosis or endocytosis, since it appears to be driven by the balance of two opposing forces rather than by an active uptake of nutrients by the cell. It should be stressed that even if almost no hemolysis or spiculation is observed at

this concentration we cannot yet exclude the potential side effects of the internalization of *l*-MSN into RBC. Nevertheless, this preliminary study on MSN engulfment by RBC is an important step toward establishing the plausibility of using MSNs as tools for the treatment of RBC related diseases or intravascular drug delivery. We are currently conducting more studies to understand and control the internalization of MSNs and the delivery of therapeutic agents into RBCs to be published in subsequent manuscripts.

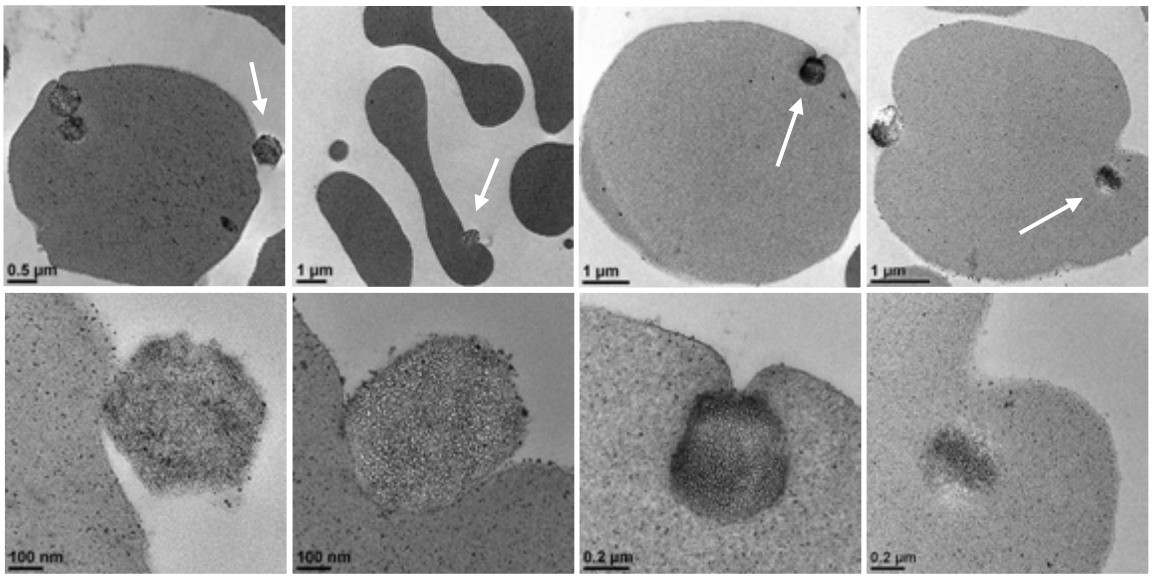

Figure 5. Cellular uptake process (left to right) examined by transmission electron microscopy of RBCs (5% hematocrit) incubated with 20 μg mL^{-1} *l*-MSN. Images increase in magnification from top to bottom, with features highlighted in white arrows. These images (left to right) correspond to different cells at different stages of nanoparticle encapsulation.

2.3. Surface functionality effects on RBC-MSN interaction

The results from the size- and surface-dependent interactions of MSNs with RBCs have demonstrated a superior hemocompatibility of *s*-MSNs over *l*-MSNs. This does not imply, however, that *s*-MSNs lack any interaction with the membranes of RBCs. While the interactions of MSNs with the membranes of RBCs is known to be dependent on the presence of silanol groups on the surface of the particles,[30,31] there is no quantitative information on the magnitude of this association. Given the interest of utilizing *s*-MSNs for intravenous drug delivery it is necessary to be able to measure and control the degree of the abovementioned interactions and, thus, controlling the circulation of the particles in the bloodstream.[40,53]

To study these interactions, *s*-MSNs were first labeled with fluorescein isothiocyanate (FITC), which enabled their tracking by flow cytometry and confocal fluorescence microscopy. FITC-*s*-MSNs were then functionalized with different amounts of aminopropyl (AP), polyethylene glycol (PEG) and carboxyl (CA) groups, as described in the Methods section. These functionalized materials are referred as AP_x-FITC-*s*-MSN, PEG_x-FITC-*s*-MSN and CA_x-FITC-*s*-MSN, respectively; where the subscript *x* corresponds to the number of mmol introduced per gram of material. The amount of functional groups (AP, PEG and CA) grafted on MSNs was quantified by TGA shown in Figure S5 bottom and summarized in Table S1. The quantification of nanoparticle attachment to the membrane of RBCs was performed by flow cytometry. Diluted suspensions of RBCs (5×10^6 cells mL^{-1}) were mixed with equal volumes of nanoparticle suspensions to reach a final concentration of 10 μg mL^{-1} of MSNs and incubated at room temperature for 2 h before flow cytometry analysis. As shown in Figure 6, the functionalized nanoparticles exhibited lower affinity to RBC than FITC-*s*-MSNs, furthermore, the affinity decreased with increasing degree of functionality. This trend was observed for each functionalized material, independent of the surface charge. In particular, AP and PEG groups (~25% of RBC bound with $AP_{1.5}$-FITC-*s*-MSN and ~20% with PEG_1-FITC-*s*-MSN) showed a significantly better ability to reduce the MSN binding with RBC than CA groups (~65% of RBC bound with $CA_{1.5}$-FITC-*s*-MSN). The inhibitory effect of PEG on the adsorption of MSN to RBC was not surprising, since PEGylation of nanoparticles is generally used to block nonspecific binding of nanoparticles to proteins.[54] On the contrary, the reduction of MSN binding to RBC due to aminopropyl group functionalization, was completely unexpected, since amines are well known to facilitate adsorption of several biomolecules to the surface of nanoparticles and facilitate many nanoparticle-cell interactions.[34,55] The reduced binding of AP-FITC-*s*-MSN to RBC could be explained by the electrostatic interaction between amino groups on the surface of MSNs and surface silanols,[56] which diminishes the accessibility of silanol groups to the cell membrane.

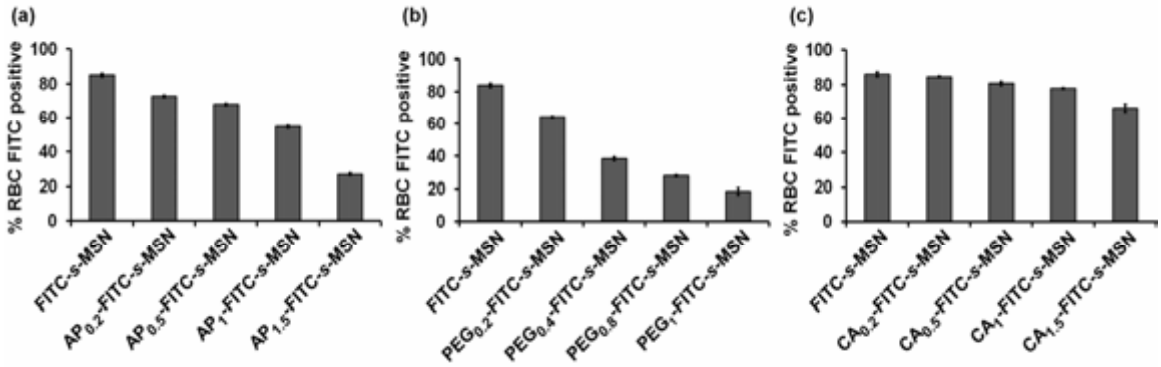

Figure 6. Flow cytometry measurement of RBCs (5×10^6 cells mL^{-1}) incubated with 10 μg mL^{-1} of (a) AP_x-FITC-*s*-MSN, (b) PEG_x-FITC-*s*-MSN and (c) CA_x-FITC-*s*-MSN.

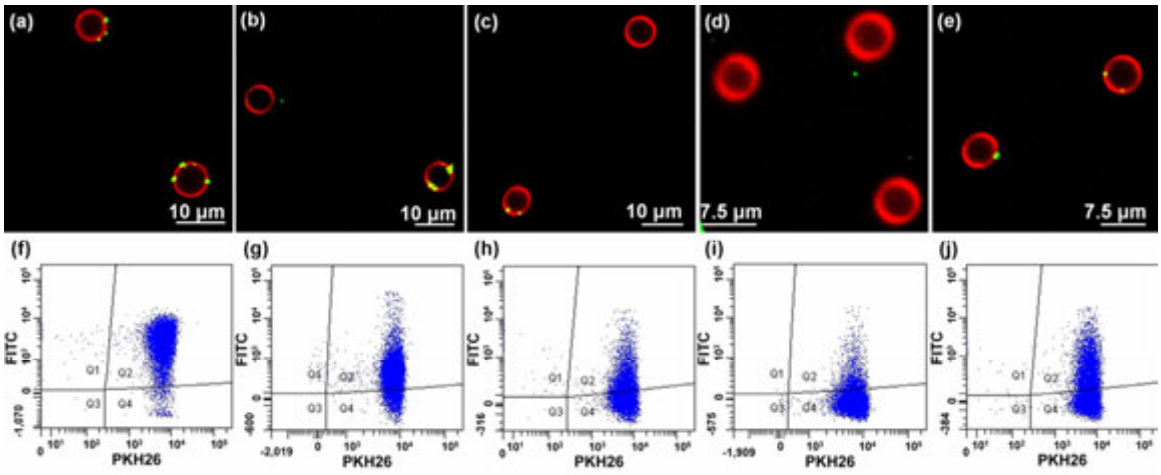

Figure 7. Confocal fluorescence micrographs (top) and dot plots from the flow cytometry analyses (bottom) of PKH26 labeled RBCs (5×10^6 cells mL^{-1}) incubated with 10 μg mL^{-1} of (a, f) FITC-*l*-MSN, (b, g) FITC-*s*-MSN, (c, h) $AP_{1.5}$-FITC-*s*-MSN, (d, i) PEG_1-FITC-*s*-MSN and (e, j) $CA_{1.5}$-FITC-*s*-MSN. The axes correspond to the intensity of red fluorescence due to PKH26 labeling (horizontal axis) and green fluorescence due to the attachment of FITC-MSNs onto PKH26-RBCs (vertical axis). The plot was gated to show PKH26 labeled RBCs in area Q4 and FITC-fluorescent PKH26-RBCs in area Q2. Individual channels for the merged confocal images and enlarged dot plots with PKH26-RBC control are shown in Figure S7 and Figure S8, respectively.

The results obtained by flow cytometry were further confirmed by examination of the mixtures of the derivatized MSNs with RBCs under confocal fluorescence microscopy. For this purpose, RBCs were first labeled with PKH26 red fluorescent dye (Sigma) and incubated with FITC labeled particles at the same conditions as in the flow cytometry

experiment. FITC-*l*-MSNs, FITC-*s*-MSNs and $CA_{1.5}$-FITC-*s*-MSNs (Figure 7a,b,e) were easily observed associated to PKH26-labeled RBCs. Conversely, only a small proportion of $AP_{1.5}$-FITC-*s*-MSNs (Figure 7c) and PEG_1-FITC-*s*-MSNs (Figure 7d) were found co-localized with PKH26-RBCs, while most of the particles were observed in the extracellular space. A series of movies showing each one of these combinations of MSNs and RBCs were prepared from micrographs taken at different z-positions by changing the focal plane every 0.5 μm, these movies can be found in the Supporting Information. The different affinities of each MSN for the RBCs were also confirmed by the different shifts of the green fluorescence intensities in the 2D dot plots from flow cytometry (Figure 7, bottom).

2.4. Effect of RBC-MSN interaction on RBC deformability

The attachment of nanoparticles to the surface of red blood cells has been suggested for extending the circulation time and sustained release of therapeutic agents.[40,53] Such attachment, however, could have an impact on the properties of the membrane affecting the normal function of RBCs. Surprisingly, this potential problem has not been addressed for any nanoparticle-based drug carrier, to the best of our knowledge. One of the key properties of RBCs (6-8 μm in diameter) is their ability to undergo deformation to traverse the capillaries of the microvascular system (2-3 μm in diameter). This remarkable deformability of RBCs is critical for effective blood flow, and depends strongly on the flexibility of the cell membrane. This is the reason why it is important to assess the effects of MSN attachment on the deformability of RBCs.

To study the deformability of RBCs, we used a literature reported method consisting of filtering the cells through polycarbonate membranes with straight channels of 3 μm pore diameter (Nucleopore).[41] This technique is generally accepted as a relative indication of RBC deformability.[41,57-59] We measured the filterability of fresh human RBCs (5% hematocrit) previously incubated with varying concentrations (10, 20, 50 μg mL^{-1}) of MSN under a constant negative pressure (-20 cm H_2O). The time it took each RBC suspension to flow through the membrane was recorded and the deformability index (DI) was expressed as the volume (mL) of red blood cells filtered per minute. As shown in Figure 8a, the deformability of RBC decreased with increasing concentrations of all MSN materials. The RBC deformability was severely impaired by *l*-MSN at concentrations as low as 10 μg mL^{-1}. This result is not surprising given the strong

affinity and shape altering effects already described for *l*-MSN. As expected, the incorporation of AP and PEG groups to the surface of *s*-MSN preserved the elasticity of

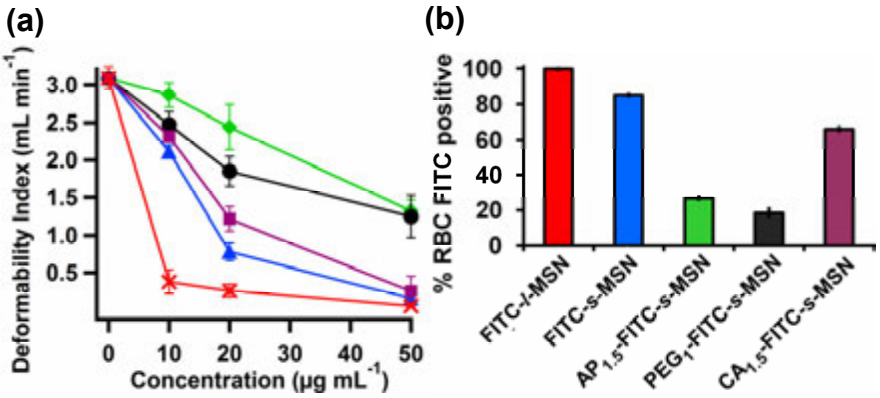

Figure 8. (a) Deformability Index (DI) of RBCs incubated with *s*-MSN (blue), $AP_{1.5}$-*s*-MSN (green), PEG_1-*s*-MSN (black), $CA_{1.5}$-*s*-MSN (purple) and *l*-MSN (red). (b) Flow cytometry analyses of RBCs incubated with FITC-*l*-MSN (red), FITC-*s*-MSN (blue), $AP_{1.5}$-FITC-*s*-MSN (green), PEG_1-FITC-*s*-MSN (black), and $CA_{1.5}$-FITC-*s*-MSN (purple).

RBCs better than the non-functionalized *s*-MSN and the CA-*s*-MSN, especially at the higher concentrations (> 20 μg mL^{-1}). These results correlate well with the observed effects on the degree of RBC-MSN interactions (Figure 8b). These observations suggest that the attachment of MSNs to the surface of RBCs restrict the flexibility of the membrane and lead to impairment in the deformability of RBCs. Conversely, the attachment of functional groups to the surface of MSNs reduces the affinity of the particles to the membrane of RBC and allows the cells to preserve their deformability.

3. Conclusion

In this study, we investigated the interactions between MSNs of different particle sizes and surface properties and RBC membranes by using fluorescence and electron microscopies and cell biology techniques. We compared the size- and surface-dependent hemocompatibility of two types of MSN materials (MCM-41 and SBA-15) and showed, for the first time, how MSNs are engulfed by RBCs. This size- and surface-dependent process is the resultant of two opposing forces, namely: the attractive interaction between MSNs and RBCs, and the bending of the cell membrane.

These results suggest that only small MCM-41 type MSN materials (100-200 nm) may be considered as potentially safe candidates for intravascular drug delivery. It must be noted that although RBCs are the dominant cells in blood, the interactions of these nanoparticles with other blood cells and components[60,61] should be also evaluated to ensure the safe use of these materials for biomedical applications. In addition, we demonstrated that the biocompatibility of these MSN materials with RBCs strongly depends on their surface derivatization to minimize their interaction with red blood cells. Blocking the surface silanols of the particles with organic groups reduces their interactions with the membranes of RBCs. Minimizing these interactions has a dramatic effect on preserving the deformability of RBCs, which is necessary to ensure effective blood circulation. These findings suggest that it is possible to gain control over the interactions of MSNs with RBC membranes in order to regulate their circulation half lives for various therapeutic purposes, while minimizing their toxicity by carefully choosing and tuning their surface functionalities. As new MSN-based drug delivery systems burgeon from many international research groups, our results will provide a practical guide to size and surface considerations when designing MSN-based drug carriers for delivery, diagnostic, and therapeutic applications.

4. Methods

Synthesis of Mesoporous Silica Nanoparticles. *s*-MSN was prepared by our previously reported method.[33] In brief, N-cetyltrimethylammonium bromide (CTAB, 1.00 g, 2.74 mmol) was dissolved in 480 mL nanopure water, followed by the addition of 3.5 mL sodium hydroxide aqueous solution (2.0 M), and the mixture was heated to 80 °C. Tetraethoxysilane (TEOS, 5.0 mL, 22.4 mmol) was added dropwise to the surfactant solution under vigorous stirring. The reaction mixture was stirred at 80 °C for another 2 h. The resulting white solid was filtered, washed thoroughly with water and methanol, and dried under high vacuum at 80 °C overnight. The fluorescent labeled MSN (FITC-*s*-MSN) was synthesized by reacting fluorescein isothiocyanate (FITC, 15 mg, 38.5 μmol) with (3-aminopropyl)trimethoxysilane (APTMS, 10 μL, 57.3 μmol) for 2 hours in dimethyl sulfoxide (DMSO), and adding the resulting product following the addition of TEOS in the above synthesis. The unlabeled FITC was removed by soxhlet extraction with methanol. The amount of FITC labeled on FITC-*s*-MSN was quantified to be 20-30 μmol g^{-1} by TGA. The functionalization of *s*-MSN and FITC-*s*-MSN with

aminopropyl (AP), polyethylene glycol (PEG) and carboxylate (CA) groups was performed by refluxing a suspension of the as-made material (200 mg of *s*-MSN or FITC-*s*-MSN) with APTMS, 2-[methoxy(polyethylenoxy)-propyl]trimethoxysilane (PEG-silane) and 3-(triethoxysilyl)propylsuccinic anhydride of various amount (*x* mmol) in anhydrous toluene (50 mL) for 20 h, followed by filtration and washing with toluene and methanol, and dried under high vacuum overnight. The succinic anhydride groups were hydrolyzed by boiling the materials in water for 6 hours and measured by FTIR. The CTAB surfactant was removed by refluxing the materials in 0.37% HCl methanol, followed by filtration and washing with abundant methanol and dried under high vacuum. The amount of functional groups (AP, PEG and CA) grafted on MSNs was quantified by TGA shown in Figure S5 bottom and summarized in Table S1.

l-MSN was prepared by a modified literature procedure.[5] Pluronic P104 (courtesy of BASF, 7.0 g) was dissolved in a mixture of water (164 g) and HCl (109 g, 4M) and stirred at 55 °C for 1 hour. Tetramethyl orthosilicate (10.64 g) was quickly added into the solution at 55 °C. After continuous stirring for 24 hours, the reaction mixture was moved to a teflon-lined, high-pressure autoclave for further hydrothermal treatment at 150 °C for 24 h. The product was isolated by filtration, washed with copious water and methanol, and dried at 80 °C in air. The Pluronic P104 surfactant was removed by calcination at 550 °C for 6 hours. The *l*-MSN was fluorescently labeled (FITC-*l*-MSN) by reacting FITC (15 mg, 38.5 μmol) with APTMS (10 μL, 57.3 μmol) for 2 hours in dimethyl sulfoxide (DMSO), and adding the resulting product to a suspension of *l*-MSN (1 g) in anhydrous toluene (100 mL) for 20 h, followed by filtration and washing with toluene and methanol. The unlabeled FITC was removed by soxhlet extraction with methanol as the solvent. The amount of FITC labeled on FITC-*l*-MSN was quantified to be around 30 μmol g^{-1}.

The products were characterized by X-ray diffraction in a Rigaku Ultima IV diffractometer, nitrogen sorption analysis in a Micromeritics Tristar 3000 surface area and porosity analyzer using Brunauer-Emmett-Teller (BET) equation to calculate apparent surface area and pore volume and the Barret-Joyner-Halenda (BJH) method to calculate pore size distribution, thermogravimetric analysis (TGA) in a TGA 2950 thermogravimetric analyzer with a temperature ramp of 5 °C/min in air, dynamic light scattering size analyses of particle suspensions in a Malvern Nano HT Zetasizer, scanning electron microscopy (SEM) of samples coated with gold in a FEI Quanta 250 FEG

microscope, and transmission electron microscopy (TEM) of samples supported on copper grids in a Tecnai G2 F20 microscope operated at 200 kV. FTIR spectroscopy was performed using a Nicolet Nexus 470 (Madison, EI), equipped with a cooled CT/A detector and an Ever-Glo source.

Isolation and labeling of red blood cells (RBCs). Ethylenediamine tetraacetic acid (EDTA)-stabilized human blood samples were freshly collected in the Occupational Medicine Office of Iowa State University and Ames Laboratory. Whole blood was centrifuged at 1600 rpm for 5 min and the plasma, buffy coat, and top layer of cells were decanted. The remaining packed RBCs were washed five times with sterile isotonic PBS. For labeling with PKH26 (Red fluorescent cell linker kit, Sigma, USA), 100 μL of packed RBCs were resuspended in 1 ml diluent C™ and mixed with 1 ml diluent C™ containing 4 μM PKH26. Cells were incubated for 5 min at room temperature in the dark. The reaction was stopped by adding 1 mL plasma (heat inactivated for 1 hour at 65°C beforehand) for 1 minute and centrifuged at 1600 rpm for 5 min. The stained RBCs were washed five times with PBS to remove free pKH26 dye.

Hemolysis assay. After cell washing, 200 μL of packed RBC was diluted to 4 mL with PBS (5% hematocrit). The diluted RBC suspension (0.2 mL) was then mixed with *s*-MSN and *l*-MSN suspensions in PBS (0.8 mL) at various concentrations. PBS and water (0.8 mL) were used instead of MSN suspensions as negative and positive control, respectively. The mixture was gently vortexed and incubated at room temperature for 2 h, followed by centrifuge (1600 rpm, 5 min) and the absorbance of the supernatant at 541 nm was measured by UV-Visible spectrometry. The percent hemolysis of RBCs was calculated using the following formula: percent hemolysis = ((sample absorbance - negative control absorbance)/(positive control absorbance - negative control absorbance)) × 100.

Scanning electron microscopy (SEM). The diluted RBC suspension (5% hematocrit, 0.2 mL) was mixed with *s*-MSN and *l*-MSN suspensions in PBS (0.8 mL) at various concentrations, and incubated at room temperature for 2 h. The samples were then fixed by adding a 1% glutaraldehyde solution dropwise over 5 min and further incubated at 37 °C for 1.5 h, followed by post-fixation with 1% osmium tetroxide in PBS for 1.5 h. Cells were dehydrated in increasing concentrations of ethanol (50%, 60% 70%, 80%, 90%, and 100%) for 15 min each. The cell suspensions were dropped onto

glass coverslips, dried, and coated with Au before viewing under a FEI Quanta 250 FEG scanning electron microscope.

Transmission Electron Microscopy (TEM). The samples were prepared, fixed and dehydrated as above, and stained with 2% uranyl acetate in 70% ethanol at room temperature overnight. The cells were washed three times with acetone and embedded in Epon. The embedded samples were sectioned in 60 nm thick slices on a sliding ultramicrotome. Thin sections supported on copper grids were examined in a Tecnai G2 F20 microscope operated at 200 kV.

Flow cytometry. After cell washing, 200 μL of RBC suspension at 5×10^6 cells mL^{-1} were mixed with 200 μL of FITC-MSN suspensions in PBS at 20 μg mL^{-1}, and incubated at room temperature for 2 h before flow cytometry analysis in a BD FACSCanto instrument.

Confocal Fluorescence Microscopy. 200 μL of PKH26 labeled RBC suspension at 5×10^6 cells mL^{-1} were mixed with 200 μL of FITC-MSN suspensions in PBS at 20 μg mL^{-1}, and incubated at room temperature for 2 h. An aliquot of sample was mounted between plastic coverslips and imaged in a Leica SP5 X confocal system.

Deformability assay. 1.5 mL of packed RBCs were washed and diluted to 30 mL with PBS (5% hematocrit). The diluted RBC suspension (1 mL) was then mixed with MSN suspensions in PBS (4 mL) at various final concentrations of 10, 20 and 50 μg mL^{-1} with PBS as control. The mixture was gently vortexed and incubated at room temperature for 2 h before filtering through polycarbonate membrane with straight channels of 3 μm pore diameter (Nucleopore, Fisher, USA) under a constant negative pressure (-20 cm H_2O). The time for 0.5 mL RBC suspension to pass through the membrane was recorded and the deformability index (DI) was calculated as the volume of red blood cells filtered per minute. Data were presented as mean values of triplicate experiments. The present method and apparatus for RBC filterability measurement have been described in detail elsewhere.[41]

ACKNOWLEDGEMENT

This manuscript has been dedicated in memory of our dear mentor and friend, Victor S.-Y. Lin. This research is supported by the U.S. National Science Foundation NSF (CHE-0809521).

REFERENCES

(1) Slowing, I. I.; Vivero-Escoto, J. L.; Trewyn, B. G.; Lin, V. S. Y. *J. Mater. Chem.* 2010, *20*, 7924.

(2) Cai, Q.; Lin, W. Y.; Xiao, F. S.; Pang, W. Q.; Chen, X. H.; Zou, B. S. *Microporous Mesoporous Mater.* 1999, *32*, 1.

(3) Huh, S.; Wiench, J. W.; Yoo, J.-C.; Pruski, M.; Lin, V. S. Y. *Chem. Mater.* 2003, *15*, 4247.

(4) Lu, F.; Wu, S.-H.; Hung, Y.; Mou, C.-Y. *Small* 2009, *5*, 1408.

(5) Linton, P.; Alfredsson, V. *Chem. Mater.* 2008, *20*, 2878.

(6) Descalzo, A. B.; Martinez-Manez, R.; Sancenon, F.; Hoffmann, K.; Rurack, K. *Angew. Chem., Int. Ed.* 2006, *45*, 5924.

(7) Coti, K. K.; Belowich, M. E.; Liong, M.; Ambrogio, M. W.; Lau, Y. A.; Khatib, H. A.; Zink, J. I.; Khashab, N. M.; Stoddart, J. F. *Nanoscale* 2009, *1*, 16.

(8) Zhao, Y.; Vivero-Escoto, J. L.; Slowing, I. I.; Trewyn, B. G.; Lin, V. S. Y. *Expert Opin. Drug Delivery* 2010, *7*, 1013.

(9) Shen, S.; Chow, P. S.; Chen, F.; Tan, R. B. H. *Chem. Pharm. Bull.* 2007, *55*, 985.

(10) Vivero-Escoto, J. L.; Slowing, I. I.; Trewyn, B. G.; Lin, V. S. Y. *Small* 2010, *6*, 1952.

(11) Slowing, I. I.; Trewyn, B. G.; Lin, V. S. Y. *J. Am. Chem. Soc.* 2007, *129*, 8845.

(12) Kim, S.-I.; Pham, T. T.; Lee, J.-W.; Roh, S.-H. *J. Nanosci. Nanotechnol.* 2010, *10*, 3467.

(13) Nguyen, T. P. B.; Lee, J.-W.; Shim, W. G.; Moon, H. *Microporous Mesoporous Mater.* 2008, *110*, 560.

(14) Doadrio, J. C.; Sousa, E. M. B.; Izquierdo-Barba, I.; Doadrio, A. L.; Perez-Pariente, J.; Vallet-Regi, M. *J. Mater. Chem.* 2006, *16*, 462.

(15) Zhu, Y.; Kaskel, S.; Ikoma, T.; Hanagata, N. *Microporous Mesoporous Mater.* 2009, *123*, 107.

(16) Mercuri, L. P.; Carvalho, L. V.; Lima, F. A.; Quayle, C.; Fantini, M. C. A.; Tanaka, G. S.; Cabrera, W. H.; Furtado, M. F. D.; Tambourgi, D. V.; Matos, J. d. R.; Jaroniec, M.; Sant'Anna, O. A. *Small* 2006, *2*, 254.

(17) Zhao, Y.; Trewyn, B. G.; Slowing, I. I.; Lin, V. S. Y. *J. Am. Chem. Soc.* 2009, *131*, 8398.

(18) Lee, J. E.; Lee, N.; Kim, H.; Kim, J.; Choi, S. H.; Kim, J. H.; Kim, T.; Song, I. C.; Park, S. P.; Moon, W. K.; Hyeon, T. *J. Am. Chem. Soc.* 2010, *132*, 552.

(19) Liong, M.; Lu, J.; Kovochich, M.; Xia, T.; Ruehm, S. G.; Nel, A. E.; Tamanoi, F.; Zink, J. I. *ACS Nano* 2008, *2*, 889.

(20) Tu, H.-L.; Lin, Y.-S.; Lin, H.-Y.; Hung, Y.; Lo, L.-W.; Chen, Y.-F.; Mou, C.-Y. *Advanced Materials* 2009, *21*, 172.

(21) Taylor, K. M. L.; Kim, J. S.; Rieter, W. J.; An, H.; Lin, W.; Lin, W. *J. Am. Chem. Soc.* 2008, *130*, 2154.

(22) Lee, C.-H.; Cheng, S.-H.; Wang, Y.-J.; Chen, Y.-C.; Chen, N.-T.; Souris, J.; Chen, C.-T.; Mou, C.-Y.; Yang, C.-S.; Lo, L.-W. *Adv. Funct. Mater.* 2009, *19*, 215.

(23) Lu, J.; Liong, M.; Li, Z.; Zink, J. I.; Tamanoi, F. *Small* 2010, *6*, 1794.

(24) Kim, J.; Kim, H. S.; Lee, N.; Kim, T.; Kim, H.; Yu, T.; Song, I. C.; Moon, W. K.; Hyeon, T. *Angew. Chem., Int. Ed.* 2008, *47*, 8438.

(25) Meng, H.; Liong, M.; Xia, T.; Li, Z.; Ji, Z.; Zink, J. I.; Nel, A. E. *ACS Nano* 2010, *4*, 4539.

(26) Tao, Z.; Morrow, M. P.; Asefa, T.; Sharma, K. K.; Duncan, C.; Anan, A.; Penefsky, H. S.; Goodisman, J.; Souid, A.-K. *Nano Lett.* 2008, *8*, 1517.

(27) Hudson, S. P.; Padera, R. F.; Langer, R.; Kohane, D. S. *Biomaterials* 2008, *29*, 4045.

(28) Heikkilae, T.; Santos, H. A.; Kumar, N.; Murzin, D. Y.; Salonen, J.; Laaksonen, T.; Peltonen, L.; Hirvonen, J.; Lehto, V.-P. *Eur. J. Pharm. Biopharm.* 2010, *74*, 483.

(29) Al Shamsi, M.; Al Samri, M. T.; Al-Salam, S.; Conca, W.; Shaban, S.; Benedict, S.; Tariq, S.; Biradar, A. V.; Penefsky, H. S.; Asefa, T. *Chem. Res. Toxicol.* 2010, *23*, 1796.

(30) Slowing, I. I.; Wu, C.-W.; Vivero-Escoto, J. L.; Lin, V. S. Y. *Small* 2009, *5*, 57.

(31) Lin, Y.-S.; Haynes, C. L. *J. Am. Chem. Soc.* 2010, *132*, 4834.

(32) Lin, Y.-S.; Haynes, C. L. *Chem. Mater.* 2009, *21*, 3979.

(33) Lai, C.-Y.; Trewyn, B. G.; Jeftinija, D. M.; Jeftinija, K.; Xu, S.; Jeftinija, S.; Lin, V. S. Y. *J. Am. Chem. Soc.* 2003, *125*, 4451.

(34) Slowing, I.; Trewyn, B. G.; Lin, V. S. Y. *J. Am. Chem. Soc.* 2006, *128*, 14792.

(35) Radu, D. R.; Lai, C.-Y.; Huang, J.; Shu, X.; Lin, V. S. Y. *Chemical Communications* 2005, 1264.

(36) Radu, D. R.; Lai, C.-Y.; Jeftinija, K.; Rowe, E. W.; Jeftinija, S.; Lin, V. S. Y. *J. Am. Chem. Soc.* 2004, *126*, 13216.

(37) Hom, C.; Lu, J.; Liong, M.; Luo, H.; Li, Z.; Zink, J. I.; Tamanoi, F. *Small* 2010, *6*, 1185.

(38) Torney, F.; Trewyn, B. G.; Lin, V. S. Y.; Wang, K. *Nat. Nanotechnol.* 2007, *2*, 295.

(39) Wang, L.-S.; Wu, L.-C.; Lu, S.-Y.; Chang, L.-L.; Teng, I. T.; Yang, C.-M.; Ho, J.-a. A. *ACS Nano* 2010, *4*, 4371.

(40) Chambers, E.; Mitragotri, S. *J. Controlled Release* 2004, *100*, 111.

(41) Reid, H. L.; Barnes, A. J.; Lock, P. J.; Dormandy, J. A.; Dormandy, T. L. *J Clin Pathol* 1976, *29*, 855.

(42) Yawata, Y. *Cell membrane : the red blood cell as a model*; Weinheim : Wiley-VCH, 2003.

(43) Roiter, Y.; Ornatska, M.; Rammohan, A. R.; Balakrishnan, J.; Heine, D. R.; Minko, S. *Nano Lett.* 2008, *8*, 941.

(44) Lipowsky, R.; Dobereiner, H. G. *Europhys. Lett.* 1998, *43*, 219.

(45) Deserno, M.; Gelbart, W. M. *J. Phys. Chem. B* 2002, *106*, 5543.

(46) Fleck, C. C.; Netz, R. R. *Europhys. Lett.* 2004, *67*, 314.

(47) Reynwar, B. J.; Illya, G.; Harmandaris, V. A.; Mueller, M. M.; Kremer, K.; Deserno, M. *Nature* 2007, *447*, 461.

(48) Zhu, H. Y.; Zhao, X. S.; Lu, G. Q.; Do, D. D. *Langmuir* 1996, *12*, 6513.

(49) Giri, S.; Trewyn, B. G.; Stellmaker, M. P.; Lin, V. S. Y. *Angew. Chem., Int. Ed.* 2005, *44*, 5038.

(50) Vivero-Escoto, J. L.; Slowing, I. I.; Wu, C.-W.; Lin, V. S. Y. *J. Am. Chem. Soc.* 2009, *131*, 3462.

(51) Zhu, C.-L.; Song, X.-Y.; Zhou, W.-H.; Yang, H.-H.; Wen, Y.-H.; Wang, X.-R. *J. Mater. Chem.* 2009, *19*, 7765.

(52) He, Q.; Zhang, Z.; Gao, Y.; Shi, J.; Li, Y. *Small* 2009, *5*, 2722.

(53) Hall, S. S.; Mitragotri, S.; Daugherty, P. S. *Biotechnol. Prog.* 2007, *23*, 749.

(54) He, Q.; Zhang, J.; Shi, J.; Zhu, Z.; Zhang, L.; Bu, W.; Guo, L.; Chen, Y. *Biomaterials* 2010, *31*, 1085.

(55) Gao, F.; Botella, P.; Corma, A.; Blesa, J.; Dong, L. *J. Phys. Chem. B* 2009, *113*, 1796.

(56) Caravajal, G. S.; Leyden, D. E.; Quinting, G. R.; Maciel, G. E. *Anal. Chem.* 1988, *60*, 1776.

(57) Luquita, A.; Urli, L.; Svetaz, M. J.; Gennaro, A. M.; Giorgetti, M. E.; Pistone, G.; Volpintesta, R.; Palatnik, S.; Rasia, M. *Journal of Biomedical Science* 2010, *17*, 1.

(58) Brown Clinton, D.; Ghali Halim, S.; Zhao, Z.; Thomas Lorraine, L.; Friedman Eli, A. *Kidney Int* 2005, *67*, 295.

(59) Kikuchi, Y.; Koyama, T. *Am. J. Physiol.* 1984, *247*, H739.

(60) De Paoli Lacerda, S. H.; Park, J.-J.; Meuse, C.; Pristinski, D.; Becker, M. L.; Karim, A.; Douglas, J. F. *ACS Nano* 2010, *4*, 365.

(61) Semberova, J.; De Paoli Lacerda, S. H.; Simakova, O.; Holada, K.; Gelderman, M. P.; Simak, J. *Nano Lett.* 2009, *9*, 3312.

APPENDIX: Supporting Information

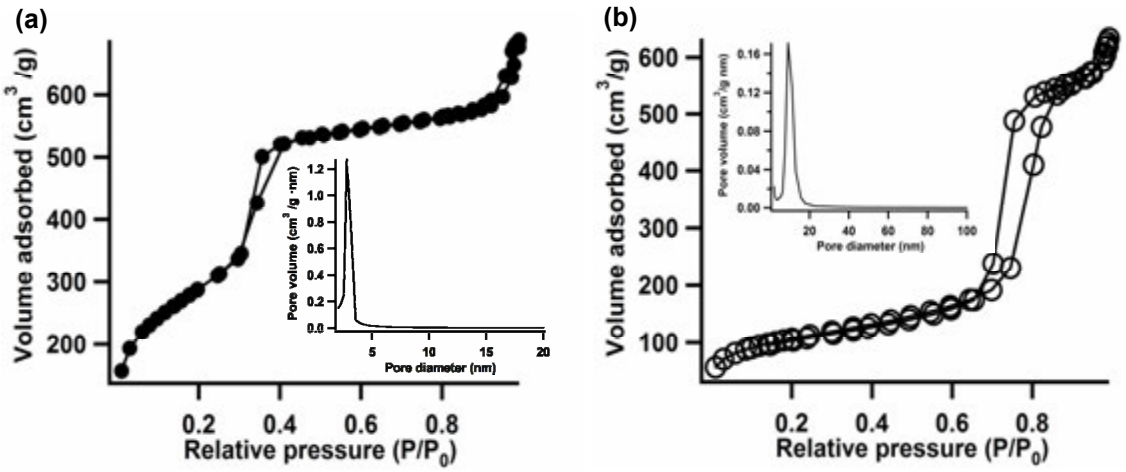

Figure S1. Linear plot of the nitrogen sorption isotherms and pore size distributions of **(a)** *s*-MSN and **(b)** *l*-MSN. Surface areas of *s*-MSN and *l*-MSN were calculated to be 1051.6 ± 2.2 m^2 g^{-1} and 387.0 ± 1.3 m^2 g^{-1}, respectively.

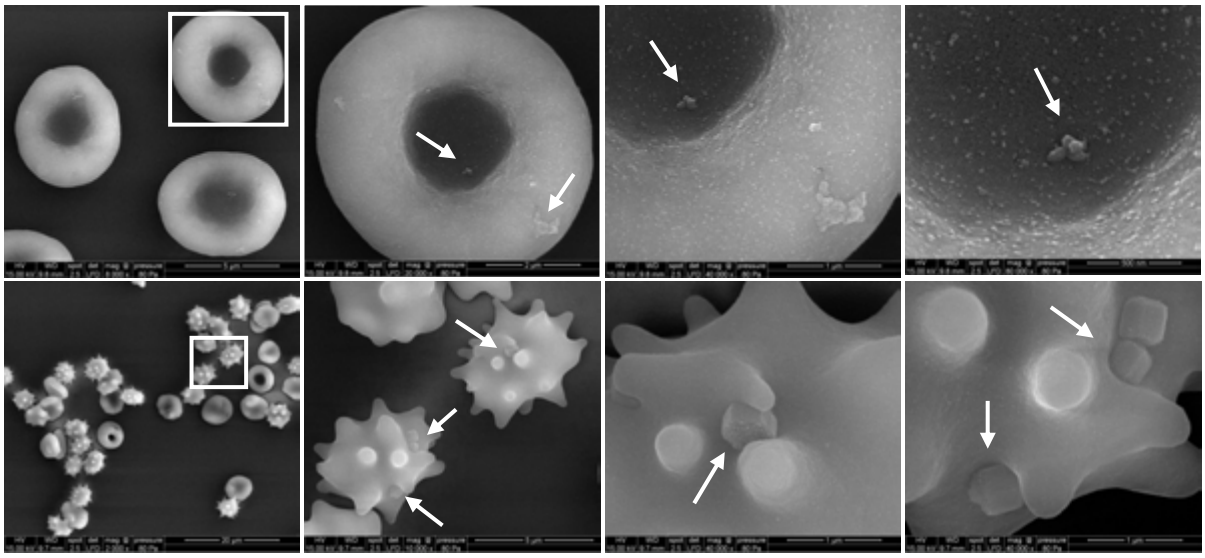

Figure S2. Scanning electron micrographs (SEM) of RBCs (5% hematocrit) incubated with 100 μg mL^{-1} *s*-MSN (top) and *l*-MSN (bottom). Images increase in magnification from left to right with features highlighted with white squares or arrows, indicating the location of particles attached on RBC membrane.

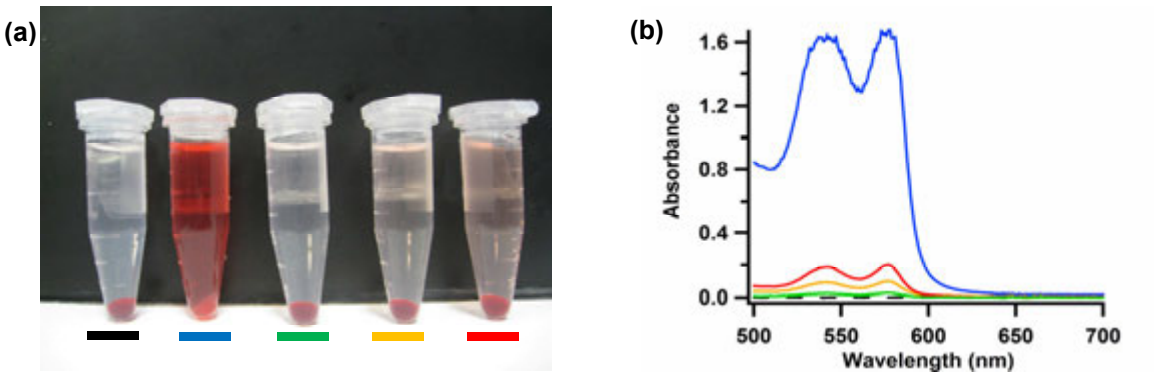

Figure S3. Hemolysis assay for *l*-MSN using water as a positive control (blue lines) and PBS as a negative control (dashed black lines). The materials were suspended at 20 (green), 50 (yellow) and 100 (red) μg mL^{-1}. The mixtures were centrifuged to detect the presence of hemoglobin (red) in the supernatant visually (a) and by absorption at 541 nm (b).

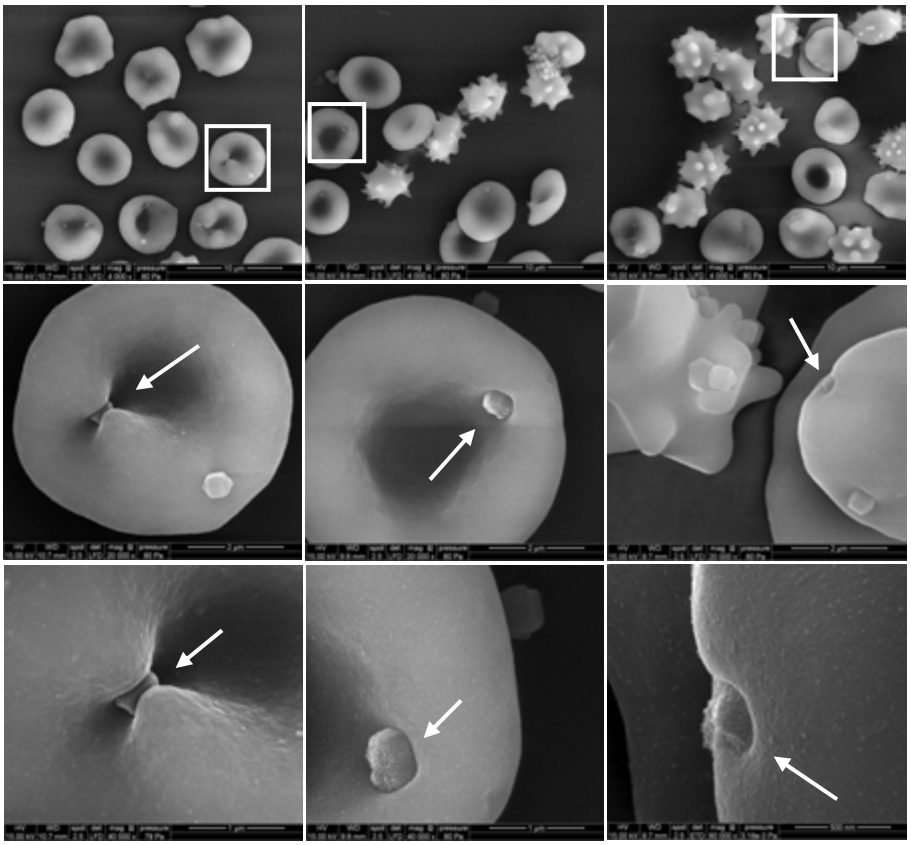

Figure S4. Scanning electron micrographs (SEM) of RBCs (5% hematocrit) incubated with 20 μg mL^{-1} (left), 50 μg mL^{-1}(middle), and 100 μg mL^{-1} of *l*-MSN (right). Percent of spiculated RBCs were observed to be < 10%, ~50% and ~90% from left to right. Images increase in magnification from top to bottom with features highlighted with white squares or arrows, indicating the location of particles attached on RBC membrane.

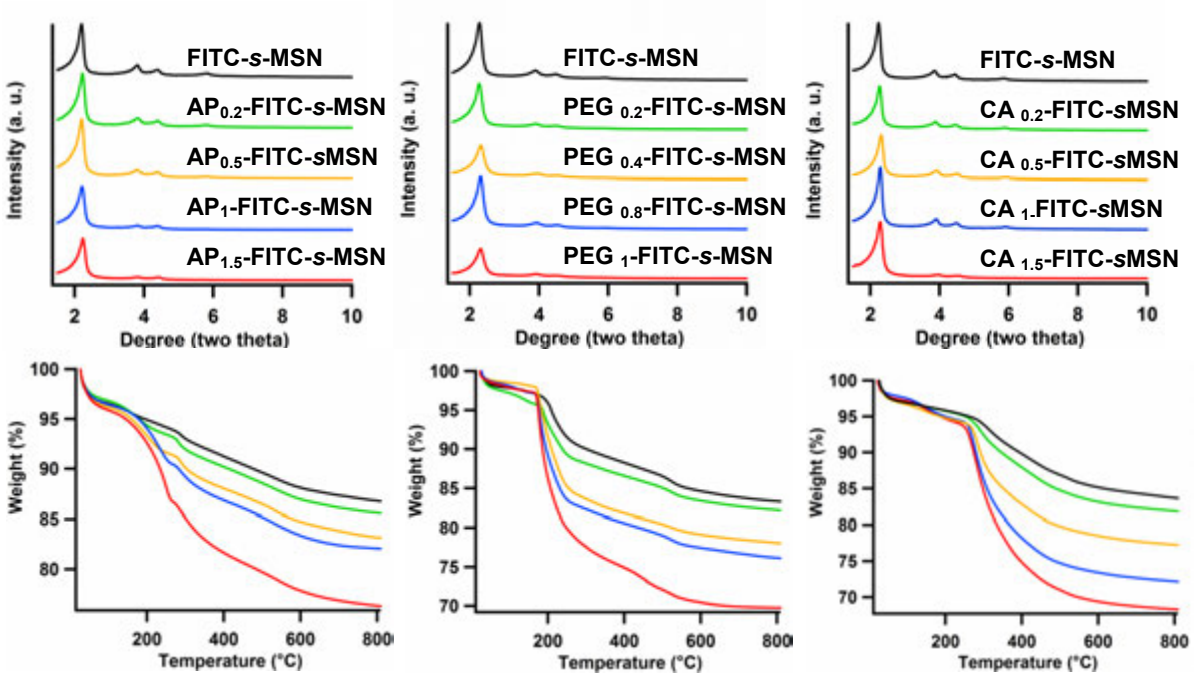

Figure S5. X-ray diffraction patterns (top) and thermogravimetric analysis (bottom) of FITC-*s*-MSN, AP_x-FITC-*s*-MSN (left), PEG_x-FITC-*s*-MSN (middle) and CA_x-FITC-*s*-MSN (right) (*x*: amount of organic groups introduced in mmol g^{-1}).

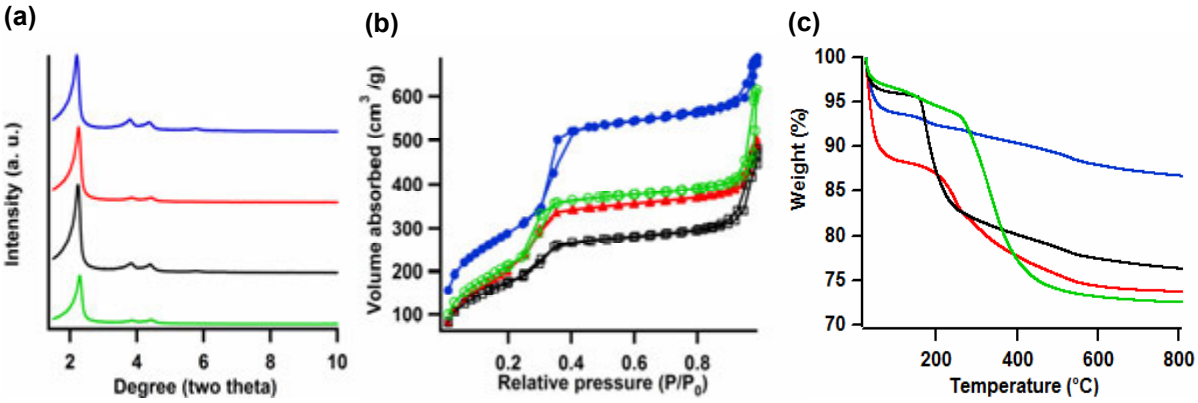

Figure S6. (a) X-ray diffraction (XRD) patterns, (b) linear plot of the nitrogen sorption isotherms and (c) thermogravimetric analysis (TGA) of *s*-MSN (blue), $AP_{1.5}$-*s*-MSN (red), PEG_1-*s*-MSN (black) and $CA_{1.5}$-*s*-MSN (green).

Table S1. Characteristics of FITC-*s*-MSN, AP_x-FITC-*s*-MSN, PEG_x-FITC-*s*-MSN and CA_x-FITC-*s*-MSN (*x*: amount of organic groups introduced in mmol g^{-1}).

Materials	Surface groups (mmol g^{-1})	Zeta potential (mV)	Surface area (m^2 g^{-1})	Pore size (nm)
FITC-*s*-MSN	0.02	-27.9	1043.4 ± 4.2	3.0
$AP_{0.2}$-FITC--*s*MSN	0.1-0.2	-22.9	948.3 ± 7.9	2.8
$AP_{0.5}$-FITC-*s*-MSN	0.4-0.6	-10.9	878.7 ± 11.7	2.8
AP_1-FITC-*s*-MSN	0.6-0.8	+3.2	796.8 ± 1.6	2.8
$AP_{1.5}$-FITC-*s*-MSN	1.2-1.6	+6.87	689.0 ± 29.0	2.7
FITC-*s*-MSN	0.03	-29.3	1036.4 ± 11.2	2.6
$PEG_{0.2}$-FITC-*s*-MSN	0.03-0.04	-26.1	985.6 ± 9.0	2.6
$PEG_{0.4}$-FITC-*s*-MSN	0.1-0.2	-22.3	839.6 ± 9.3	2.4
$PEG_{0.8}$-FITC-*s*-MSN	0.2-0.3	-20.7	770.8 ± 1.6	2.4
PEG_1-FITC-*s*-MSN	0.4-0.5	-13.1	628.9 ± 2.6	2.4
FITC-*s*-MSN	0.03	-28.6	1107.8 ± 8.6	2.7
$CA_{0.2}$-FITC-*s*-MSN	0.07-0.1	-34.3	967.4 ± 2.9	2.5
$CA_{0.5}$-FITC-*s*-MSN	0.3-0.4	-36.1	913.6 ± 19.2	2.4
CA_1-FITC-*s*-MSN	0.5-0.7	-39.2	863.0 ± 9.2	2.4
$CA_{1.5}$-FITC-*s*-MSN	0.7-1	-42.7	779.2 ± 5.0	2.5

Table S2. Characteristics of *s*-MSN, $AP_{1.5}$-*s*-MSN, PEG_1-*s*-MSN, $CA_{1.5}$-*s*-MSN and *l*-MSN.

Materials	Surface groups (mmol g^{-1})	Zeta potential (mV)	Surface area (m^2 g^{-1})	Pore size (nm)	Hydrodynamic particle size (nm)
s-MSN		-22.2	1051.6 ± 2.2	3.1	122
$AP_{1.5}$-*s*-MSN	1.1-1.5	+5.79	780.3 ± 9.0	2.4	142
PEG_1-*s*-MSN	0.3-0.4	-11.6	650.5 ± 2.9	2.7	122
$CA_{1.5}$-*s*-MSN	0.6-0.9	-43.1	792.9 ± 4.4	2.9	142
l-MSN		-16.5	387.0 ± 1.3	9.0	531

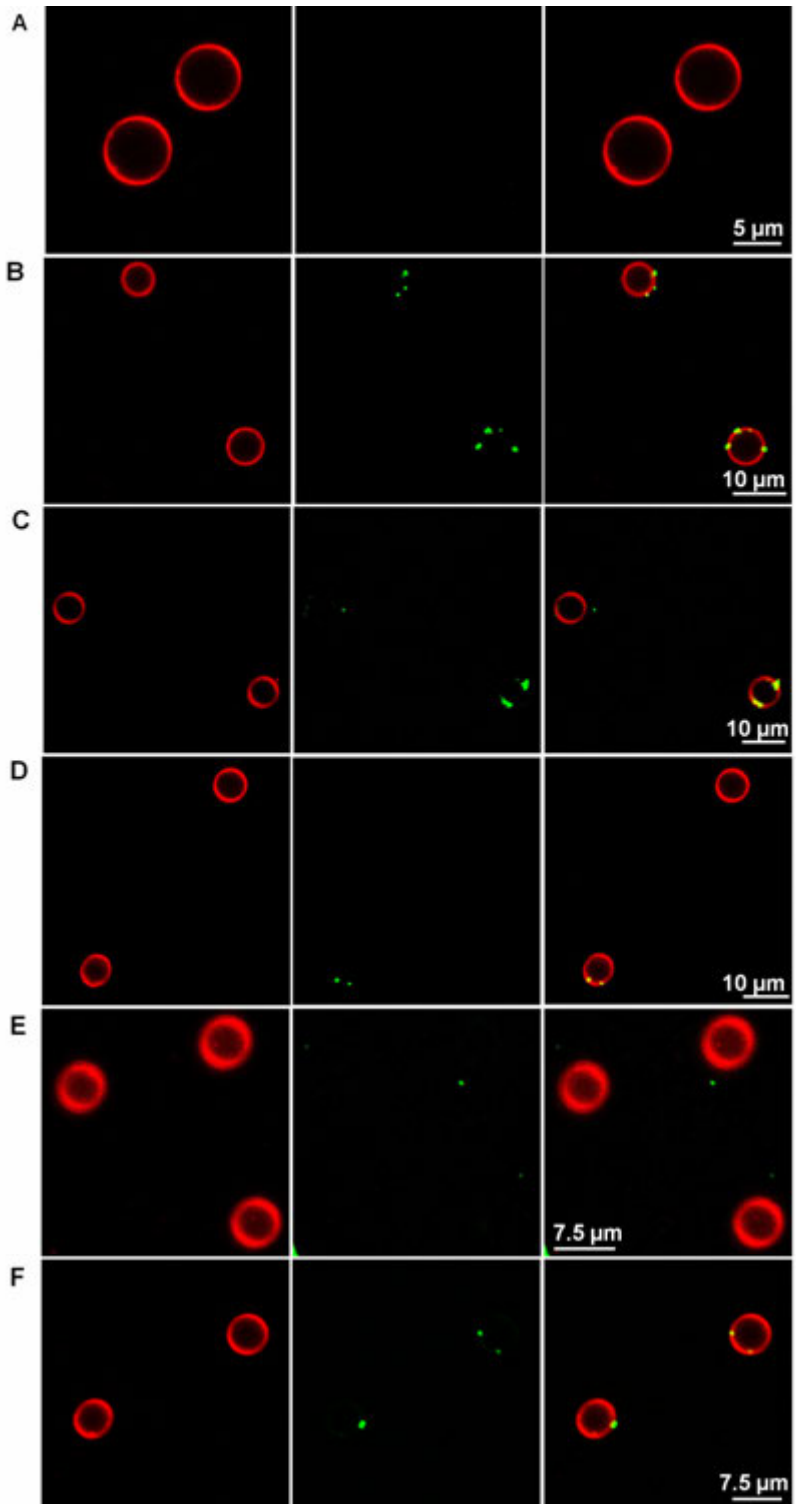

Figure S7. Confocal fluorescence micrographs of (A) RBCs (5×10^6 cells mL^{-1}) incubated with 20 μg mL^{-1} of (B) FITC-*l*-MSN, (C) FITC-*s*-MSN, (D) $AP_{1.5}$-FITC-*s*-MSN, (E) PEG_1-FITC-*s*-MSN and (F) $CA_{1.5}$-FITC-*s*-MSN. The channels from left to right correspond to red blood cells stained with PKH26 red fluorescence dye, FITC-MSNs and the merged images.

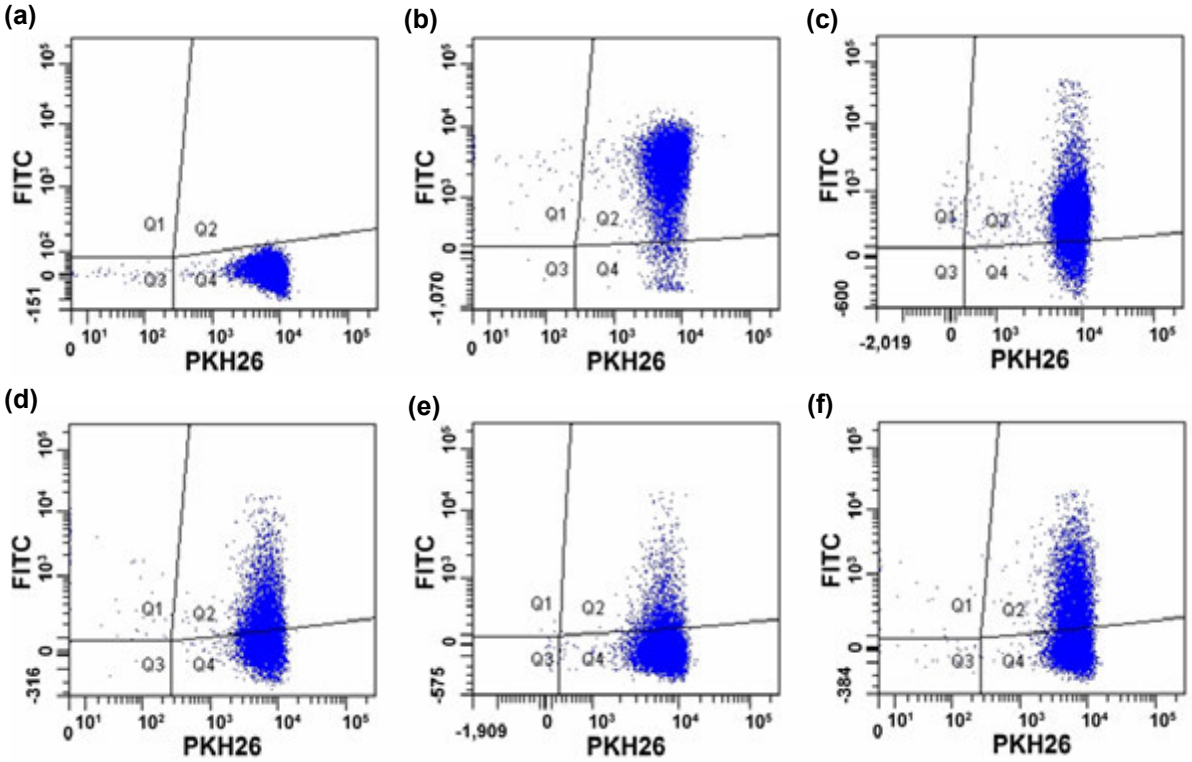

Figure S8. Dot plot from the flow cytometry analysis of (a) PKH26 labled RBC incubated with (b) FITC-*l*-MSN, (c) FITC-*s*-MSN, (d) $AP_{1.5}$-FITC-*s*-MSN, (e) PEG_1-FITC-*s*MSN and (f) $CA_{1.5}$-FITC-*s*-MSN. The axes correspond to the intensity of red fluorescence due to PKH26 labeling (horizontal axis) and green fluorescence due to the attachment of FITC-MSNs onto PKH26-RBCs (vertical axis). The plot was gated to show PKH26 labeled RBCs in area Q4 and FITC-fluorescent PKH26-RBCs in area Q2.

CHAPTER 4. MESOPOROUS SILICA NANOPARTICLE TETHERED SINGLE SITE PLATINUM CATALYSTS FOR THE FUNCTIONALIZATION OF ETHYLENE

A manuscript submitted for publication in ***Journal of American Chemical Society***

Jeremy R. Andreatta, Hung-Ting Chen, **Xiaoxing Sun**, Chih-Hsiang Tsai, Brian G. Trewyn, Victor S.-Y. Lin, T. Brent Gunnoe

ABSTRACT

Mesoporous silica nanoparticles have been used for tethering a platinum catalyst to achieve enhanced thermal stability and longevity. We synthesized and characterized the mesoporous silica nanoparticle supported Pt(II) complexes. We then investigated the heterogeneous system by comparing it with the homogeneous catalyst on the catalytic performance for the hydrophenylation of ethylene and the durability to high temperature.

ARTICLE

Alkyl arenes, especially ethyl benzene, are produced on the millions of tons scale per annum and serve as important precursors and commodity chemicals for a variety of industrial sectors ranging from pharmaceutical to polymers to surfactants. Alkylbenzene derivatives account for about 75% of the world wide benzene use, with ethylbenezne (EB) being the fate for 54% of the world´s available benzene supply.[1] Traditionally, Friedel-Crafts (FC) catalysis is utilized for the production of simple alkyl arenes.[2] FC catalysts suffer from several drawbacks including polyalkylation, lack of regioselectivity for dialkylated arenes, inability for selective formation of linear alkyl arenes, use of toxic starting materials (e.g. HF as a co-catalyst), and lack of catalyst recyclability. Recent developments of zeolite materials have been able to address some of the above problems; however, some of the limitations of both FC and zeolite catalytsts are inherent to the mechanism.

Transition metal mediated insertion of olefins into arene C-H bonds has been reported using Ir, Ru, and Pt complexes (Scheme 1).[3] The hydroarylation of ethylene using [^{t}bpyPtPh(THF)][BAr$^{F}_{4}$] (**1**) [^{t}bpy = 4,4´-di-*tert*-butyl-2,2´-bipyridyl,Ph = phenyl, BAr$^{F}_{4}$ = tetrakis(3,5-bis(trifluoromethyl)phenyl)borate] as a homogeneous catalyst has

been studied in detail and proven to be an effective catalyst for the selective formation of ethylbenzene (EtPh).[4] One drawback of the homogeneous system is the lack of thermal stability and/or catalyst longevity. Herein, we report the synthesis, characterization, and catalytic activity of mesoporous silica nanoparticle (MSN) supported bpyPt complexes for the hydrophenylation of ethylene.

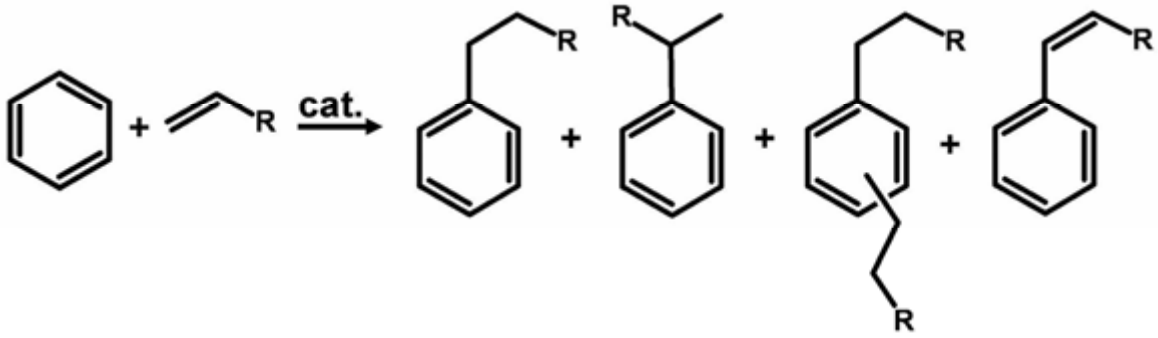

Scheme 1. Transition metal catalyzed hydroarylation of olefins.

The area of MSN materials, especially as catalyst scaffolds, has recently received much attention.[5] Examples include supported catalysts for olefin hydrogenation,[6-10] Heck and Sonogashira reactions,[11-14] ring opening of epoxides,[15] hydroamination of olefins,[16] and hydrocarboxylation of aryl olefins and alcohols[17] among others. In many cases, MSN supported catalysts exhibit not only increased stability, but also result in an increase in the selectivity versus its homogeneous analog. For example, Tilley and coworkers observed marked increases in the production of (Z)-1-phenyl-propene during the partial hydrogenation of the parent alkyne.[10] Using the general strategies developed for the attachment of various single site transition metal catalysts, we report the development of a MSN tethered Pt(II) bipyridine catalysts for the hydrophenylation of olefins.

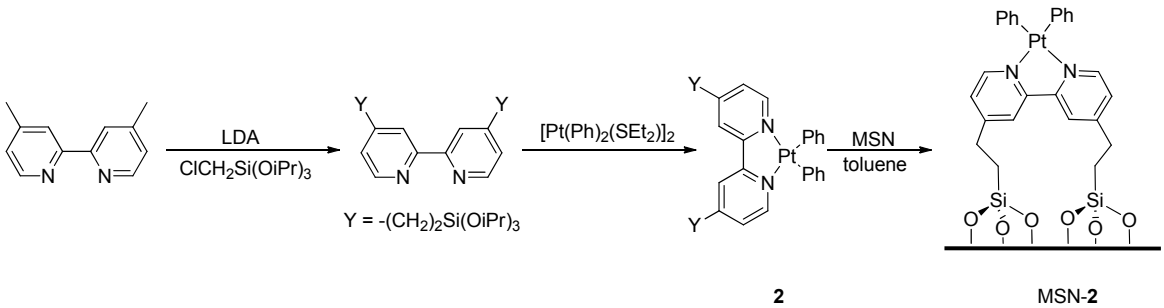

Scheme 2. Synthesis of SibpyPt(Ph)$_2$ and attachment via post-synthesis grafting to MSN.

Initial studies focused on the modification of the 2,2′-bipyridine (bpy) ligand architecture at the 4 and 4′ positions while maintaining a similar electronic environment about the platinum center. The synthesis of a bpy bearing alkyl siloxane moieties was achieved via the lithiation of 4,4′-dimethyl bipyridine followed by the addition of chloromethyltriisopropoxysilane (Scheme 2) to yield 4,4′-bis(2-triisopropoxysilyl)ethyl)-2,2′-bipyridine (^{Si}bpy).

Analogous to the synthesis of the **1**, the addition of $[Pt(Ph)_2(SEt_2)]_2$ to the ligand in an ether solution afforded the desired ^{Si}bpyPt(Ph)$_2$ **(2)** product in about 40 % yield. Attachment to the MSN was achieved via post-synthesis grafting in refluxing toluene. ^{29}Si and ^{13}C solid state NMR (ssNMR), along with TEM, ICP-OES, and N_2 sorption were used to characterize MSN-2. The TEM image and the low-angle X-ray diffraction pattern clearly show that the 2-d hexagonal mesopore structure of MSN-2 remained intact after synthesis and metal ligand attachment. Nitrogen sorption analysis of MSN-2 measured a BET surface area of 610 m^2 g^{-1}, along with a BJH mean pore diameter of 5.8 nm, indicating no sign of pore blockage. The catalyst loading of MSN-2 was assessed by ICP-OES, which was determined to be 0.038 mmol g^{-1}. The ^{13}C ssNMR spectrum of MSN-2 indicates that the Pt-Ph bonds are still present in the product material and a comparison of the solution and ssNMR demonstrate good agreement (Figure 1).

Initial catalytic studies utilizing MSN-2 under similar reaction conditions for **1** (100 °C) resulted in approximately 100 turnovers (TOs) of ethylbenzene in 24 hours compared to 70 TOs after 16 hours using 1. Additionally, the ratio of dialkylated products to the more desired monosubstituted benzene product was almost identical between the two systems (~20-25%). As with the homogeneous Pt(II) catalyst, styrene production is observed; however, ~5 turnovers of styrene are observed versus the 1-2 that is occasionally observed with **1**.

The heterogeneous catalyst material, MSN-2 was examined over a range of temperatures (100 - 200 °C), ethylene pressures (15 – 500 psi), and the number of equivalents (relative to Pt concentration) of $HBAr^F_4$ (1 -10 equiv.). Optimal conditions for catalysis were obtained at 150 °C, 25 psi ethylene, and 5 equivalents of $HBAr^F_4$. Under optimal reaction conditions, approximately 140 TOs of ethylbenzene 12 TOs of styrene are observed using the MSN tethered Pt catalyst.

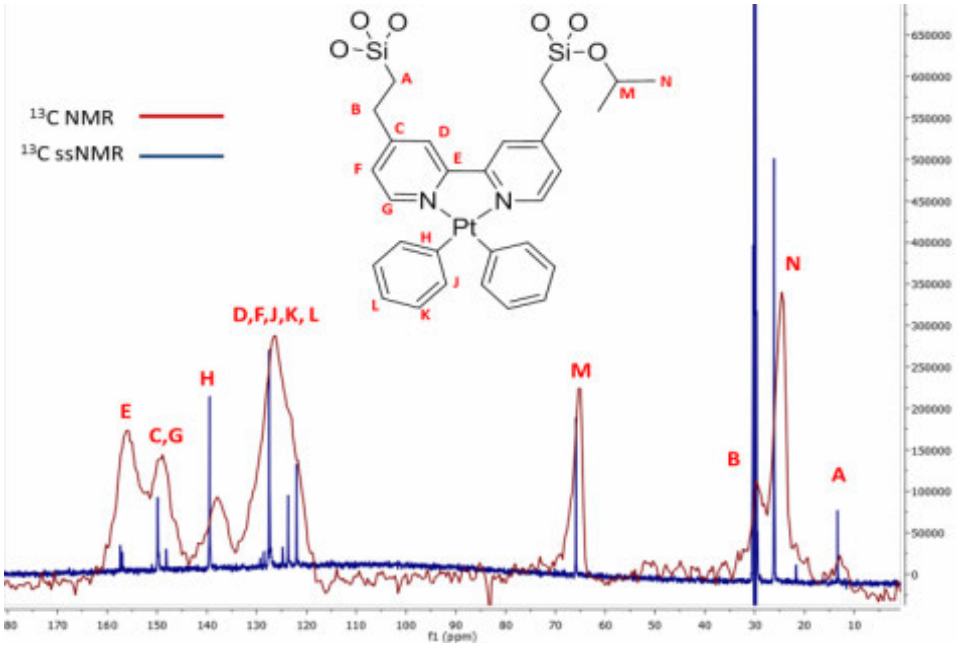

Figure 1. Comparison of ^{13}C NMR spectra of **2** (maroon) and MSN-2(blue).

Additionally, control reactions using MSN, $HBAr^F_4$, Pt(0) on silica, and a combination of MSN and $HBAr^F_4$, and Pt(0) and $HBAr^F_4$ were examined for any activity towards the hydrophenylation of ethylene. In each case, catalysis was not observed.

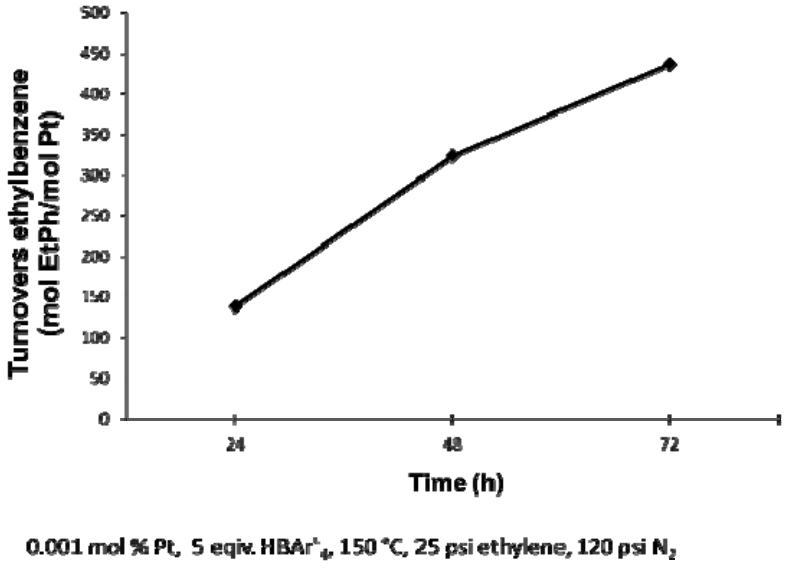

Figure 2. Plot of the production of ethylbenzene versus time using MSN-2.

Catalyst stability was also examined. The homogeneous (^{t}bpy)Pt(II) catalyst showed appreciable degradation after 16 h at 100 °C. Under optimal reaction conditions, the MSN

tethered catalyst demonstrated activity for 72 hours (Figure 2). Interestingly, up to 40 TOs of styrene are observed after 72 hours of reactivity.

In conclusion, we have tethered a (^{t}bpy)Pt(II) catalyst onto the surface of mesoporous silica nanoparticles via a post-synthesis method. The heterogeneous MSN supported Pt(II) catalyst exhibited a dramatically increased thermal stability with no obvious change in catalytic activity.

REFERENCES

(1) Perego, C.; Ingallina, P. *Green Chem.* 2004, *6*, 274.

(2) Olah, G. A.; Molnár, Á. *Hydrocarbon chemistry*; 2nd ed.; Wiley-Interscience: New York, 2003.

(3) Andreatta, J. R.; McKeown, B. A.; Gunnoe, T. B. *J. Organomet. Chem.* 2011, *696*, 305.

(4) McKeown, B. A.; Foley, N. A.; Lee, J. P.; Gunnoe, T. B. *Organometallics* 2008, *27*, 4031.

(5) Slowing, I. I.; Vivero-Escoto, J. L.; Trewyn, B. G.; Lin, V. S. Y. *J Mater Chem* 2010, *20*, 7924.

(6) Dufaud, V.; Beauchesne, F.; Bonneviot, L. *Angew Chem Int Edit* 2005, *44*, 3475.

(7) Lin, W. B.; Mihalcik, D. J. *Angew Chem Int Edit* 2008, *47*, 6229.

(8) Lin, W. B.; Mihalcik, D. J. *Chemcatchem* 2009, *1*, 406.

(9) Huang, Y.; Xu, S.; Lin, V. S. Y. *Chemcatchem* 2011, *3*, 131.

(10) Choi, Y. S.; Moschetta, E. G.; Miller, J. T.; Fasulo, M.; McMurdo, M. J.; Rioux, R. M.; Tilley, T. D. *Acs Catal* 2011, *1*, 1166.

(11) Tsai, F.-Y.; Wu, C.-L.; Mou, C.-Y.; Chao, M.-C.; Lin, H.-P.; Liu, S.-T. *Tetrahedron Letters* 2004, *45*, 7503.

(12) Tsai, F. Y.; Lin, B. N.; Huang, S. H.; Wu, W. Y.; Mou, C. Y. *Molecules* 2010, *15*, 9157.

(13) Sharma, K. K.; Biradar, A. V.; Das, S.; Asefa, T. *Eur J Inorg Chem* 2011, *2011*, 3174.

(14) Bahramian, B.; Bakherad, M.; Keivanloo, A.; Bakherad, Z.; Karrabi, B. *Appl Organomet Chem* 2011, *25*, 420.

(15) Das, S.; Asefa, T. *Acs Catal* 2011, *1*, 502.

(16) Duncan, C.; Biradar, A. V.; Asefa, T. *Acs Catal* 2011, *1*, 736.

(17) Mukhopadhyay, K.; Sarkar, B. R.; Chaudhari, R. V. *Journal of the American Chemical Society* 2002, *124*, 9692.

APPENDIX: Supporting Information

Experimental Procedure

1.1 Materials. Tetramethyl orthosilicate (TMOS) (98 %) was purchased from Aldrich. Non ionic surfactant pluronic 104 (P 104) was purchased from BASF Corporation with a composition of $(EO)_{27}(PO)_{61}(EO)_{27}$. Nanopure water (17.9 MHz) used for MSN synthesis was prepared from a Barnstead E-pure water purification system.

1.2 Synthesis of MSN-10.[1] P 104 (7.0 g, 1.186 mmol) was added to 1.6 M HCl (273.0 g). After stirring at a speed of 400 rpm in a lightly covered 500 ml Erlenmeyer flask at 55 °C for 1 h, tetramethylorthosilicate (TMOS) (10.64 g, 69.9 mmol) was added and stirred for additional 24 h. The resulting mixture was subjected to hydrothermal treatment at 150 °C for 24 h in a 450 ml parr reactor. After cooling, the white solid was collected by filtration, washed with nanopure water and methanol and dried in air. Removal of surfactant (P 104) was done by calcination at 550 °C for 6 h in a programmable oven at a ramp rate of 1.5 °C min^{-1}.

1.3 Synthesis of G-$^{alkyl\text{-}2}$BpyPt-TMOS-MSN.[2] MSN-10 was dried under vacuum at 90 °C for 4 h prior to grafting. For grafting 100 mg of MSN-10 was suspended in 20 ml of dry toluene and 160 mg (0.2 mmol) of 4,4'-bis((2-triisopropoxysilyl)ethyl) 2,2'-bipyridine Pt diphenyl was added to it. The mixture was refluxed at 100 °C for 24 h under argon atmosphere. The resulting mixture was filtered, washed with toluene and methanol, and dried under vacuum overnight.

1.4 Structural Characterization. *X Ray Diffraction.* Powder X-ray diffraction (XRD) measurements were performed using Rigaku Ultima IV diffractometer using a Cu Kα radiation source. *Transmission Electron Microscopy.* The TEM samples were prepared by placing a small aliquot of an aqueous suspension on a lacey carbon film coated 400 mesh copper grid and drying it in air. The TEM images were obtained on a Tecnai F2 microscope operated at 200 kV. *Scanning Electron Microscopy.* Particle morphology was determined by SEM using a Hitachi S 4700 FE-SEM system with 10 kV accelerating voltage. *Surface Characterization.* The surface area and average pore diameter were measured using N_2 adsorption/desorption measurements in a Micromeritics ASAP 2020 BET surface analyzer system. The data were evaluated using Brunauer−Emmett−Teller (BET) and Barrett−Joyner−Halenda (BJH) methods respectively to calculate surface area

and pore distributions. Samples were prepared by degassing at 100 °C for 6 h before analysis.

1.5 Functional group and metal loading characterization. *Solid State NMR (*SS NMR). Surface ligand loadings were determined by ^{29}Si DPMAS. Pt loading was determined by running ICP-OES measurements over Optima 8300 PerkinElmer ICP-OES spectrometer.

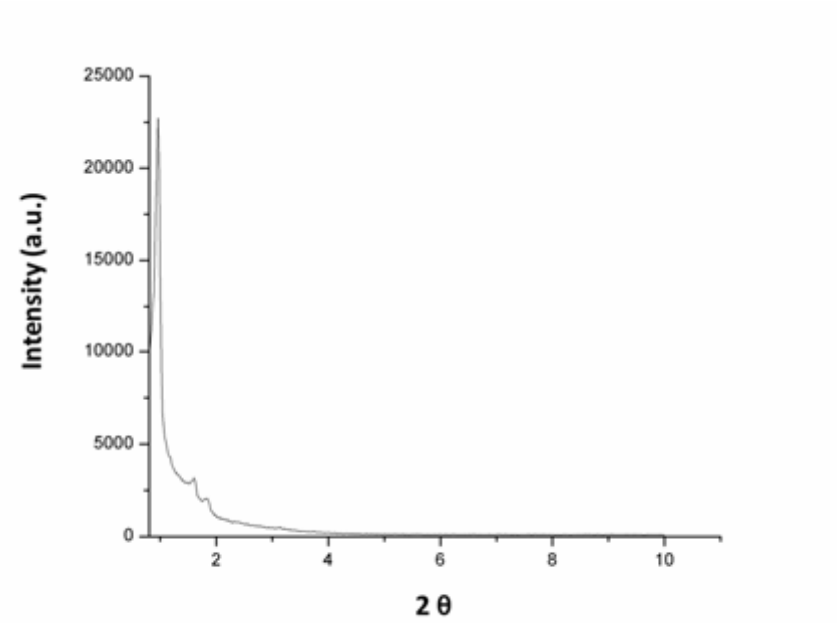

Figure 1. Powder X-ray diffraction pattern of MSN-2.

Table 1.

Sample	S_{BET} (m^2/g)	V_P (cm^3/g)	W_{BJH} (Å)	Loading of Bpy-Pt complex by ^{29}Si NMR (mmol/g)	Loading of Pt by ICP-OES (mmol/g)
G-$^{alkyl\text{-}2}$BpyPt-TMOS-MSN	407	0.85	49	0.04	0.038

The BET surface area (S_{BET}), the mesopore volume (V_p), and the mean mesopore width (W_{BJH}) were obtained from the nitrogen adsorption/desorption data. The amounts of organic functional groups incorporated to the silica materials were estimated from the ^{29}Si DPMAS and ICP-OES.

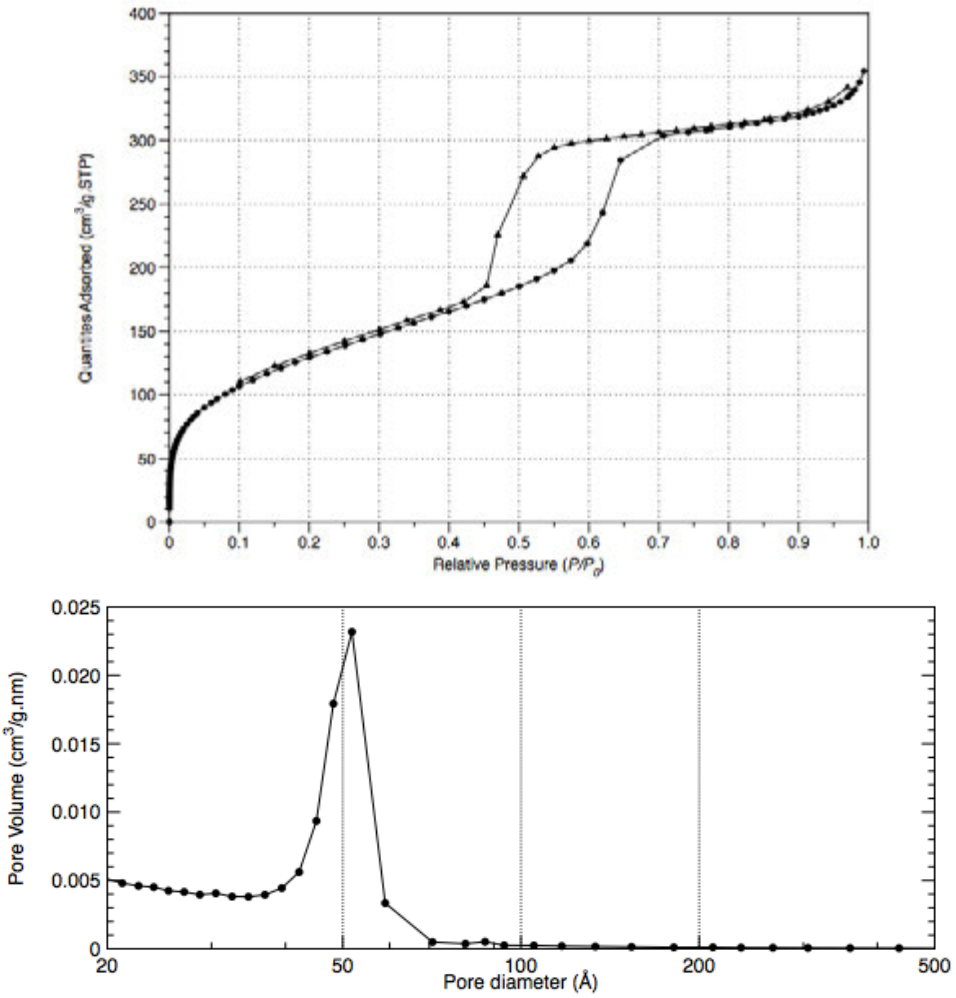

Figure 2. N_2 adsorption/desorption isotherms and pore size distribution of MSN-2.

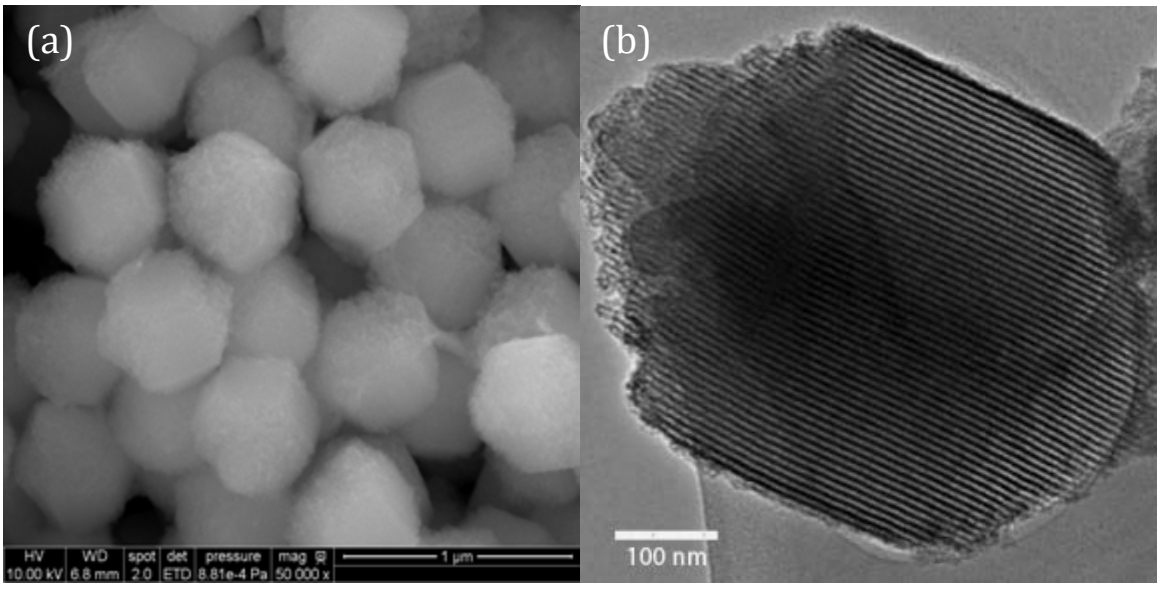

Figure 3. (a) SEM and (b) TEM image of MSN-2.

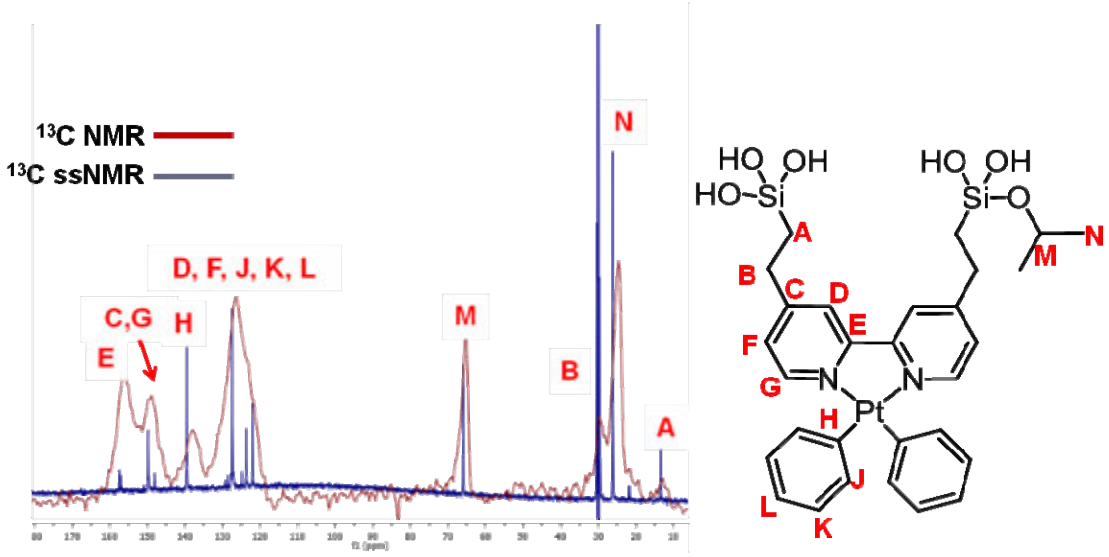

Figure 4. ^{13}C solid state NMR of G-$^{alkyl\text{-}2}$BpyPt-TMOS-MSN, on the right, assignments of the peaks are shown.

FOOTNOTES:

1. Valenstein, J. S.; Kandel, K.; Melcher, F.; Slowing, I. I..; Lin, V. S. –Y.; Trewyn, B.G. *ACS Appl. Mater. Interfaces* **2012**, *4*, 1003−1009
2. In G-$^{alkyl\text{-}2}$BpyPt-TMOS-MSN, G stands for grafting, alkyl is the chain attached to the bipyridyl moiety, 2 denotes that the ligand is bitethered, on the surface of mesoporous silica, Bpy stands for the bipyridyl moiety, Pt is the metal co-ordinated, TMOS (tetramethylorthosilicate) is the silica source used for MSN synthesis.

CHAPTER 5. ONE-POT OXIDATIVE ESTERIFICATION OF ALLYL ALCOHOL CO-CATALYZED BY ALCOHOL DEHYDROGENASE ENZYME AND MESOPOROUS SILICA NANOPARTICLE SUPPORTED GOLD NANOPARTICLES

Xiaoxing Sun, Justin S. Valenstein, and Brian G. Trewyn

ABSTRACT

Supported Au-nanoparticle catalysts used for the oxidative alcohol esterification reaction often suffer from certain deficiencies such as slow alcohol oxidation rate and poor reactivity in aqueous environments. We designed a co-catalyst system that combines the advantages of a biocatalyst, alcohol dehydrogenase, and an inorganic catalyst to accelerate oxidation reactions tandemly. We developed a mesoporous silica nanoparticle supported Au nanoparticles (Au-MSN) catalyst. We identified several factors that affect the catalytic performance of the co-catalyst system. We examined the catalytic performance of this co-catalyst system on the one-pot esterification of allyl alcohol. We envision that this system could lead to the development of a variety of enzyme-metal catalyst pairs for a number of reactions.

1. Introduction

Carboxylic esters are some of the most industrially important products for the synthesis and development of fine chemicals, pharmaceuticals and polymers.[1] The traditional synthesis methods for carboxylic esters not only require multiple reaction steps and harsh reaction conditions, but also produce a large amount of waste.[2-4] Therefore, the development of environmentally benign methods has become a demanding and challenging subject in organic synthesis to address the increasing economical and ecological concerns regarding the conventional methods. Among many synthetic routes that have been investigated, supported Au-nanoparticle (Au NP) catalyzed oxidative esterification may be the most preferred and promising one, as reported by several research groups.[5-10] Because the whole process involves only molecular oxygen as a green oxidant instead of the stoichiometric environmentally harmful oxidants, and avoids

employing strong acids and excessive reactants in the reaction. Moreover, in comparison with many other metal catalysts, Au catalyst exhibits excellent activity and selectivity for the alcohol oxidative esterification without extra ligands,[11] which might be attributed to a number of factors including metal–support interactions and the Au nanoparticles size effect.[9,12] For example, Christensen and coworkers reported the aerobic oxidative esterification of alcohols over Au/TiO_2 catalyst.[10] Miyamura *et al*. synthesized methyl esters through the aerobic oxidation of alcohols over polymer-incarcerated gold nanoparticles.[6] Costa *et al*. performed a one-pot oxidative esterification of benzyl alcohol to methyl benzoate over the Au/MgO catalyst and reached a virtually quantitative yield.[8] It is noteworthy that Yang and coworkers recently demonstrated that the activity of supported Au nanoparticle catalyst is strongly dependent on the Au nanoparticle size. Mesoporous silica materials are more advantageous than other supports due to their ability to manipulate the growth of Au nanoparticles by controlling the amount of Au loaded into the mesopore architecture.[7] Moreover, the large surface area of mesoporous silica material provides better diffusion of substrates and accessibility to the catalyst sites.[13]

However, most of the Au nanoparticle catalyzed carboxylic ester synthetic procedures were performed in methanol solutions to yield only methyl esters. Direct oxidative esterification of alcohols carried out in aqueous solution is rarely reported although aqueous reactions are remarkably safe, and economically and environmentally beneficial.[14] In addition, it has been established that the reaction mechanism is divided into three steps,[15] the dehydrogenation of the alcohol that produces the corresponding aldehyde, the aldehyde transformation to its hemi-acetal form and the further oxidation of the hemi-acetal to the carboxylic ester. The rate determining step (RDS) has been demonstrated to be the α-hydrogen abstraction from alcohol and it limits the overall catalytic performance of supported Au nanoparticle catalyst. Therefore, this major challenge of overcoming the slow RDS requires the Au nanoparticle catalysts for alcohol oxidative esterification reactions to work under either high temperature or high pressure to accelerate the slow alcohol oxidation kinetics, which can be extremely hazardous due to the risk of vigorous explosions.[16] Additionally, high pressure and high temperature reactions are energy and capital intensive processes and identifying new processes that avoid these is critical to maintain sustainability.

Herein, we present the development of a co-catalyst system comprising alcohol dehydrogenase (ADH) enzyme and mesoporous silica nanoparticles supported Au nanoparticles (Au-MSN). We demonstrated that ADH enzyme was capable of converting allyl alcohol to its corresponding aldehyde, so as to accelerate the slow RDS at room temperature. We also proved that the Au-MSN catalyzed the conversion of the aldehyde to the carboxylic ester in aqueous solution without additional acid or base. We further investigated the catalytic performance of our co-catalyst system for the one-pot synthesis of allyl acrylate ester through aqueous oxidative esterification reaction. As shown in Figure 1, ADH enzyme efficiently aids the oxidation of allyl alcohol to acrolein,[17] and Au-MSN subsequently oxidizes acrolein in fast kinetics, generating allyl acrylate, an important chemical in the polymer industry. We compared a number of experimental conditions and determined several factors that affect this tandem reaction kinetics.

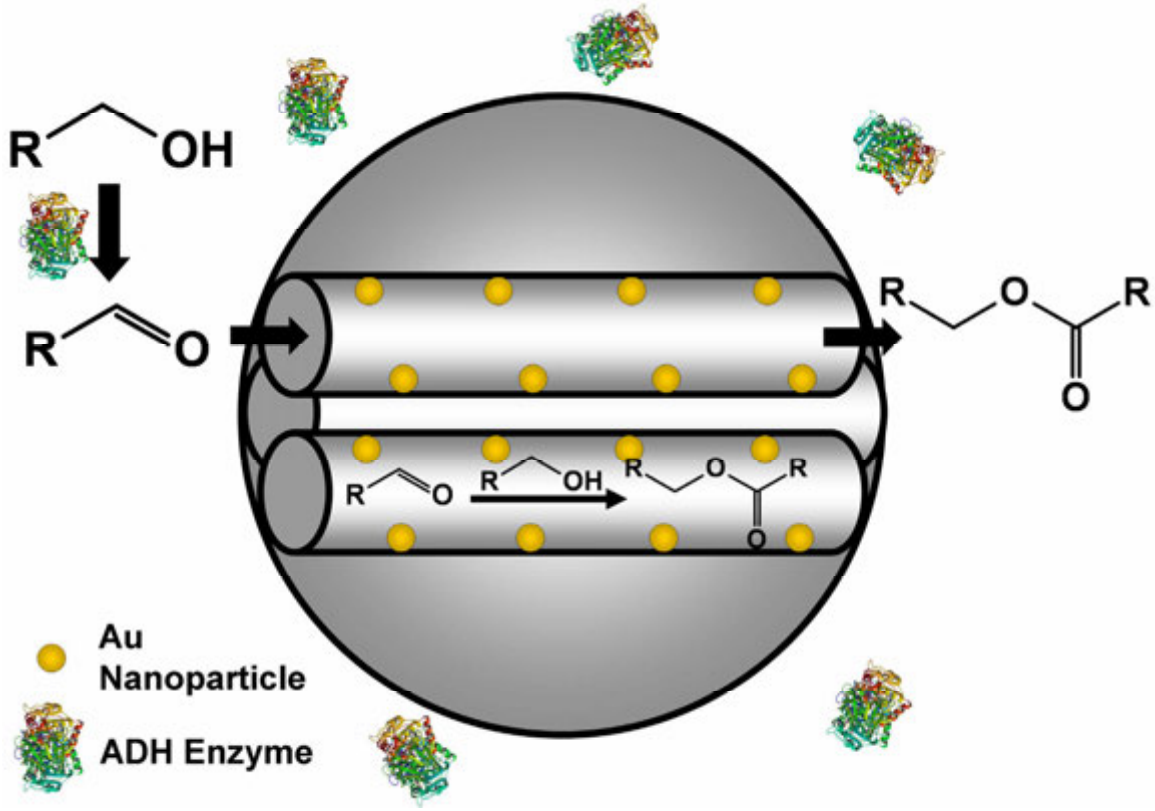

Figure 1. Schematic representation of the ADH enzyme and Au-MSN co-catalyst system

2. Materials and Methods

2.1 Reagents and materials

Pluronic 104 (P104) was a gift courtesy of BASF. Other reagents were purchased from Sigma-Aldrich, Inc. All chemicals were used as received without further purification.

2.2 Synthesis of MSN

The MSN was prepared via our previously reported method.[18] Typically, 7.0 g P104 surfactant was dissolved in 273.0 g HCl solution (1.6 M) and stirred at 55 °C for 1 hr, followed by a rapid addition of 10.64 g tetramethylorthosilicate. After continuous stirring at 55 °C for 24 hr, the mixture was transferred into a Teflon-lined, high-pressure autoclave for hydrothermal treatment at 150 °C for 24 hr. The solid product was filtered and washed with copious amounts of water and methanol, and dried under vacuum for 24 hr. Surfactant was removed by calcination at 550 °C for 6 hr.

2.3 Synthesis of $Au(en)_2Cl_3$

$Au(en)_2Cl_3$ was synthesized based on a literature procedure.[19] Ethylenediamine (6.7 mmol) was added to a 10 ml aqueous solution of $HAuCl_4 \cdot 3H_2O$ (2.54 mmol). The solution was stirred at room temperature for 30 min. Anhydrous ethanol (70 mL) was added into the solution to form a light-yellow precipitate. The solid product was filtered and washed with ethanol and dried under vacuum for 24 hr.

2.4 Synthesis of Au-MSN

Au-MSN was prepared by our previously reported method.[20] In brief, 0.372 g (0.085 mmol) $Au(en)_2Cl_3$ was dissolved in 150 ml deionized water. The pH value of this solution was adjusted to 10.0 using NaOH. Subsequently, 2.0 g of surfactant removed MSN was added. The pH value of the mixture immediately dropped to around 6 and was tuned to reach a pH of 9.0 with NaOH. The mixture was stirred at room temperature for 2 hr. The solid product was isolated by filtration, washed with water, and dried under vacuum. This process was performed for three cycles to reach a desirable loading of $Au(en)_2Cl_3$. Finally, Au-MSN was generated by the reduction of $Au(en)_2Cl_3$ loaded MSN, which was carried out under H_2 flow at 200 °C for 5 hr.

2.5 Enzymatic assay of alcohol dehydrogenase

The enzymatic reactivity of alcohol dehydrogenase enzyme catalyzed conversion of allyl alcohol to acrolein was determined based on the method of Vallee and Hoch.[21] Typically, an alcohol dehydrogenase enzyme stock solution was prepared by dissolving the enzyme in a phosphate buffer (10 mM, pH 7.5) to reach an enzyme concentration of 1 mg ml^{-1}. The enzyme stock solution was further diluted to the enzyme working solution, with an enzyme concentration of 0.2 mg ml^{-1} in sodium phosphate buffer (10 mM with 0.1% w/v Bovine Serum Albumin). A 15 mM solution of β-Nicotinamide adenine dinucleotide (NAD^+) was prepared by dissolving NAD^+ (0.5 g) in deionized water (50 ml). In a 96-well plate, 50 µl allyl alcohol, 70 µl NAD^+ solution and 10 µl enzyme working solution was pipetted and sodium pyrophosphate buffer solution (50 mM, pH 8.8) was added until a total volume of 250 µl was reached. The mixture was immediately measured for UV-vis absorbance at 340 nm on a microplate reader (Biotek Synergy MX).

To investigate the effect of Au-MSN on enzyme denaturation, 30 µl Au-MSN suspension (2.5 mg ml^{-1} in 10 mM sodium pyrophosphate buffer) was mixed with enzyme working solution at different weight ratios (18:1, 12:1 and 9:1). The mixture was then stirred for 30 min and centrifuged at 800 rpm for 4 min. 10 µl of supernatant was used in an enzyme assay test instead of the enzyme working solution.

2.6 Aerobic oxidative esterification of allyl alcohol and acrolein by Au-MSN

A mixture of allyl alcohol (171 mg, 3 mmol), acrolein (168 mg, 3 mmol) and Au-MSN catalyst (0.015 mmol, 0.5 mol% Au) in 0.6 ml sodium pyrophosphate buffer solution (50 mM, pH 8.8) was prepared in a reaction vial. Anisole (20.0 mg, 0.184 mmol) was added as an internal standard. The vial was then purged and balloon filled with pure oxygen. The reaction mixture was stirred at room temperature for various reaction time periods (1 hr, 3 hr, 6 hr, 12 hr and 24 hr), followed by toluene extractions (0.2 ml × 3). The extractions were analyzed using GC-MS.

2.7 Aerobic oxidative esterification of allyl alcohol by ADH and Au-MSN

A mixture of allyl alcohol (854 mg, 15 mmol), NAD^+ (100 mg, 0.15 mmol), alcohol dehydrogenase enzyme (3 mg), bovine serum albumin (0.5 mg) and Au-MSN catalyst (0.015 mmol, 0.5 mol% Au) in 4 ml sodium pyrophosphate buffer solution (50 mM, pH 8.8) was prepared in a reaction vial. Anisole (20.0 mg, 0.184 mmol) was added as an internal standard. The vial was then purged and balloon filled with pure oxygen. The

reaction mixture was stirred at room temperature for 24 hr, followed by toluene extractions (0.5 ml × 3). The extraction solution was analyzed using GC-MS.

2.8 Characterization methods

The X-ray powder diffraction (XRD) patterns were measured by Rigaku Ultima IV X-Ray Diffractometer using a Cu Kα radiation source. The low angle diffraction was measured with a 2θ angle ranging from 0.8 to 10 degrees to evaluate the long-range order of the materials. The high angle diffraction pattern was obtained with a 2θ angle ranging from 10 to 90 degrees to investigate the degree of crystallinity of Au inside the mesopores of MSN. The surface analysis was performed by nitrogen sorption isotherms on a Micromeritics Tristar 3000 analyzer. The surface area was calculated by the Brunauer-Emmett-Teller (BET) method. The pore size distribution was calculated by the Barrett-Joyner-Halenda (BJH) method using the desorption branch of isotherm. Transmission electron microscopy (TEM) was completed on a Tecnai G^2 F20 electron microscope operated at 200 kV. The metal content loading of the Au-MSN was quantified by a Hewlett-Packard 4500 ICP-MS. The ester yield was quantified with an Agilent 6890 gas chromatograph coupled to an accurate mass time-of-flight (TOF) mass spectrometer.

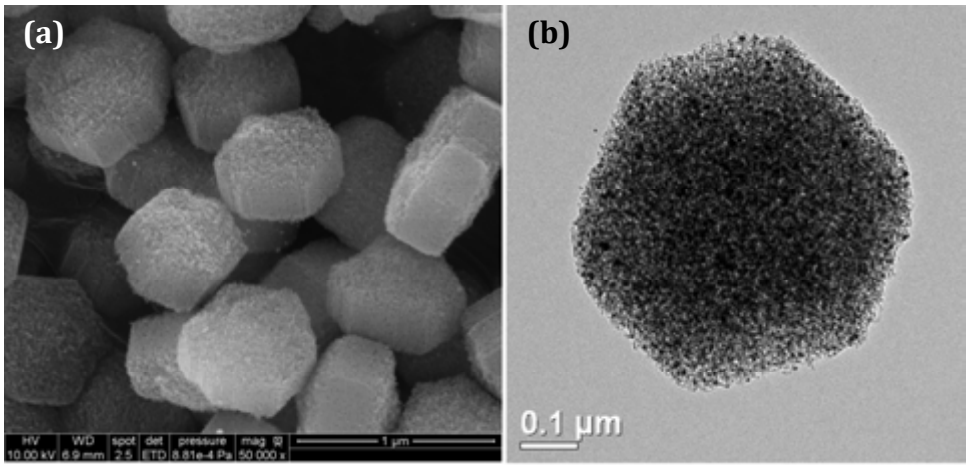

Figure 2. (a) SEM image and **(b)** TEM image of Au-MSN

3. Results and Discussion

3.1. MSN characterization

Full characterizations of Au-MSN were performed by various techniques. The synthesized material exhibited typical type IV isotherm behavior with an approximate

BET surface area of 294 m^2 g^{-1} and a pore volume of 0.87 cm^3 g^{-1} (Figure 3, Table 1). Although both values decreased after Au loading, both are still sufficient for mass transport and catalysis. BJH pore size distributions showed that a negligible decrease in pore diameters was observed for the materials after Au impregnation. These results suggest that the Au nanoparticles formed by *in situ* reduction are accessible and do not block the mesopore channels. The powder X-ray diffraction patterns are shown in Figure 4. The low angle pattern indicated that the 2D hexagonal mesopore structure of MSN remained intact after Au loading. The high angle pattern demonstrated the presence of crystalline Au on the MSN, as indicated by the good match with the standard pattern of crystalline Au.[22] In compliance with the X-ray diffraction pattern, TEM image of Au-MSN also indicates a successful loading of Au nanoparticles, represented by the dark spots scattered all over the mesoporous silica nanoparticles in Figure 2b, suggesting a homogeneous distribution with no apparent aggregation. EDX results also confirmed the elemental existence of Au. The actual loading of Au content (12.4 wt%) was determined by ICP-MS analysis. Scanning electron microscopy (SEM) showed that Au-MSN nanoparticles have consistent morphology and particle sizes at around 600 nm (Figure 2a).

Table 1. Summary of physical properties of MSN and Au-MSN

Material	S_{BET} (m^2 g^{-1})	Pore Volume (cm^3 g^{-1})	Pore Size (nm)	Au Loading wt%
MSN	**385**	**1.04**	**11.0**	**0**
Au-MSN	**294**	**0.83**	**10.7**	**12.4**

[a.] Specific surface area (S_{BET}), pore volume and pore diameter were obtained from N_2 sorption analysis. S_{BET} was calculated by BET method and the pore diameter was calculated by BJH method. [b.] The weight percentage (wt%) of Au content on Au-MSN was determined by ICP-MS analysis.

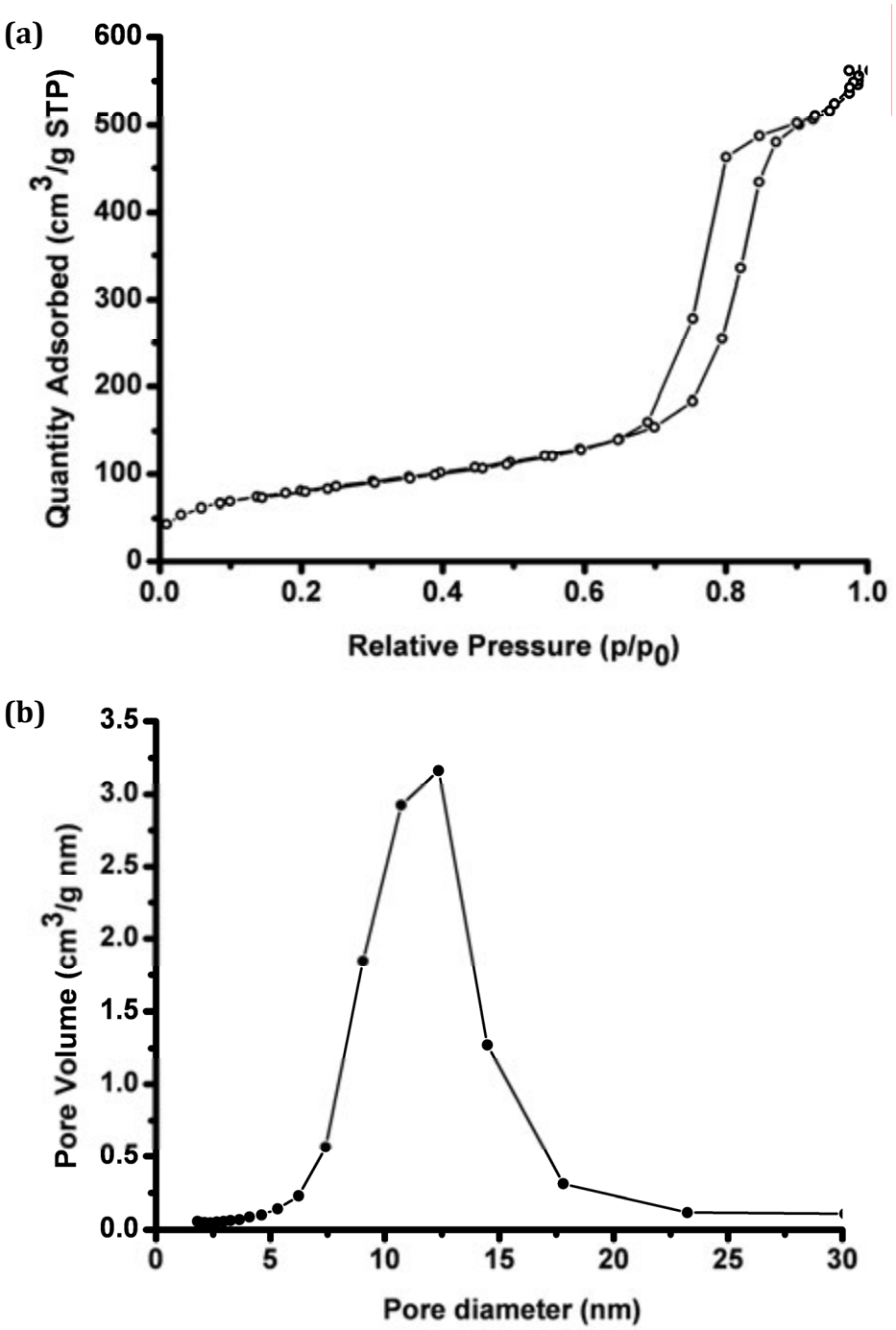

Figure 3. (a) N_2 adsorption/desorption isotherms and **(b)** pore diameter distribution of Au-MSN

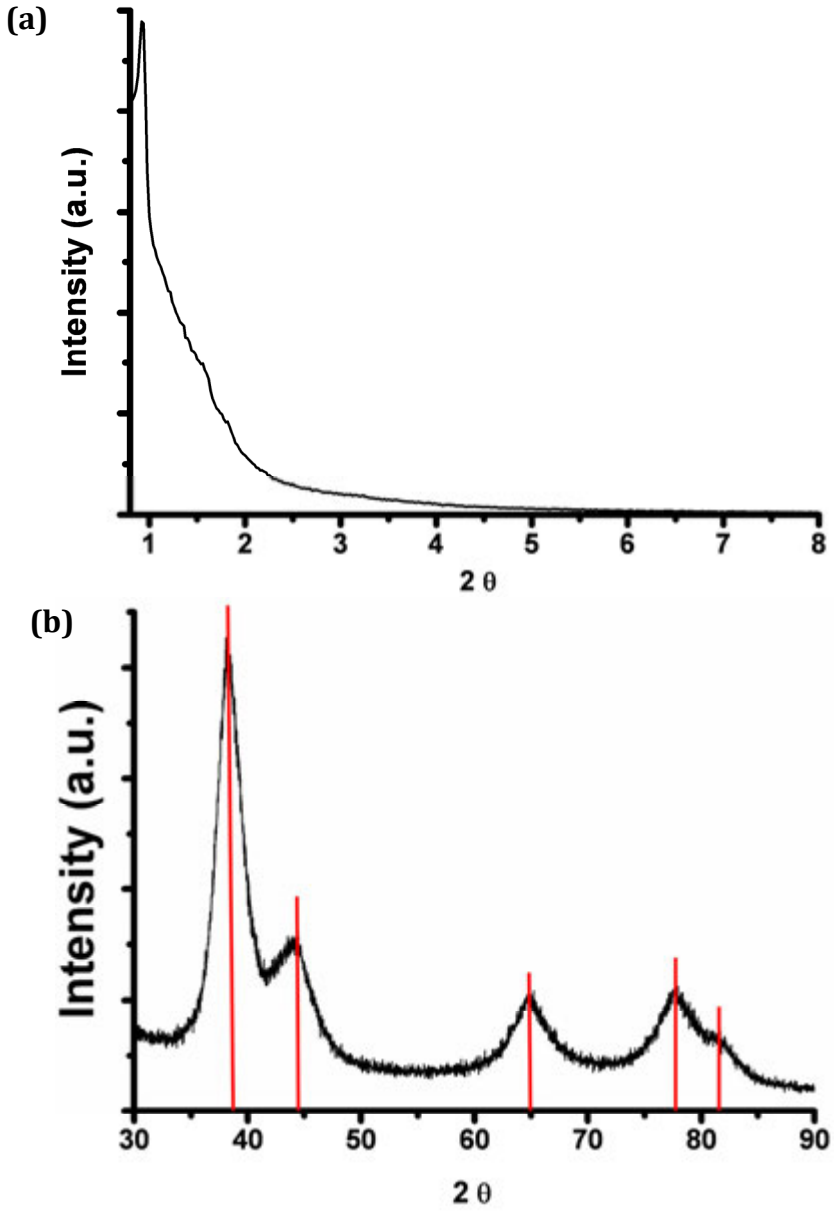

Figure 4. (a) Low-angle and **(b)** high-angle powder X-ray diffraction patterns of Au-MSN. The red lines indicate the standard pattern of crystalline gold.

3.2. ADH enzyme catalyzed alcohol oxidation

The enzymatic activity and catalytic efficiency of ADH on the allyl alcohol oxidation reaction was examined by means of ADH enzyme assay tests, as described in the experimental section. The enzyme assay test is based on the different UV-vis absorption behaviors of NAD^+ and its reduced form, NADH, where NADH has a strong absorption of UV-vis light at the wavelength of 340 nm while light absorbance at the same wavelength is very weak for NAD^+. In an ADH enzyme catalyzed alcohol oxidation

reaction, the production of NADH is proportional to the consumption of NAD^+ and the generation of aldehyde.[23, 24] Therefore, we can monitor the reaction kinetics by measuring the UV-vis light absorbance values.

We investigated the effect of allyl alcohol concentration, NAD^+ loading amount and ADH enzyme concentration on the enzyme activity separately. To evaluate the allyl alcohol concentration effect, the enzyme assay tests were performed in a 96-well plate, NAD^+ solution (15 mM, 70 µl), enzyme working solution (0.2 mg ml^{-1}, 5 µl) and various amount of allyl alcohol (37.5 µl, 50 µl and 62.5 µl) was pipetted and sodium pyrophosphate buffer solution (50 mM) was added until a total volume of 250 µl was reached. As shown in Figure 5a, ADH enzyme activity was depressed upon increased allyl alcohol concentrations, which is in accordance with the report of Bradbury and Christensen that allyl alcohol inhibits ADH enzyme activity,[25] although allyl alcohol itself is an ADH enzyme substrate with high specificity.[17] We also determined that this inhibition effect can be alleviated by decreasing the allyl alcohol concentration below 25% (v/v).

Similar assay tests were carried out to examine the effect of NAD^+ amount on the enzymatic reaction kinetics. In a 96-well plate, allyl alcohol (25 µl), enzyme working solution (0.2 mg ml^{-1}, 5 µl) and various amounts of NAD^+ solution (15 mM, 10 µl, 20 µl and 50 µl) was pipetted and sodium pyrophosphate buffer solution (50 mM) was added until a total volume of 250 µl was reached. It is interesting to note that the production of NADH can be tuned by the amount of NAD^+ substrate (Figure 5b), where the introduction of more NAD^+ led to the conversion of more NADH, as well as a higher yield of acrolein (aldehyde).

In addition, the reaction kinetics is closely associated to the enzyme concentrations. In a 96-well plate, allyl alcohol (36 µl), NAD^+ solution (15 mM, 50 µl) and various amount of enzyme working solution (0.2 mg ml^{-1}, 2 µl, 5 µl and 10 µl) was pipetted and sodium pyrophosphate buffer solution (50 mM) was added until a total volume of 250 µl was reached. As illustrated in Figure 5c, higher ADH enzyme concentration was able to catalyze the alcohol oxidation reaction at a faster rate than that of lower ADH enzyme concentration. In summary, we expect that these fundamental studies on the factors that affect ADH enzymatic reaction kinetics would provide basic guidelines when designing other enzyme involved catalysts.

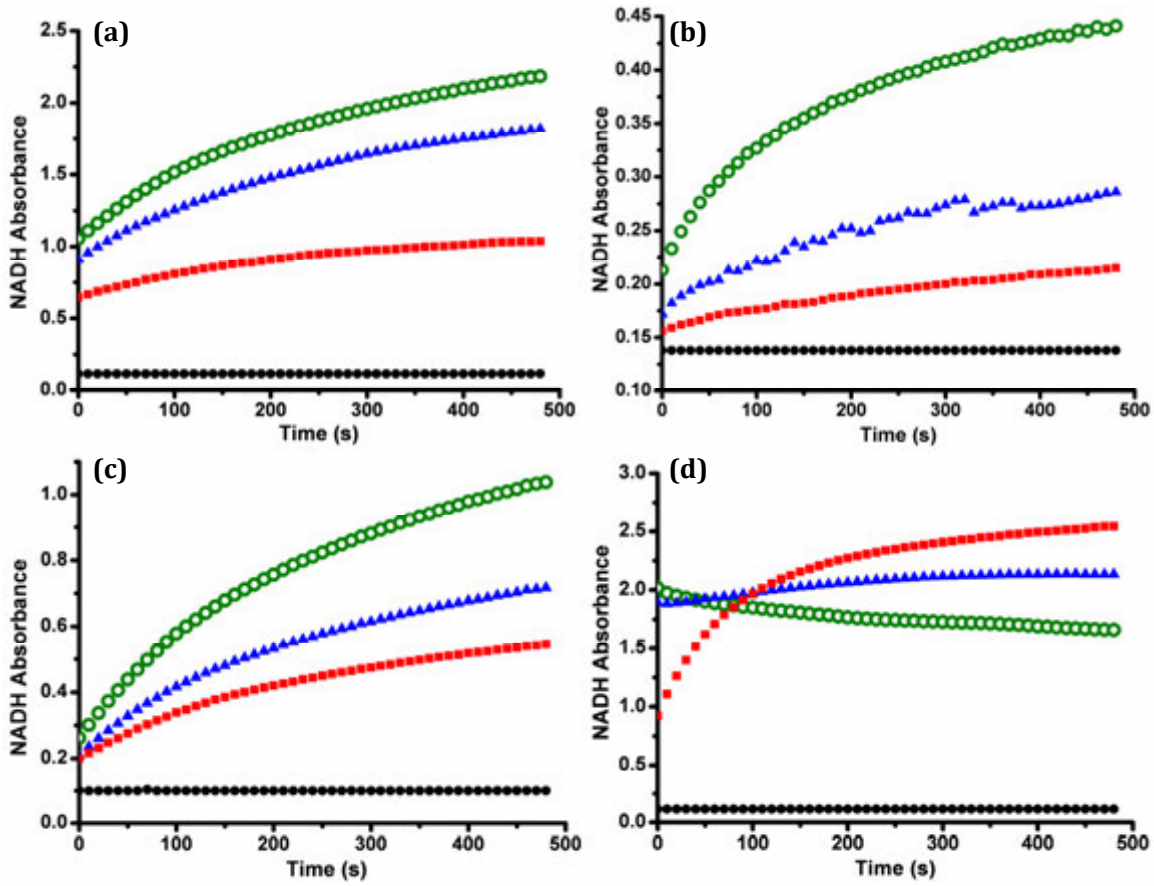

Figure 5. ADH enzyme assay test results at various conditions, **(a)** various allyl alcohol concentrations (v/v), 15% (green circle), 20% (blue triangle), 25% (red square) and blank (black dot). **(b)** Various amounts of NAD^+, 0.75 μmol (green circle), 0.30 μmol (blue triangle), 0.15 μmol (red square) and blank (black dot). **(c)** Various ADH enzyme concentrations, 8 μg ml^{-1} (green circle), 4 μg ml^{-1} (blue triangle), 1.6 μg ml^{-1} (red square) and blank (black dot). **(d)** Various ADH enzyme to Au-MSN weight ratios, 1:18 (green circle), 1:12 (blue triangle), 1:9 (red square) and blank (black dot).

Complementary to the enzyme assay tests, a millimole-scale quantitative analysis of ADH enzyme catalyzed allyl alcohol oxidation reaction was explored to provide direct evidence of aldehyde production. A reaction mixture (1 ml, 50 mM sodium pyrophosphate buffer) comprising allyl alcohol (171 mg), NAD^+ (20 mg) and ADH enzyme (0.6 mg) was prepared and allowed to stir at room temperature for 1 hr. Acrolein (aldehyde) was then extracted from the mixture with toluene and analyzed by GC-MS. Consistent with data obtained from enzyme assay tests, ADH enzyme exhibited high activity and selectivity for the allyl alcohol oxidation reaction, where a 95% acrolein yield

was obtained. These results suggest that ADH enzyme is capable of oxidizing alcohol in fast kinetics with high specificity.

The fact that MSN as well as Au nanoparticles would undermine the enzymatic activity through a non-specific adsorption effect when incubated with enzymes has been reported by several research groups.[26,27] Therefore, it is important to analyze the influence of Au-MSN on the ADH activity before combining the enzyme and Au-MSN in one system. As detailed in the experimental section, ADH enzyme was incubated with Au-MSN at three different weight ratios (1:9, 1:12 and 1:18) for 30 min at room temperature. The supernatant was then used for the assay tests. As shown in Figure 5d, the ADH activity was depressed dramatically upon incubation with Au-MSN at a weight ratio of 1:18 presumably due to enzyme denaturation. However, adjusting the enzyme to Au-MSN weight ratio to 1:9 can diminish the detrimental influence of the inorganic catalyst. This data demonstrated that the enzyme and Au-MSN ratio is another factor that would impact the performance of the co-catalyst system.

3.3. Au-MSN catalyzed aldehyde esterification

To investigate the catalytic efficiency of Au-MSN on the acrolein to acrylate ester transformation, the aerobic oxidative esterification of allyl alcohol and acrolein was carried out in sodium phosphate buffer solution using Au-MSN as a catalyst at room temperature. A control experiment showed that MSN without Au loading was catalytically inactive in this reaction. As illustrated in Figure 6, we can clearly observe that the ester yield increased over reaction time, from 7.2% at 1 hr to 34.8% at 24 hr (0.5 mol% catalyst, blue triangle). The reaction kinetic study also suggests that the reaction rate slightly decreased over time. Moreover, the amount of Au-MSN catalyst affected the ester productivity, where 34.8% of ester yield was obtained with a 0.5 mol% loading of Au-MSN, as opposed to only a 6.6% ester yield when a 0.02 mol% loading of Au-MSN was introduced over the same period of 24 hr.

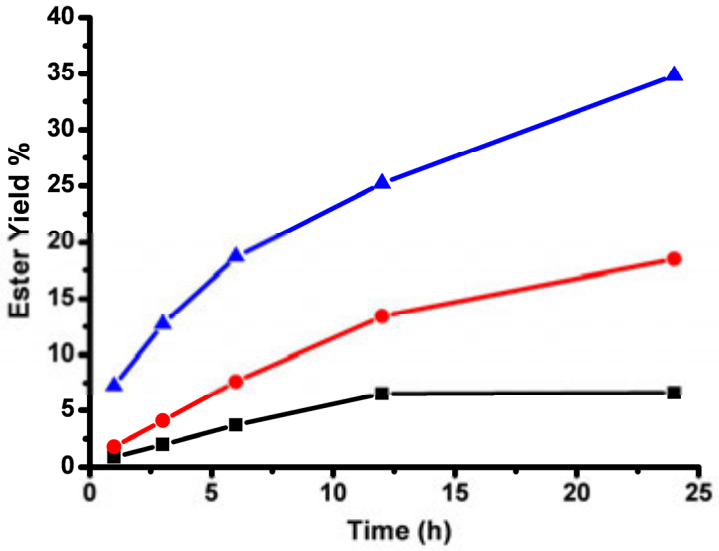

Figure 6. Production of allyl acrylate ester versus time using 0.02 mol% Au-MSN (black square), 0.08 mol% Au-MSN (red dot), and 0.5 mol% Au-MSN (blue triangle)

Table 2. Catalytic performance of the co-catalyst system for allyl alcohol oxidative esterification under various conditions.

Trial	NAD^+ (mmol)	ADH (mg)	Au-MSN (mg)	Ester Yield (%)
1	**0.3**	**3**	**0**	**n.d.**
2	**0.3**	**0**	**24**	**2.2**
3	**0.3**	**3**	**24**	**26.1**
4	**0.15**	**3**	**24**	**9.7**
5	**0.3**	**2**	**12**	**n.d.**

[a.] Conditions: allyl alcohol (1 ml, 15 mmol); sodium pyrophosphate buffer solution (50 mM, pH 8.8, 4 ml); O_2 (1 atm) were consistent along all trials with various amounts of NAD^+, ADH enzyme and Au-MSN. Ester yield was determined by GC-MS. n.d. – not detectable.

3.4. One-pot aerobic alcohol oxidative esterification reaction results

Finally, to evaluate the performance of the constructed co-catalyst system on the one-pot alcohol oxidative esterification, a reaction mixture containing allyl alcohol, NAD^+, ADH enzyme and Au-MSN was prepared and stirred for 24 hr, as described in the experimental section. The resulting mixture was extracted with toluene and subsequently analyzed by GC-MS. Either ADH enzyme or Au-MSN alone exhibited very low

reactivity for ester productions (Trial 1 and 2). In contrast, an enhanced ester yield of 26.1% was measured using the ADH enzyme and Au-MSN co-catalyst system (Trial 3), which can be attributed to the tandem oxidative mechanism as we have proposed. It is also noteworthy that increasing the amount of substrate or catalyst caused elevation of the ester yield (Trial 3, 4 and 5), but the solubility issue of NAD^+ prevents further enhancement of reactivity through simply adding more NAD^+ in this experiment. Furthermore, the co-catalyst system shows comparable reactivity to a previously reported method by conducting the reaction at 85 °C, where a 17.5% yield of allyl acrylate ester was produced.[28] Therefore, this co-catalyst system served as a feasible tool for the one-pot aqueous oxidative esterification of alcohol. Further interests on metal active sites distribution, metal-support interactions and suppressing the nonspecific adsorption effect between enzyme and Au-MSN with polyethylene glycol (PEG) coating or pre-adsorbed bovine serum albumin (BSA) are still under investigation for the development of catalytic efficiency.

4. Conclusion

A co-catalyst system consisting ADH enzyme and Au-MSN has been developed for the first time and applied in the oxidative esterification of allyl alcohol. The reaction kinetics and mechanism were discussed and we have identified fundamental factors for designing similar systems. We found that our co-catalyst system revealed superior ester productivity over each catalyst alone. Furthermore, we envision that the concept of employing a biocatalyst and a supported inorganic catalyst to establish a synergic effect could extend to other reactions.

REFERENCES

1. Otera, J. *Esterification: Methods, Reactions and Applications*, Wiley-VCH: Weinheim, Germany, **2003**
2. Larock, R. C. *Comprehensive Organic Transformations: A Guide to Functional Group Preparations*, 2nd ed.; Wiley-VCH: New York, **1999,** p 1993
3. Carey, F. A.; Sundbery, R. G. *Advanced Organic Chemistry, Part B: Reactions and Synthsis*, 5th ed. Springer: New York, **2007**; p 252.
4. Sheldon, R. A.; Arends, I. W. C. E.; Dijksman, A. *Catal. Today* **2000**, 57, 157
5. Oliveira, R. L.; Kiyohara, P. K.; Rossi, L. M. *Green Chem.* **2009**, 11(9), 1366-1370
6. Miyamura, H.; Yasukawa, T.; Kobayashi, S. *Green Chem.***2010**, 12(5), 776-778
7. Hao, Y.; Chong, Y.; Li, S.; Yang, H. *J. Phys. Chem. C* **2012**, 116(11), 6512-6519
8. Costa, V. V.; Estrada, M.; Demidova, Y.; Prosvirin, I.; Kriventsov, V.; Cotta, R. F.; Fuentes, S.; Simakov, A.; Gusevskaya, E. V. *J. Catal.* **2012**, 292, 148-156
9. Brett, G. L.; Miedziak, P. J.; Dimitratos, N.; Lopez-Sanchez, J. A.; Dummer, N. F.; Tiruvalam, R.; Kiely, C. J.; Knight, D. W.; Taylor, S. H.; Morgan, D. J. *et. al. Catal. Sci. Technol*. **2012**, 2(1), 97-104
10. Marsden, C.; Taarning, E.; Hansen, D.; Johansen, L.; Klitgaard, S. K.; Egeblad, K.; Christensen, C. H. *Green Chem.*, **2008**, 10, 168-170
11. Liu, C.; Wang, J.; Meng, L. K.; Deng, Y.; Li, Y.; Lei, A. W.; *Angew. Chem. Int. Ed.* **2011**, 50, 5144-5148
12. Haruta, M.; Daté, M. *Appl. Catal. A-Gen.*, **2001**, 222, 427-437
13. Chi, Y.-S.; Lin, H.-P.; Mou, C.-Y. *Appl. Catal. A-Gen.*, **2005**, 284, 199-206
14. Boffi, A.; Cacchi, S.; Ceci, P.; Cirilli, R.; Fabrizi, G.; Prastaro, A.; Niembro, S.; Shafir, A.; Vallribera, A. *ChemCatChem* **2011**, 3(2), 347-353
15. Jørgensen, B. S.; Christiansen, S. E.; Thomsen E. M. L.; Christensen, C. H. *J. Catal.* **2007**, 251, 332.
16. Abad, A.; Corma, A.; Garcia, H. *Pure Appl. Chem.*, **2007**, 79(11), 1847-1854
17. Sealy-Lewis, H. M.; Fairhurst, V. *Microbiology* **1995**, 141(9), 2295-300
18. Kim, T.-W.; Slowing, I. I.; Chung, P.-W.; Lin, V. S.-Y. *ACS Nano* **2010**, 5, 360
19. Zhu, H.; Liang, C.; Yan, W.; Overbury, S. H.; Dai, S. *J. Phys. Chem. B* **2006**, 110, 10842
20. Martin-Ortigosa, S.; Valenstein, J. S.; Sun, W.; Moeller, L.; Fang, N.; Trewyn, B. G.; Lin, V. S.-Y.; Wang, K. *Small* **2012**, 8(3), 413-422

21. Vallee, B. L.; Hoch F. *Proc. Nat. Acad. Sci. USA* **1955**, 41, 327-328

22. Jette E. R.; Foote F. *J. Chem. Phys.* **1935**, 3, 605-616

23. Léric, H.; Kaplan, J.; Broun, G. *Clin. Chim. Acta.*, **1970**, 29, 523-528

24. Lim, H. H.; Buttery, J. E. *Clin. Chim. Acta.*, **1977**, 75, 9-12

25. Bradbury, S. P.; Christensen, G. M. *Environ. Toxicol. Chem.*, **1991**, 10, 1155-1160

26. Hong, R.; Fischer, N. O.; Verma, A.; Goodman, C. M.; Emrick, T.; Rotello, V. M. *J. Am. Chem. Soc.* **2004**, 126, 739-743

27. Taluja, A.; Bae, Y. H. *Pharm. Res.* **2007**, 24, 1517-1526

28. Hayashi, T.; Inagaki, T.; Itayama, N.; Baba, H. *Catal. Today* **2006**, 117(1-3), 210-213

CHAPTER 6. LUCIFERASE AND LUCIFERIN CO-IMMOBILIZED MESOPOROUS SILICA NANOPARTICLE MATERIALS FOR INTRACELLULAR BIOCATALYSIS

A paper published in ***Journal of American Chemical Society***, **2011**, *133*, 18554-18557

Xiaoxing Sun, Yannan Zhao, Victor S.-Y. Lin, Igor I. Slowing, and Brian G. Trewyn

ABSTRACT

We report a gold nanoparticle-capped mesoporous silica nanoparticle (Au-MSN) platform for intracellular co-delivery of an enzyme and a substrate with retention of bioactivity. As a proof-of-concept demonstration, Au-MSNs are shown to release luciferin from the interior pores of MSN upon gold nanoparticle uncapping in response to disulfide-reducing antioxidants and co-deliver bioactive luciferase from the PEGylated exterior surface of Au-MSN to HeLa cells. The effectiveness of luciferase-catalyzed luciferin oxidation and luminescence emission in the presence of intracellular ATP was measured by a luminometer. Overall, the chemical tailorability of the Au-MSN platform for retaining enzyme bioactivity, the ability to co-deliver enzyme and substrate, and the potential for imaging tumor growth and metastasis afforded by intracellular ATP- and glutathione-dependent bioluminescence make this platform appealing for intracellular controlled catalysis and tumor imaging.

ARTICLE

The intracellular delivery and controlled release of multiple biogenic molecules, such as genes, enzymes, proteins, and other molecules of pharmaceutical interest,[1-5] provides a powerful tool for therapeutics and fundamental study of biological processes such as enzyme-catalyzed reactions. While intracellular enzyme delivery has been studied using nanocarriers,[2-4] the co-delivery of enzyme and substrate for enzymatic reactions mediated by intracellular factors has not yet been reported. Modulation of enzymatic reactions by cellular factors provides a potent means to gain information of cellular processes, such as signal transduction, DNA replication and metabolism. These cellular factors can be considered to be biological markers and therapeutic targets for disease diagnosis and treatment.[6-8] For example, one of the key metabolites involved in maintaining a reduced intracellular redox milieu is the tripeptide, glutathione (GSH).[9] GSH has long been

suggested to be part of signaling cascades transuding environmental signals to the nucleus and its elevated concentration in many types of tumors is often associated with an increased resistance to chemo- and radiotherapy.[8] Likewise, as biological energy, ATP is involved in a multitude of important intracellular physiological processes, such as protein metabolism and cell apoptosis, the level of which is a measure of tumor cell viability and growth.[6] Therefore, intracellular co-delivery of enzymes and substrates for cellular factor (*e.g.* GSH and ATP)-mediated enzymatic reactions would not only afford novel biocatalysis inside live cells but also find application in monitoring tumor growth and metastasis. Two major challenges, however, are 1) the design of nanomaterials for intracellular controlled release of multiple biogenic species with preserved bioactivity, and 2) the development of methods for imaging and quantification of cellular factor-mediated catalytic reactions.

Recently, mesoporous silica nanoparticles (MSNs) demonstrated to be excellent candidates as vehicles for co-delivery applications,[10,11] owing to the co-existence of both interior pore and exterior particle surfaces for loading various guest molecules. This unique feature provides the possibility of using MSN for controlled release and co-delivery of enzymes and substrates for intracellular enzymatic reactions. With respect to the challenge of imaging and quantification, most studies on nanoparticle-based tumor imaging have focused on their cellular uptake and have relied heavily on fluorescence readout, which cannot provide biologically relevant information on cellular processes. Bioluminescence has gained favor in the last decade as an attractive approach for tumor imaging.[12-17] This technique is based on light emission by the luciferase-catalyzed oxidation of the luciferin substrate, which occurs in an ATP-dependent manner.[18,19] A vast number of experiments have been carried out examining tumor growth and the effect of therapeutics with the use of tumor cell lines that have been genetically engineered to produce luciferase.[12-17] However, the detection of photons is dependent on the circulatory half-life of injected luciferin substrate and its perfusion into the tumor.[20] The fast elimination of luciferin from the circulation makes utilizing it in many clinical applications challenging.[20] Both the sophisticated gene engineering and the short circulatory half-life of luciferin call for novel nanomaterials for intracellular co-delivery of luciferase and luciferin, which would offer additional advantage of improving tumor uptake via the enhanced permeability and retention (EPR) effect.[21]

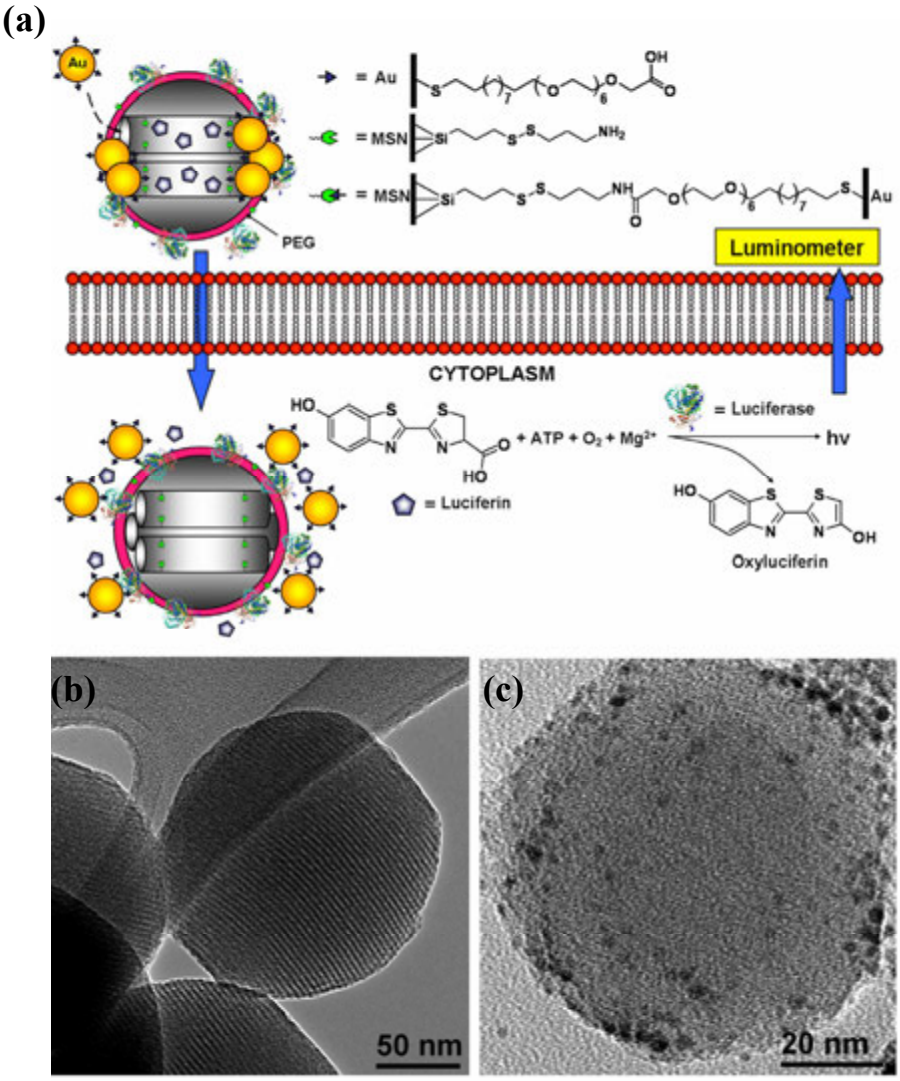

Figure 1. (a) Schematic representation of gold nanoparticle-capped mesoporous silica nanoparticles (Au-MSNs) for intracellular co-delivery of luciferase and luciferin. Transmission electron micrographs are shown in (b) PEGlyated linker-MSN and (c) luciferin-loaded Au-MSN. High magnification image of luciferin-loaded Au-MSN is shown in Figure S3d in the SI.

Herein, we report the development of a gold nanoparticle-capped MSN (Au-MSN) system and investigate the intracellular co-delivery of luciferase and luciferin, as a model enzyme and substrate pair. As depicted in Figure 1a, luciferin is loaded in the mesopores of MSN and encapsulated with disulfide-linked gold nanoparticles that physically block luciferin from leaching out. Luciferase is physisorbed to the PEGylated external surface of Au-MSN through electrostatic interactions as previously

demonstrated.[22] Luciferin molecules trapped inside the pores are released upon uncapping by intracellular disulfide-reducing antioxidants such as GSH or cysteine, or the introduction of dithiothreitol (DTT).[23] The released luciferin is in turn converted by co-delivered luciferase to oxyluciferin in presence of intracellular ATP and co-factor Mg^{2+}, along with the release of energy in the form of photons, measurable with a luminometer.

We first synthesized 3-(propyldisulfanyl)ethylamine (0.9 mmol g^{-1}) functionalized mesoporous silica nanosphere (linker-MSN) material *via* a method that we previously reported.[23,24] As described in the Supporting Information (SI), the material was PEGylated by grafting 2-[methoxy(polyethylenoxy)-propyl]trimethoxysilane to yield the PEGylated (0.1 mmol g^{-1}) linker-MSN with an average particle diameter of 160 nm and an MCM-41-type channel-like mesoporous structure (BJH pore diameter = 2.5 nm) (Figure 1b).

We then functionalized the surface of the gold nanoparticles with a carboxylic acid-terminated polyethylene glycol (PEG) linker (Figure 1a) through exchange of 1-propanethiol protected gold nanoparticle[25] with PEG-functionalized thiol ligand in dichloromethane (see SI). The PEG-functionalized gold nanoparticles (PEG-AuNPs) are negatively charged (ζ-potential at -39.6 mV) in PBS (pH 7.4) with an average particle diameter of 3 nm as determined by transmission electron microscopy (TEM) shown in Figure S3b.

Before constructing the enzyme-substrate Au-MSN system, the influence of MSN and Au NP on the enzymatic activity of luciferase was analyzed by means of a luciferase activity assay.[26,27] As presented in Figure S4, the luciferase activity is depressed dramatically when incubated with linker-MSNs and 1-propanethiol stabilized gold nanoparticles, with activities of ~20% and below 15%, respectively, after only 1 h incubation. However, nearly 75% and ~ 63% of luciferase activity were observed after 3 h of contact with PEGylated linker-MSNs and PEG-Au NPs, respectively. The enzymatic activity of luciferase was also found to be dependent on the incubation time. A slight decrease in luciferase activity was found when the incubation time increased from 3 to 24 h, in which nearly 60% and ~62% of activity were observed for PEGylated linker-MSNs and PEG-Au NPs, respectively. These data demonstrated that surface PEGylation plays a crucial role in improving the biocompatibility of MSN and Au NP for the retention of enzyme bioactivity, which is consistent with other literature reports.[22,28]

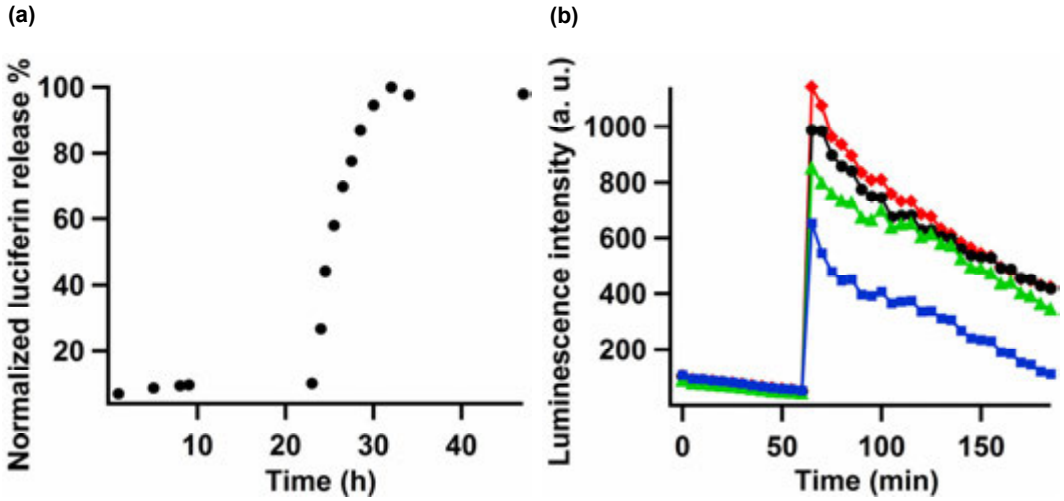

Figure 2. (a) Cumulative release of luciferin from luciferin-loaded Au-MSN suspension (1 mg mL^{-1}) after addition of 1 mM dithiothreitol (DTT) at 23 h. (b) Resultant luminescence from luciferase-luciferin Au-MSN suspension (1 mg mL^{-1}) in presence of ATP (80 μM) and Mg^{2+} (8 mM) after addition of 0.1 (blue), 0.5 (green), 1 (red) and 10 (black) mM DTT at 60 min.

Having demonstrated the surface biocompatibility of the materials, we utilized the Au-MSN platform to adsorb and encapsulate the enzymatic substrate, luciferin. To do so, the mesopores of PEGylated linker-MSN (25 mg) were loaded with luciferin (33 μM) in PBS buffer (pH 7.4), then capped with PEG-Au NPs (25 mg) through amide bond formation between the carboxylic acid groups of PEG-Au NP and amino groups of PEGylated linker-MSN (Figure 1a), giving rise to the desired luciferin-loaded Au-MSN (Figure 1c). The loading of luciferin was determined to be 13.1 μmol g^{-1} by fluorescence emission spectroscopy (see SI).

Transmission electron microscopy (TEM) imaging provides visual evidence on the mesopore capping with PEG-Au NPs. Figure 1b and 1c shows the TEM image of PEGylated linker-MSN before and after capping with PEG-AuNPs. In the case of the uncapped MSN (Figure 1b), the hexagonally packed mesoporous channels are clearly visable. In contrast, the TEM image of luciferin-loaded Au-MSN (Figure 1c) shows dark spots on MSN surface, representing the attachment of gold nanoparticles on the exterior surface of MSN.

To determine if the release of luciferin from the luciferin-loaded Au-MSN could be induced by disulfide cleavage as desired for intracellular controlled release,

luciferin-loaded Au-MSN (1 mg mL^{-1}) was suspended in PBS buffer (pH 7.4) for 23 h before addition of 1 mM DTT. As shown in Figure 2a, the Au-MSN drug delivery system exhibited less than 5.0% of drug release in PBS buffer over of the initial 23 h period. The result suggests a good capping efficiency of the gold nanoparticles for encapsulation of the luciferin molecules against leaching. Addition of disulfide-reducing molecules, DTT (1 mM) triggered the release of the mesopore-entrapped luciferin. The rate of luciferin release slightly decreased over time until reaching 100% of the total cumulative release (1.44 μmol g^{-1}) in 8 h. In addition, the controlled release of luciferin mediated by the Au-MSN system would offer the advantage of improving the circulatory half-life of luciferin and also promote tumor uptake via EPR effect, as required in various *in vitro* and *in vivo* luminescence assays. In addition, the disulfide linkage design renders the release of luciferin predominately inside the cells.[9,23,24]

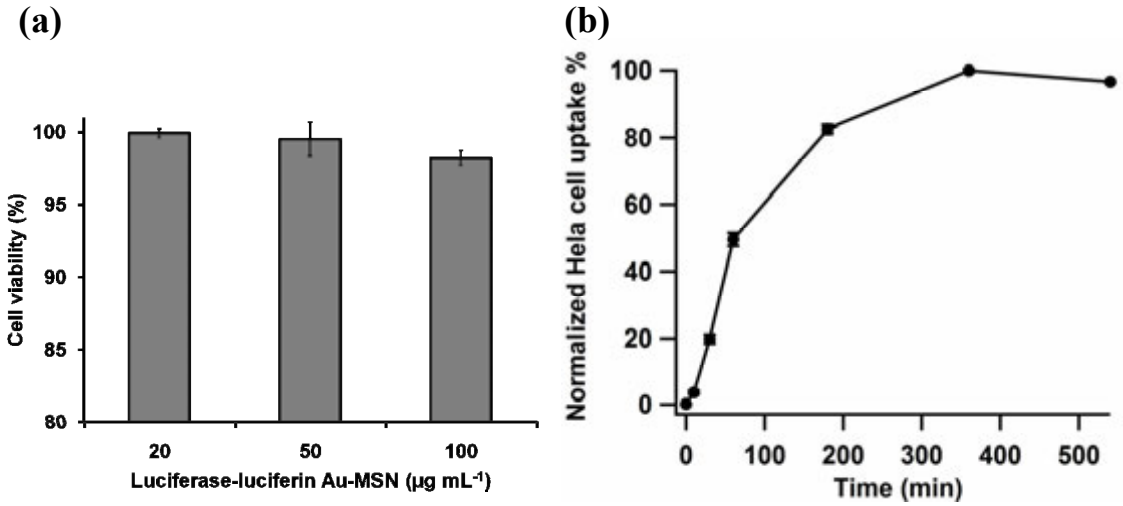

Figure 3. (a) Cytotoxicity study of Hela cells (4×10^5 cells mL^{-1}) after 24 h incubation with different concentrations (20, 50, 100 μg ml^{-1}) of luciferase-luciferin Au-MSN suspensions. (b) Endocytosis kinetics measurement of Hela cells incubated with 50 μg ml^{-1} luciferase-luciferin FITC-Au-MSNs. The cellular uptake percentage at each time point was normalized to that at 6 h of contact (63% FITC-positive cells).

The most advantageous feature of this Au-MSN platform is the potential to deliver different biogenic species simultaneously in a controlled fashion. To construct the enzyme-substrate co-delivery system, luciferase was immobilized on the external surface of Au-MSNs by incubating luciferin-loaded Au-MSNs (1 mg ml^{-1}) with luciferase (1 mg

ml^{-1}) in PBS buffer (pH 7.4) for 2 h, followed by centrifugation and freeze drying. The loading of luciferase was measured to be 29.7 μmol g^{-1} by luciferase activity assay (see SI). This system will henceforth be referred to as luciferase-luciferin Au-MSN. To examine the applicability of this controlled release co-delivery system, DTT-stimulated luciferase-luciferin reaction was conducted *in situ*, as described in the SI. The luminescence intensity remained at background level over a period of 60 minutes before the addition of disulfide bond reducing agents, suggesting a "zero premature release" property of this system. After addition of DTT (1 mM), luciferin was released and converted to oxyluciferin in a luciferase-catalyzed light-emitting reaction. As shown in Figure 2b, the pattern of luminescence as a function of time was similar for all DTT doses (0.1, 0.5, 1 and 10 mM). The highest luminescence signal was detected in 5 minutes and gradually decayed, reaching background after approximately 180 min. The observed luminescence strongly depends on the concentration of DTT. An increase in the luminescence signal was observed with growing DTT dose up to 1 mM, suggesting a dose-dependent controlled release profile. Importantly, when 10 mM DTT was introduced to the system, the luminescence showed a 15% reduction in intensity compared to the signal triggered by 1 mM DTT, which can be attributed to the denaturation of luciferase by high DTT concentrations.[29] Hence, the effectiveness of the luciferase-luciferin reaction on the Au-MSN platform depends on the strength of the reducing environment to which it is exposed.

Prior to functional biological studies of the luciferase-luciferin Au-MSNs, it is necessary to evaluate the cellular uptake and cytotoxic effects of the material. To do so, we first assessed the cellular uptake of fluorescein isothiocyanate (FITC)-labeled luciferase-luciferin Au-MSNs (denoted as luciferase-luciferin FITC-Au-MSNs) by human cervical carcinoma (Hela) cells over time. The cells were incubated in the presence of the nanoparticles (50 μg mL^{-1}) for increasing periods of time. The percentage of cells internalizing luciferase-luciferin FITC-Au-MSNs were then monitored by flow cytometry, using the trypan blue exclusion method for quenching the fluorescence of extracellular particles.[30] As shown in Figure 3b, the percent of FITC-positive cells increased with time, reaching over 80% of total cellular uptake at 3h of contact and a plateau in approximately 6 h. Taking into account the aforementioned incubation time effect on luciferase activity (Figure S4), 3 h of contact was selected for the following biological experiments. We performed confocal fluorescence microscopy (Figure 4a-c) and TEM

(Figure 4d-f) analysis of Hela cells 3 h after treatment with 50 μg mL^{-1} of luciferase-luciferin FITC-Au-MSNs and luciferase-luciferin Au-MSNs, respectively. Indeed, the nanoparticles were easily visable inside the cells confirming uptake of the materials. Finally, the toxicity of the luciferase-luciferin Au-MSNs was assessed by Guava ViaCount cytometry assay with Hela cells. Following 24 h treatment, we observed minimal toxicity (> 95% of cell viability) at concentrations of the material as high as 100 μg ml^{-1} (Figure 3a), in consistence with the good biocompatibility of MSN[23,31] and gold nanoparticles.[32]

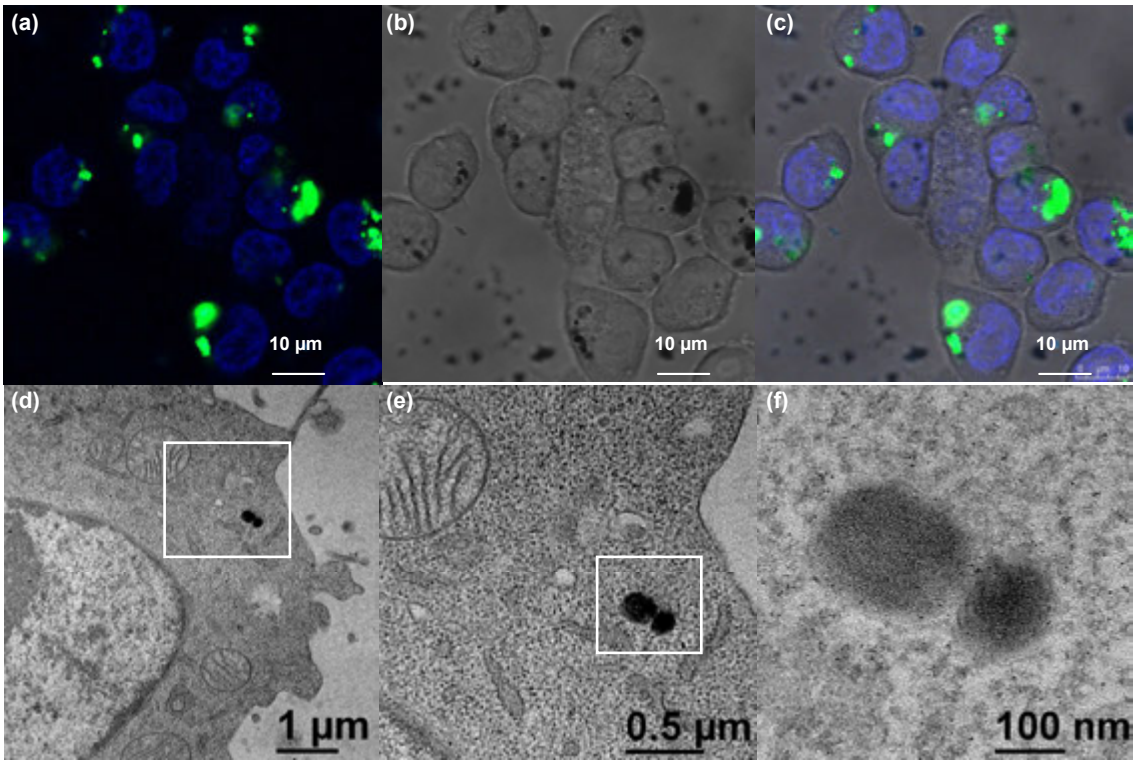

Figure 4. (a) Fluorescence confocal micrographs of Hela cells (4×10^5 cells mL^{-1}) internalized with luciferase-luciferin FITC-Au-MSN (50 μg mL^{-1}, green) for 3 h. Cell nuclei were stained with DAPI (blue). (b) Corresponding bright field image of Hela cells. (c) Fluorescence confocal and bright field merged image. (d-f) Transmission electron micrographs of Hela cells (4×10^5 cells mL^{-1}) internalized with luciferase-luciferin Au-MSN (50 μg mL^{-1}) for 3 h. Images increase in magnification from left to right.

To demonstrate that the enzyme-substrate Au-MSN system can deliver both the enzyme luciferase and the substrate luciferin for intracellular ATP- and redox

potential-mediated biocatalysis, the luciferase-luciferin Au-MSN (50 μg mL^{-1}) was internalized by Hela cells. After 3 h incubation, the intracellular luciferase-catalyzed luciferin conversion and light emission was assessed by means of intracellular luciferase activity assay (see SI). As shown in Figure 5a, a burst of luminescence was observed immediately and slowly decayed over the next 30 min. Neither the untreated Hela cells nor the cells treated with free solution of luciferase and luciferin (10- and 15-fold of loading amount, respectively) generated detectable luminescence, which is consistent with the low extracellular ATP level[33,34] and the membrane impermeability of luciferase.[35] Therefore, the observed luminescence can be attributed to the capability of our Au-MSN system for intracellular co-delivery of enzyme and substrate. Furthermore, our model system provides a means to further regulate the enzymatic reaction inside live cells. As a first demonstration of intracellular catalysis with tunability, the enzymatic reaction efficiency was increased by enhancing the intracellular reducing environment. As shown in Figure 5b, addition of 1 mM DTT after the decay of the initial intracellular disulfide-reducing antioxidant triggered luminescence and led to a 5-fold signal in 10 min compared to the highest initial luminescence, followed by a gradual decay, in accord with the *in situ* controlled release experiment shown Figure 3b. Therefore, this system renders the possibility to serve as not only a universal enzyme-substrate carrier for intracellular controlled catalysis but also a unique reporter to monitor intracellular redox-potential for the study of drug delivery, cell viability and tumor growth.

In conclusion, the present study has introduced a novel approach to intracellular co-delivery of enzyme and substrate enabling the system to be utilized in intracellular controlled catalysis. Although we have demonstrated only the co-delivery of luciferase and luciferin in this study, the concept for delivering multiple biogenic agents using such systems could also be extended to other enzymatic reactions by exchanging the enzyme and substrate pair. In addition, it has been recently observed that MSNs are able to undergo exocytosis and harvest intracellular biomolecules,[36] hence, we envision that our system could not only conduct biocatalysis inside live cells but also sequester the product out of cells for a variety of biotechnological applications.

The luciferase-luciferin Au-MSN system was designed to allow imaging and quantification of the intracellular catalysis for system optimization, which also affords a unique route toward monitoring tumor growth and metastasis by means of bioluminescence and using intracellular ATP and GSH levels as indicators. Compared

with traditional bioluminescence assays, which generally employ gene engineering and multiple luciferin injection, only one system needs to be delivered for this strategy. Rapid readouts of the luminescence arising from the nanoparticle internalization and intracellular GSH-mediated luciferase-luciferin reaction provide a unique platform for evaluating tumor development and a convenient way of monitoring response to treatments and measuring therapeutic efficacy, which is of importance for medical diagnosis, drug screen and development.

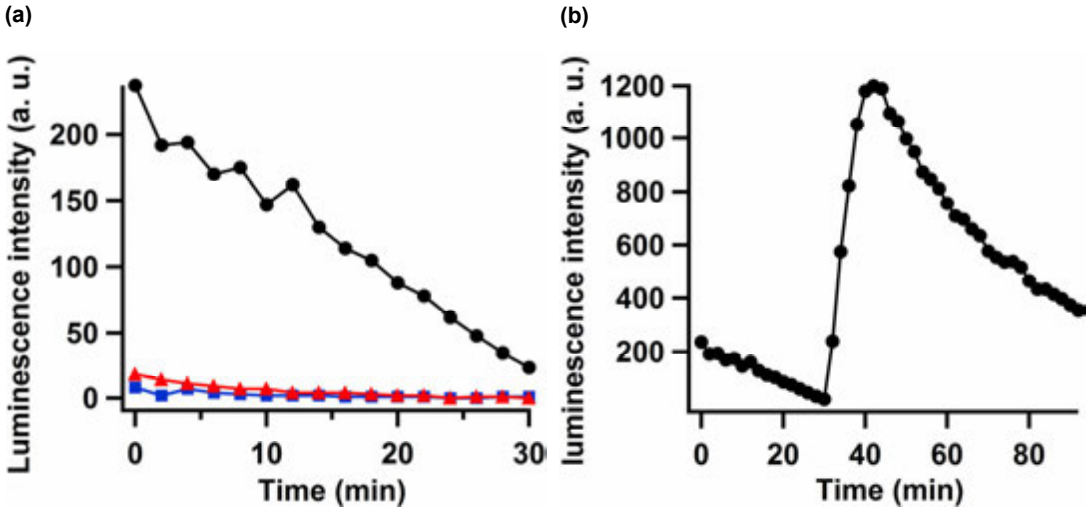

Figure 5. (a) Resultant luminescence from Hela cells (4×10^5 cells mL^{-1}) measured after 3 h incubation with luciferase-luciferin Au-MSNs (50 μg mL^{-1}, black) and with free luciferase (1 mg mL^{-1}) and luciferin (40 μM) solution (red), as compared to untreated cells (blue). (b) Observed luminescence after addition of 1 mM dithiothreitol (DTT) at 30 min to Hela cells (4×10^5 cells mL^{-1}) preincubated with luciferase-luciferin Au-MSNs (50 μg mL^{-1}) for 3 h.

ACKNOWLEDGEMENT

This work is dedicated to the memory of our dear mentor and friend, Dr. Victor Shang-Yi Lin. BGT, XS, and YZ would like to thank the U.S. National Science Foundation (CHE-0809521) and IIS would like to thank the U.S. Department of Energy, Ames Laboratory, Office of Basic Energy Sciences (Contract No. DE-AC02-07CH11358) for support to complete this project.

REFERENCES

(1) Zhao, Y.; Vivero-Escoto, J. L.; Slowing, I. I.; Trewyn, B. G.; Lin, V. S. Y. *Expert Opin. Drug Delivery* 2010, *7*, 1013-1029.

(2) Slowing, I. I.; Trewyn, B. G.; Lin, V. S. Y. *J. Am. Chem. Soc.* 2007, *129*, 8845-8849.

(3) Bale, S. S.; Kwon, S. J.; Shah, D. A.; Banerjee, A.; Dordick, J. S.; Kane, R. S. *ACS Nano* 2010, *4*, 1493-1500.

(4) Ghosh, P.; Yang, X.; Arvizo, R.; Zhu, Z.-J.; Agasti, S. S.; Mo, Z.; Rotello, V. M. *J. Am. Chem. Soc.* 2010, *132*, 2642-2645.

(5) Bale, S. S.; Kwon, S. J.; Shah, D. A.; Kane, R. S.; Dordick, J. S. *Biotechnol. Bioeng.* 2010, *107*, 1040-1047.

(6) Ahmann, F. R.; Garewal, H. S.; Schifman, R.; Celniker, A.; Rodney, S. *In Vitro Cell. Dev. B.* 1987, *23*, 474-480.

(7) Meyer, A. J.; Brach, T.; Marty, L.; Kreye, S.; Rouhier, N.; Jacquot, J.-P.; Hell, R. *Plant J.* 2007, *52*, 973-986.

(8) Balendiran, G. K.; Dabur, R.; Fraser, D. *Cell Biochem. Funct.* 2004, *22*, 343-352.

(9) Wu, G.; Fang, Y.-Z.; Yang, S.; Lupton, J. R.; Turner, N. D. *J. Nutr.* 2004, *134*, 489-492.

(10) Zhao, Y.; Trewyn, B. G.; Slowing, I. I.; Lin, V. S. Y. *J. Am. Chem. Soc.* 2009, *131*, 8398-8400.

(11) Torney, F.; Trewyn, B. G.; Lin, V. S. Y.; Wang, K. *Nat. Nanotechnol.* 2007, *2*, 295-300.

(12) Sweeney, T. J.; Mailander, V.; Tucker, A. A.; Olomu, A. B.; Zhang, W.; Cao, Y.-A.; Negrin, R. S.; Contag, C. H. *Proc. Natl. Acad. Sci. USA* 1999, *96*, 12044-12049.

(13) Jenkins, D. E.; Oei, Y.; Hornig, Y. S.; Yu, S.-F.; Dusich, J.; Purchio, T.; Contag, P. R. *Clin. Exp. Metastasis* 2003, *20*, 733-744.

(14) Liu, J. J.; Wang, W.; Dicker, D. T.; El-Deiry, W. S. *Cancer Biol. Ther.* 2005, *4*, 885-892.

(15) Chandran, S. S.; Williams, S. A.; Denmeade, S. R. *Luminescence* 2009, *24*, 35-38.

(16) Shinde, R.; Perkins, J.; Contag, C. H. *Biochemistry* 2006, *45*, 11103-11112.

(17) Edinger, M.; Sweeney, T. J.; Tucker, A. A.; Olomu, A. B.; Negrin, R. S.; Contag, C. H. *Neoplasia* 1999, *1*, 303-310.

(18) Lundin, A.; Rickardsson, A.; Thore, A. *Anal. Biochem.* 1976, *75*, 611-620.

(19) DeLuca, M.; McElroy, W. D. *Biochemistry* 1974, *13*, 921-925.

(20) Berger, F.; Paulmurugan, R.; Bhaumik, S.; Gambhir Sanjiv, S. *Eur. J. Nucl. Med. Mol. Imaging* 2008, *35*, 2275-2285.

(21) Matsumura, Y.; Maeda, H. *Cancer Res*. 1986, *46*, 6387-6392.

(22) Hong, R.; Fischer, N. O.; Verma, A.; Goodman, C. M.; Emrick, T.; Rotello, V. M. *J. Am. Chem. Soc.* 2004, *126*, 739-743.

(23) Lai, C.-Y.; Trewyn, B. G.; Jeftinija, D. M.; Jeftinija, K.; Xu, S.; Jeftinija, S.; Lin, V. S. Y. *J. Am. Chem. Soc.* 2003, *125*, 4451-4459.

(24) Giri, S.; Trewyn, B. G.; Stellmaker, M. P.; Lin, V. S. Y. *Angew. Chem. Int. Ed.* 2005, *44*, 5038-5044.

(25) Brust, M.; Walker, M.; Bethell, D.; Schiffrin, D. J.; Whyman, R. *J. Chem. Soc., Chem. Commun.* 1994, *7*, 801-802.

(26) Leach, F. R.; Webster, J. J. *Methods Enzymol.* 1986, *133*, 51-70.

(27) Lin, S.; Cohen, H. P. *Anal. Biochem.* 1968, *24*, 531-540.

(28) Taluja, A.; Bae, Y. H. *Pharm. Res.* 2007, *24*, 1517-1526.

(29) Lomakina, G. Y.; Modestova, Y. A.; Ugarova, N. N. Vestn. *Mosk. Univ., Ser. 2: Khim.* 2008, *49*, 81-85.

(30) Hed, J.; Hallden, G.; Johansson, S. G.; Larsson, P. *J. Immunol. Methods* 1987, *101*, 119-125.

(31) Slowing, I.; Trewyn, B. G.; Lin, V. S. Y. *J. Am. Chem. Soc.* 2006, *128*, 14792-14793.

(32) Arvizo, R.; Bhattacharya, R.; Mukherjee, P. *Expert Opin. Drug Delivery* 2010, *7*, 753-763.

(33) Gordon, J. L. *Biochem. J.* 1986, *233*, 309-319.

(34) Pellegatti, P.; Raffaghello, L.; Bianchi, G.; Piccardi, F.; Pistoia, V.; Di Virgilio, F. *PLoS One* 2008, *3*(7): e2599.

(35) Bayele, H. K.; Ramaswamy, C.; Wilderspin, A. F.; Srai, K. S.; Toth, I.; Florence, A. T. *J. Pharm. Sci.* 2006, *95*, 1227-1237.

(36) Slowing, I. I.; Vivero-Escoto, J. L.; Zhao, Y.; Kandel, K.; Peeraphatdit, C.; Trewyn, B. G.; Lin, V. S.-Y. *Small* 2011, *7*, 1526-1532.

APPENDIX: Supporting Information

1. Materials Syntheses

1.1 Synthesis of thiol-functionalized mesoporous silica nanoparticle (SH-MSN)

SH-MSNs were synthesized by co-condensation method that we reported previously.[1] *N*-Cetyltrimethylammonium bromide (CTAB; 1.0 g) was dissolved in 480 mL of nanopure water. NaOH (aq) (2.0 M, 3.5 ml) was introduced to the CTAB solution at 353 K. Tetraethoxysilane (TEOS, 5.0 ml, 22.4 mmol) and 3-mercaptopropyltrimethoxysilane (MPTMS, 1.0 ml, 5.4 mmol) was added dropwisely to the CTAB solution under vigorous stirring. The mixture was allowed to react for 2 h to generate a white precipitate. This solid crude product was filtered, washed with nanopure water and methanol, and dried under high vacuum to yield the as-synthesized SH-MSN. Surface thiol groups were quantified to be 1.75 mmol g^{-1} by thermogravimetric analysis (TGA).

1.2 Synthesis of PEGylated SH-MSN

As-synthesized SH-MSN (1.0 g) was suspended in anhydrous toluene (80 ml), followed by the addition of 2-[methoxy(polyethylenoxy)-propyl]trimethoxysilane (PEG-silane, 1.0 mmol). The dispersion was refluxed for 20 hours. The solid was filtered, washed with toluene and methanol and dried under high vacuum. The surfactant was removed by refluxing the material (1.0 g) in 1.0 ml of HCl (37.4%) and 100 ml of methanol for 6 h. After that, the material was washed extensively with methanol and placed under high vacuum to remove remaining solvent. Surface PEG groups were quantified to be 0.15 mmol g^{-1} by TGA.

1.3 Synthesis of PEGylated 3-(Propyldisulfanyl)propylamine-MSN (PEGylated linker-MSN)

Surfactant-free PEGylated SH-MSN (0.20 g) and 2-aldrithiol (0.75 g) was dissolved in ethanol (80 ml). The mixture was stirred at room temperature for 24 h to undergo the disulfide bond exchange reaction. The solid was collected, washed with ethanol and dried under high vacuum. The white powder was resuspended in 30 ml ethanol, followed by the dropwise addition of aminoethanethiol (0.18 g) in 20 ml ethanol solution. The mixture was stirred at room temperature for 24 h followed by centrifugation and

washing with copious ethanol to generate the PEGlyated linker-MSN. 3-(Propyldisulfanyl)propylamine groups on MSN surface were quantified to be 0.9 mmol g^{-1} by TGA.

1.4 Synthesis of 1-propanethiol stabilized gold nanoparticles (Au NPs)

The 1-propanethiol stabilized gold nanoparticles were synthesized according to a literature reported procedure.[2] $HAuCl_4$ (354.4 mg) was dissolved in H_2O (30 ml), mixed with a solution containing $N(C_8H_{17})_4Br$ (2.187 g) and toluene (80 ml). The two phase mixture was vigorously stirred for 20 min and the organic phase was collected, followed by the addition of 1-propanethiol (68.5 mg) and $NaBH_4$ solution. The solution was stirred at room temperature for 3 h and the organic phase was separated. The solvent was removed under reduced pressure and the remaining product was mixed with 400 ml ethanol. The mixture was kept at -18°C until dark brown solid precipitated. Finally, the dark brown solid was centrifuged and washed with ethanol several time to afford 1-propanethiol stabilized gold nanoparticles.

1.5 Synthesis of 2-(2-{2-[2-(2-[2-(11-mercapto-undecyloxy)-ethoxy]-ethoxy)-ethoxy]-ethoxy}-ethoxy)-ethoxy-acetic acid (thiolalkyl-EG6-COOH) stabilized gold nanoparticles (PEG-Au NPs)

The thiolalkyl-EG6-COOH stabilized gold nanoparticles were synthesized through ligand-exchange reaction according to a modified literature reported procedure.[3] 1-propanethiol stabilized gold nanoparticles (20 mg) were dissolved in 20 ml dichloromethane. Thiolalkyl-EG6-COOH (474 mg) was dissolved in dichloromethane and added into the gold nanoparticles solution. The mixture was stirred at room temperature for 24 h. The solid was centrifuged, washed with dichloromethane and dried under high vacuum. A 500 μg mL^{-1} suspension of PEG-Au-MSN in PBS (pH 7.4) was prepared and ζ-potential of PEG-Au-NPs was measured to be -39.6 mV on a Malvern Nano HT Zetasizer.

2. Characterization

2.1 Powder X-Ray Diffraction

X-ray diffraction patterns of the MSN materials were obtained in a Rigaku ultima IV X-ray diffractometer using Cu Kα irradiation.

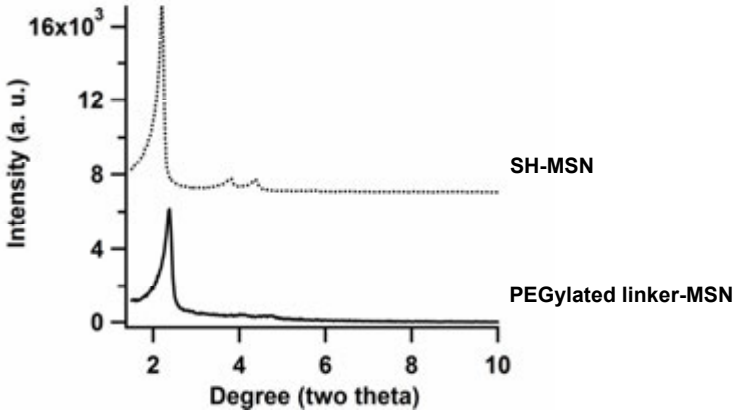

Figure S1. Low angle X-Ray Diffraction patterns of SH-MSN (dotted line) and PEGylated linker-MSN (solid line).

2.2 Nitrogen adsorption/desorption isotherms

Surface analysis of the MSN materials was performed by nitrogen sorption isotherms in a Micromeritics Tristar 3000 sorptometer. The surface areas were calculated by the Brunauer–Emmett–Teller (BET).

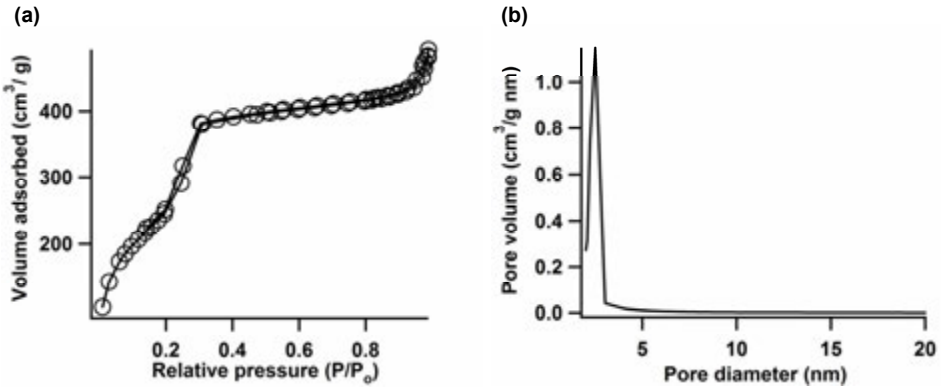

Figure S2. (a) BET nitrogen adsorption/desorption isotherms and (b) BJH pore size distributions of PEGylated linker-MSN. Surface area and pore diameter of PEGylated linker-MSN were calculated to be 929 m^2 g^{-1} and 2.5 nm, respectively.

2.3 Transmission Electron Microscopy (TEM)

The TEM examination was completed on a Tecnai G2 F20 electron microscope operated at 200 kV to examine at electron optical magnification of 64,000 to 550,000.

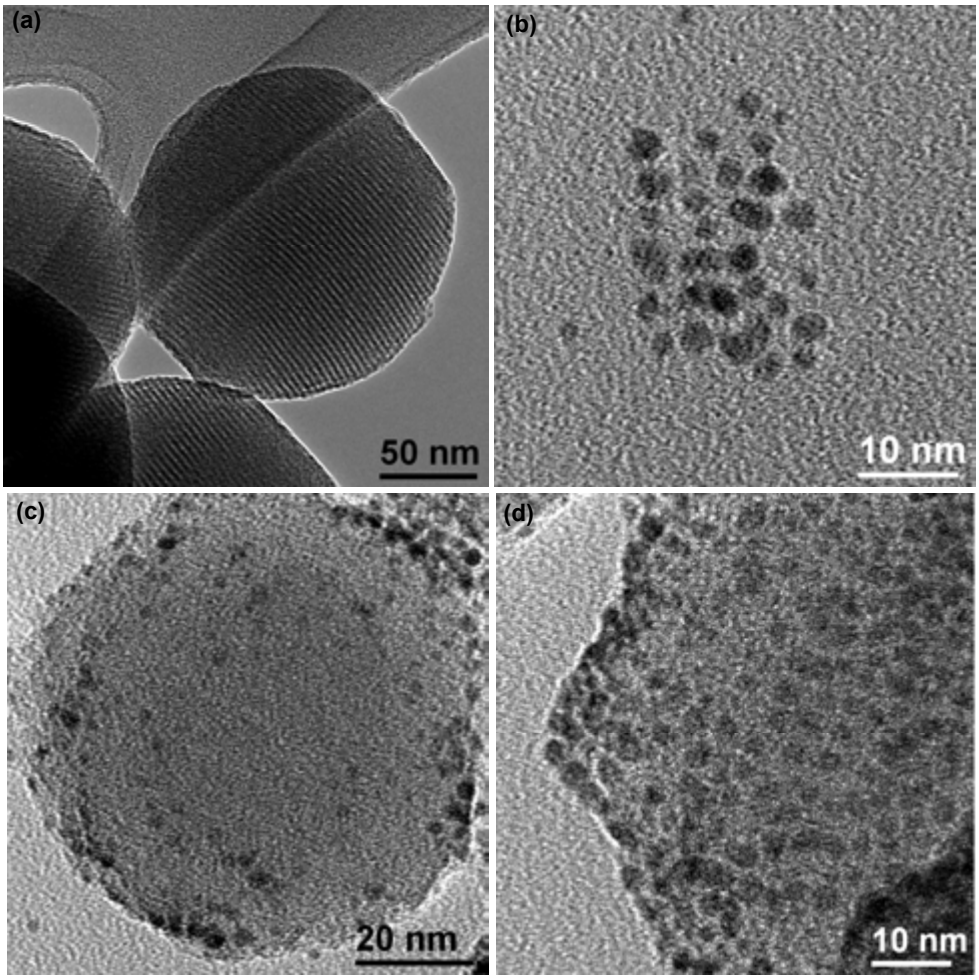

Figure S3. TEM micrographs of (a) PEGylated linker-MSN, (b) PEG-Au NP, (c-d) luciferin-loaded Au-MSN.

3. Loading and releasing experiments

3.1 Mesopores capping with PEG-Au NPs

PEGylated linker-MSN (25.0 mg) was suspended in 10 ml PBS (pH 7.4), PEG-Au NPs (25.0 mg) were added to the above suspension along with the addition of N-hydroxysuccinimide (NHS, 10 mg) and 1-ethyl-3-(3-dimethylaminopropyl) carbodiimide hydrochloride (EDC, 10 mg). The mixture was stirred for another 24 h followed by filtration and washing with PBS (×8), giving rise to the desired Au-MSNs.

3.2 Loading of luciferin and capping with PEG-Au NPs

PEGylated linker-MSN (25.0 mg) was suspended in 10 ml PBS (pH 7.4) containing 35.7 μM D-luciferin, and incubated at room temperature with stirring for 24 h. PEG-Au NPs (25.0 mg) were added to the above suspension along with the addition of

N-hydroxysuccinimide (NHS, 10 mg) and 1-ethyl-3-(3-dimethylaminopropyl) carbodiimide hydrochloride (EDC, 10 mg). The mixture was stirred for another 24 h followed by filtration and washing with PBS (×8), giving rise to the desired luciferin-loaded Au-MSNs. The loading of luciferin (13.1 μmol g^{-1}) was measured by fluorescence microscopy (FluoroMax-2, λ_{ex} 330 nm, λ_{em} 535 nm) and calculated by subtracting the amount of luciferin remaining in the phosphate buffer and the combined washings from the amount of luciferin initially added to the reaction.

3.3 Controlled release of luciferin

Luciferin-loaded Au-MSNs (10 mg) were pre-treated by a solution (1 ml) of luciferase (1 mg), ATP (0.08 μmol) and Mg^{2+} (8 μmol) to consume the physisorbed luciferin that is tolerant to PBS washing. The pre-treated luciferin-loaded Au-MSNs (5 mg) were then suspended in 5 ml PBS and stirred at room temperature. The amount of luciferin leaching was monitored by fluorescence measurement (FluoroMax-2, λ_{ex} 330 nm, λ_{em} 535 nm) over a period of 23 h. Dithiothreitol (DTT) was then added to the above suspension with final concentration of 1 mM. The release of luciferin triggered by DTT was monitored at different time intervals by fluorescence microscopy.

3.4 Loading of luciferase

The Au-MSNs (1 mg, section 3.1) or pre-treated Luciferin-loaded Au-MSN (1 mg, section 3.2) was suspended in 1 ml PBS (pH 7.4) containing 1 mg ml^{-1} of luciferase, and incubated at room temperature for 2 h. The resulting luciferase@Au-MSNs or luciferase-luciferin Au-MSNs were washed with PBS (×3) and freeze dried. A loading of luciferase (29.7 μmol/g) on luciferase-luciferin Au-MSNs was measured by luciferase activity assay as described below, and calculated by subtracting the amount of luciferase remaining in the phosphate buffer and the combined washings from the amount of luciferase initially added to the material suspension.

3.5 Luciferase activity assay

The biological acitivty of luciferase was measured according to a standard luciferase activity assay as reported previously.[4,5] Free luciferase or luciferase-luciferin Au-MSNs of different concentrations were added to a solution of $MgSO_4$ (8 mM), ATP (80 μM) and

luciferin (40 μM). Luminescence intensity was measured immediately by a luminometer in a microplate reader (Synergy MX).

3.6 Surface property effect on bioactivity of luciferase

Free luciferase (1 mg mL^{-1}) was incubated with 0.5 mg mL^{-1} of SH-MSN, PEGlyated linker-MSN Au NPs or PEG-Au NPs for different period of time (1, 3, 24 h) at room temperature. The biological activity of the treated luciferase was measured by luciferase activity assay as described above, and compared with untreated luciferase. (Figure S4)

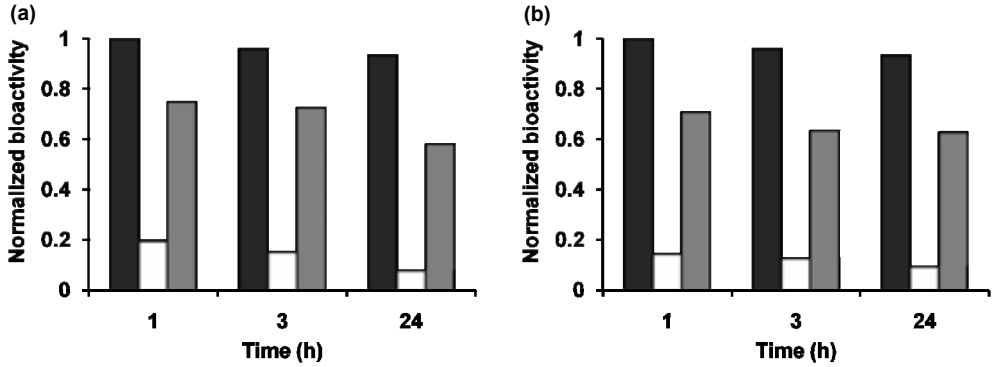

Figure S4. Normalized bioactivity of luciferase (1 mg mL^{-1}) upon incubation with 0.5 mg mL^{-1} of (a) linker-MSN (white), PEGlyated linker-MSN (gray), (b) Au NPs (white), and PEG-Au NPs (gray) for different period of time (1, 3, and 24 h), as compared to the bioactivity of untreated luciferase (1 mg mL^{-1}, black).

4. Biocompatibility studies

Reagents and materials for biological studies

HeLa cell line was obtained from American Tissue Culture Collection (ATCC). Formaldehyde solution (37%, w/w) was purchased from Fisher. 4,6-Diamidino-2-phenylindole dihydrochloride (DAPI) and trypan blue solution (0.4%, w/w) were purchased from Sigma–Aldrich. Trypsin (1×, 0.25%) in 0.1% EDTA-Na without calcium and magnesium was purchased from Fisher Scientific.

Cell line maintenance

Human liver, skin fibroblast and HeLa cells were maintained in T75 flasks using the base medium DMEM (Dulbucco's modified Eagle's medium) supplemented with 2 mM l-glutamine, 100 U/mL penicillin, 100 mg/mL streptomycin, and 1 mg/mL gentamycin.

To make the complete growth medium, 10% fetal bovine serum is added for liver and skin fibroblast cells culture, and 10% equine serum is added for HeLa cells. Rat islet tumor cells were maintained in T75 flasks using ATCC formulated RPMI-1640 medium supplemented with 10% fetal bovine serum. HeLa cells were split every 2–3 days. Human liver, skin fibroblast and rat islet tumor cells were split every 3-4 days.

4.1 Cellular uptake study

Luciferase-luciferin Au-MSNs were labeled with fluorescein isothiocyanate (denoted as luciferase-luciferin FITC-Au-MSNs) for flow cytometry measurement and confocal fluorescence microscopy imaging. FITC-labeled SH-MSNs were employed as the starting material for the preparation of luciferase-luciferin FITC-Au-MSNs and synthesized by co-condensation reaction[1] of TEOS (22.4 mmol), MPTMS (5.4 mmol) and fluorescein-linked 3-aminopropyltrimethoxysilane (FITC-APTMS, 40 μmol).

Hela cells were seeded in six-well plates at the concentration of $1x10^5$ cells/mL and incubated at 37°C under 5.5% CO_2 in the standard growth media. After 24 h incubation, the growth media were replaced by suspensions of 50 μg ml^{-1} luciferase-luciferin FITC-Au-MSNs in serum-free medium, and the cells were incubated for specific times (1,0 30, 60, 180, 360 and 540 min). The suspensions were then discarded, and the cells were harvested by trypsinization and resuspended in trypan blue solution for flow cytometry analysis. Flow cytometry was performed in a BD FACSCanto instrument. The percent of cells internalizing luciferase-luciferin FITC-Au-MSNs (FITC-positive cells) was plotted as a function of incubation time, as shown in Figure S5.

For confocal microscopy, glass cover slips were set in the bottom of the wells of the plates, followed by addition of the cell suspensions. After cell attachment, the cells were incubated with 50 μg ml^{-1} luciferase-luciferin FITC-Au-MSNs for 3 h. The nuclei were then stained with Hoechst 33258 (blue) dye. The cells were imaged in a Leica SP5 X confocal system with Leica AFS Lite 2.1.0 imaging processing software under an oil-immersion 100x objective.

For transmission electron microscopy (TEM), the trypsinized cells were fixed by 3% glutaraldehyde solution after 3 h incubation with 50 μg ml^{-1} luciferase-luciferin FITC-Au-MSNs. After 1 h incubation with 3% glutaraldehyde at 37°C, the samples were post-fixed with 1% osmium tetroxide in PBS for 1.5 h. Cells were then dehydrated in increasing concentrations of ethanol (50%, 60% 70%, 80%, 90%, and 100%) for 15

min each and stained with 2% uranyl acetate in 70% ethanol at room temperature overnight. The cells were washed three times with acetone and embedded in Epon. Embedded samples were sectioned in 60 nm thick slices on a sliding ultramicrotome. Thin sections supported on copper grids were examined with a Tecnai G2 F20 transmission electron microscope operated at 200 kV.

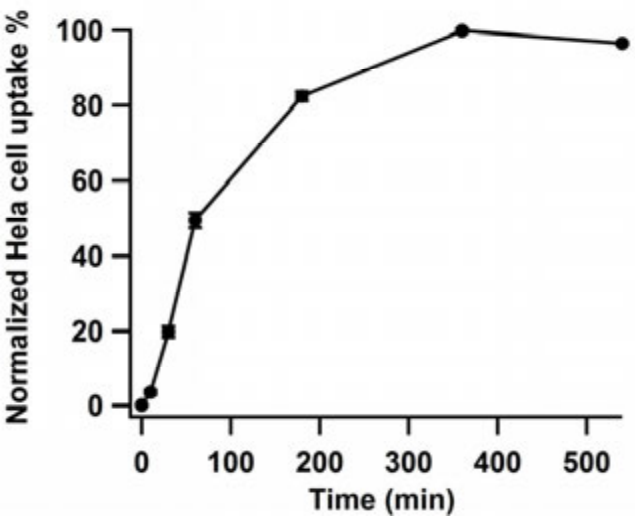

Figure S5. Endocytosis kinetics measurement of Hela cells incubated with 50 μg ml^{-1} luciferase-luciferin FITC-Au-MSNs. The cellular uptake percentage at each time point was normalized to that at 6 h of contact (63% FITC-positive cells).

4.2 Cell viability study

HeLa cells were seeded in 6-well plates at the concentration of $1x10^5$ cells/mL and were incubated for 24 h in standard culture medium at 37 °C in 5% CO_2. After 24 h incubation, the growth medium was replaced by suspensions of 20, 50 and 100 μg ml^{-1} luciferase-luciferin Au-MSNs in the standard medium, and the cells were incubated for 24 h. As a control experiment, the cells were incubated with standard growth medium without luciferase-luciferin Au-MSNs for another 24 h. Finally, the cytotoxicity of the material with Hela cells was evaluated by Guava ViaCount cytometry assay (Guava Technologies, Inc.; Hayward, CA). Cell viability % = (number of viable cells after treatment with luciferase-luciferin Au-MSNs / number of viable cells from untreated control sample)×100%. (Figure S6)

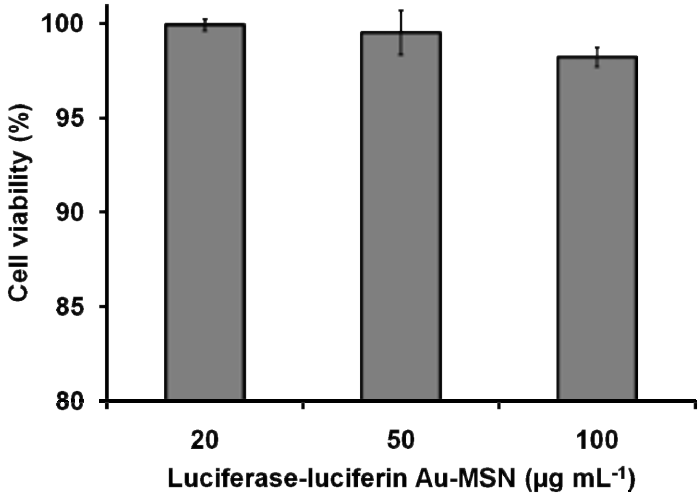

Figure S6. Cytotoxicity study of luciferase-luciferin Au-MSN with Hela cells. Hela cells were incubated with different concentrations (20, 50, 100 μg ml^{-1}) of luciferase-luciferin Au-MSN suspensions for 24 h before measuring cell viability by Guava ViaCount cytometry assay.

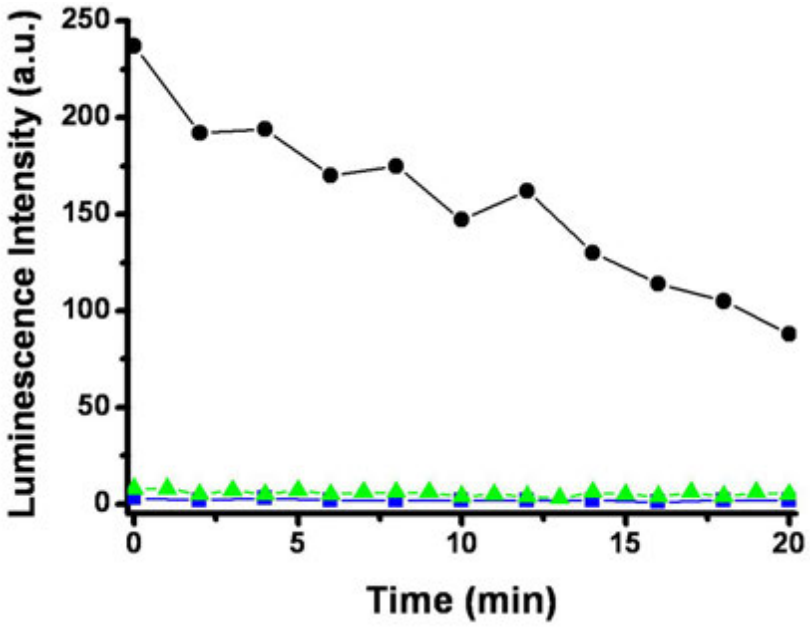

Figure S7. Luminescence from Hela cells (4×10^5 cells mL^{-1}) measured after 3 h incubation with luciferase-luciferin Au-MSNs (50 μg mL^{-1}, black dot) and with luciferase@Au-MSNs (50 μg mL^{-1}, green triangle), as compared to untreated cells (blue square).

4.3 Intracellular luciferase activity assay

Hela cells were seeded in 96-well plates at the concentration of $1x10^5$ cells ml^{-1} and incubated at 37°C under 5.5% CO_2 in the standard growth media. After 24 h incubation, the growth media were replaced by suspensions of 50 μg ml^{-1} luciferase-luciferin Au-MSNs in serum-free medium, and the cells were incubated for either 3 h or 6 h. A solution of $MgSO_4$ (8 mM) was then added and luminescence intensity was measured by a luminometer on a microplate reader (Synergy MX), as shown in Figure S7 and S8.

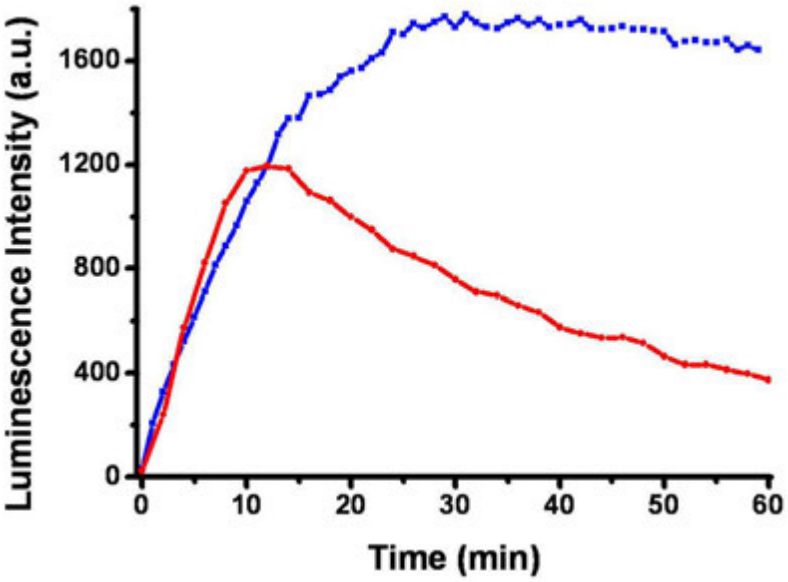

Figure S8. Observed luminescence after addition of 1 mM dithiothreitol (DTT) to Hela cells (4×10^5 cells mL^{-1}) preincubated with luciferase-luciferin Au-MSNs (50 μg mL^{-1}) for 3 h (red dot) and 6 h (blue square).

REFERENCES

(1) Lai, C.-Y.; Trewyn, B. G.; Jeftinija, D. M.; Jeftinija, K.; Xu, S.; Jeftinija, S.; Lin, V. S. Y. *Journal of the American Chemical Society* **2003**, *125*, 4451-4459.

(2) Brust, M.; Walker, M.; Bethell, D.; Schiffrin, D. J.; Whyman, R. *J. Chem. Soc., Chem. Commun.* **1994**, 801-802.

(3) Cutler, E. C.; Lundin, E.; Garabato, B. D.; Choi, D.; Shon, Y.-S. *Materials Research Bulletin* **2007**, *42*, 1178-1185.

(4) Leach, F. R.; Webster, J. J. *Methods Enzymol.* **1986**, *133*, 51-70.

(5) Lin, S.; Cohen, H. P. *Anal. Biochem.* **1968**, *24*, 531-540.

CHAPTER 7. GENERAL CONCLUSIONS

This dissertation summarizes the research accomplished during my doctoral studies. The central theme is focused on the applications of mesoporous silica nanoparticles (MSNs) in the field of drug delivery as well as catalysis. Contributions in both fields have been made by Dr. Lin's and Dr. Trewyn's group, using MSNs to serve as multiple biomolecules intracellular delivery vehicles, or as solid supports for noble metal catalyst complexation. Unique features of MSNs, such as large surface area, tunable pore diameter, controllable particle size and morphology, excellent biocompatibility, offer great advantages over other materials.

Recent advancement of hybrid MSNs materials as non-invasive, biocompatible drug delivery devices has been well established in pharmaceutical research. The flexibility to functionalize both interior pore and exterior particle surface of MSNs with organic components has led to the fabrication of numerous MSNs based nanovalve and capping systems. Thus, drug molecules can be encapsulated in the pores and released in a controlled fashion by physical, chemical or biological external or internal stimuli. Although the biocompatibility of MSNs has not been fully unveiled, paradigms of successful *in vivo* drug delivery systems using MSNs have been demonstrated. Investigations conducted on the hemocompatibility of MSNs showed that the interactions of MSNs with human red blood cells (RBC) membranes are particle size- and surface-dependent. Moreover, hemocompatibility of MSNs can be regulated by surface modification. In addition, it is discovered for the first time that MSNs were internalized by RBC, rendering the possibility of delivering drug molecules into non-phagocytic cells with MSNs.

MSNs material has also been extensively applied in the field of catalysis as solid scaffolds. A Pt(II) complex catalyst was tethered onto MSNs via a post-synthesis method. A detailed study suggests that the assembly exhibited preserved catalytic activity and dramatically improved thermal stability comparing to the homogeneous catalyst. Furthermore, this MSNs supported noble metal catalyst can function synergically with other catalysts, especially biocatalysts. In an alcohol oxidative esterification reaction, with the aid of alcohol dehydrogenase (ADH) to efficiently oxidize alcohol to aldehyde, MSNs supported Au nanoparicles (Au-MSN) were able to subsequently convert aldehyde

to esters with fast kinetics. The fundamental studies would enable this co-catalyst system to extend to a variety of catalyst pairs for a great scope of reactions.

Taking advantage of the excellent endocytosis efficiency of MSNs, catalysis reactions can take place intracellularly using cell components as substrates. An intracellular co-delivery system was designed based on a gold nanoparticles-capped MSNs platform. Luciferin was trapped inside the pore channels and released upon gold nanoparticle uncapping after cell internalization. Luciferase enzyme with preserved bioactivity was co-delivered simultaneously. Successful intracellular catalysis reaction was indicated by the emission of luminescence signals during the oxidization of delivered luciferin and intracellular ATP by luciferase enzyme. This co-delivery system could play a significant role in intracellular controlled catalysis and tumor imaging.

In summary, MSNs material shows its versatility in a wide range of applications. However, applications are not limited to what have been discussed in this dissertation. We envision that in the future, multi-functional MSNs assemblies can be developed to accomplish multiple tasks simultaneously.